Domain wall propagation combining spin-polarized current and all-optical switching

Boyu Zhang

NNT : 2019SACLS096

Propagation des Parois de Domaines Combinant Courant Polarisé et Commutation Toute Optique

Domain Wall Propagation Combining Spin-Polarized Current and All-Optical Switching

Thèse de doctorat de l'Université Paris-Saclay et de l'Université de Beihang
préparée à l'Université Paris-Sud

École doctorale n°575 : electrical, optical, bio : physics and engineering (EOBE)
Spécialité de doctorat : Physique

Thèse présentée et soutenue à Pékin, le 23 Mai 2019, par

Boyu Zhang

Composition du Jury :

Zheng Zheng Professeur, Université de Beihang	Président
Gilles Gaudin Directeur de recherche CNRS, Grenoble, SPINTEC	Rapporteur
Jianhua Zhao Professeur, Académie chinoise des sciences	Rapporteur
Nicolas Vernier Maitre de conférences, HDR, Université Paris-Saclay	Examinateur
Dafiné Ravelosona Directeur de recherche CNRS, Orsay, C2N	Directeur de thèse
Weisheng Zhao Professeur, Université de Beihang	Directeur de thèse
Stéphane Mangin Professeur, Université de Lorraine, Institut Jean Lamour	Co-Directeur de thèse

Thèse de doctorat

REMERCIEMENTS

Je souhaite commencer ce manuscrit par adresser mes remerciements sincères aux personnes qui m'ont beaucoup aidé depuis quatre ans et qui ont contribué à l'achèvement de cette mémoire. Cette thèse a été menée dans le cadre de la coopération entre le Centre de Nanoscience et Nanotechnologie (C2N) de l'Université Paris-Saclay, l'Institut Jean Lamour (IJL) de l'Université de Lorraine et le Fert Beijing Institute de l'Université de Beihang.

J'aimerais remercier en premier lieu mes directeurs de thèse Monsieur Dafiné Ravelosona, directeur de recherche CNRS à l'Université Paris-Saclay et Monsieur Weisheng Zhao, professeur à l'Université de Beihang, et aussi mon co-directeur de thèse Monsieur Stéphane Mangin, professeur à l'Université de Lorraine, qui m'ont accueilli dans leur équipe et qui m'ont soutenu tout au long des quatre ans de travail.

Pendant la 1ère année, j'ai acquis des connaissances basiques sur la spintronique et le magnétisme, déposé des couches minces et mesuré leur propriété magnétique sous la direction de M. Weisheng Zhao. Dès la 2ème année, j'ai commencé des expériences sur les parois de domaine combinant le courant et le laser sous la direction de M. Dafiné Ravelosona et de M. Stéphane Mangin. Ils m'ont aidé à exploiter des démarches de recherche scientifique et à résoudre des problèmes scientifiques ou administratifs.

Je tiens à remercier sincèrement Prof. Gilles Gaudin de Spintec, Prof. Jianhua Zhao de l'Académie chinoise des sciences, Prof. Nicolas Vernier de l'Université Paris-Saclay, Prof. Zheng Zheng de l'Université de Beihang d'avoir accepté d'être membre du jury de thèse ainsi que pour leurs remarques et discussions très enrichissantes.

Mes remerciements vont tout particulièrement à Prof. Youguang Zhang, Prof. Na Lei, Prof. Xiaoyang Lin, Dr. Jun Du, Dr. Xueying Zhang, Dr. Yong Xu, Dr. Huaiwen Yang et Dr. Yu Zhang, pour leurs suggestions d'orientation des travaux et leurs expertises expérimentales, et à Dr. Gefei Wang pour m'avoir hébergé pendant mes séjours à Orsay.

Mes remerciements vont ensuite à toutes les personnes de l'équipe de nanomagnétisme et électronique de spin de l'IJL. Je remercie Prof. Sébastien Petit-Watelot et Prof. Carlos Rojas-Sanchez pour leurs conseils sur les expériences électriques, et Prof. Gregory Malinowski et Prof. Jon Gorchon pour leurs conseils pendant les expériences de laser. Je voudrais exprimer aussi toute ma gratitude à Dr. Laurent Badie, qui m'a guidé tout au long de la fabrication des micro-fils, et à Prof. Stéphane Andrieu et Prof. Michel Hehn, qui m'ont aidé pour déposer des couches minces. Merci à Pierre Vallobra pour son aide précieuse avec la pulvérisation et merci à Filip Schleicher pour la discussion concernant la simulation de commutation tout optique. Un grand merci à Dr. Crosby Soon Chang pour son conseil avec la mesure des propriétés magnétiques. Je tiens à remercier les doctorants: Kosseila Ait-Oukaci, Hamza Bouhani, Alexandre Dekens, Thibaud Fache, Charles Guillemard, Anton Kyianytsia, Gauthier Masset, Maryam Massouras et Thai Ha Pham, pour les bons moments passés ensemble à Nancy, je leur souhaite plein de réussite pour leur thèse.

Je voudrais aussi adresser mes remerciements à Monsieur Nicolas Vernier, professeur au C2N, qui m'a dirigé pour l'expérience de Kerr et donné des conseils sur ma recherche, à Monsieur Sylvain Eimer, ingénieur au C2N, qui m'a enseigné la technique de pulvérisation, à Monsieur Romain Baude, président de l'entreprise APREX solutions, qui m'a aidé pour traiter les données avec le logiciel TRACK, à Mme Sophie Bouchoule, Mme Laurence Stephen et Prof. Eric Cassan de l'école doctorale EOBE pour leur aide lors de l'inscription et la soutenance de ma thèse.

Je tiens à remercier vivement Prof. Eric Fullerton et Prof. Albert Fert pour nos discussions fructueuses.

Je voudrais aussi remercier tous mes amis: Jianying Qin, Shiheng Liang, Xue Gao, Bingshan Tao, Er Liu, Mamour Sall, Salmen Mrahi, You Wang, Qi An, Jiaqi Zhou, Xiaoxuan Zhao, Xiaochao Zhou, Yang Liu, Deming Zhang, Mengxing Wang, Shouzhong Peng, Lezhi Wang, Jiang Nan, Heng Zhao, Runnan Zhou, Kaihua Cao, Qian Shi, Jiaqi Wei, Anni Cao, Zilu Wang, Shaohua Yan, Pan Liu, Junfeng Qiao, Daoqian Zhu, Houyi Cheng, pour leur accompagnement et aide durant ces quatre ans.

Un grand merci à China Scholarship Council (CSC) pour son support de financement pendent mes recherches en France.

Enfin, et surtout, je voudrais remercier ma famille, et particulièrement mes parents, M. Lingjun Zhang et Mme Meihong Dong, qui ont cru en moi et m'ont encouragé et rassuré dans mes moments de doute et face aux difficultés.

Boyu Zhang

23 Mai 2019, Pékin

TABLE OF CONTENTS

ABSTRACT

Since the first observation of ultrafast demagnetization in Ni films arising from a pulsed laser excitation, there has been a strong interest in understanding the interaction between ultrashort laser pulses and magnetization. These studies have led to the discovery of all-optical switching (AOS) of magnetization in a ferrimagnetic film alloy of GdFeCo using femtosecond laser pulses. All-optical switching enables an energy-efficient magnetization reversal of the magnetic material with no external magnetic field, where the direction of the resulting magnetization is given by the right or left circular polarization of the light.

The manipulation of magnetization through laser beam has long been restricted to one material, though it turned out to be a more general phenomenon for a variety of ferromagnetic materials, including alloys, multilayers and heterostructures, as well as rare earth free synthetic ferrimagnetic heterostructures. Recently, we have observed the same phenomenon in single ferromagnetic films, thus paving the way for an integration of all-optical writing in spintronic devices.

Moreover, in similar materials, like [Co/Pt] or [Co/Ni] with high spin polarization and tunable perpendicular magnetic anisotropy (PMA), efficient current-induced domain wall (DW) motion can be observed in magnetic wires, where spin-orbit torque (SOT) or spin transfer torque (STT) provides a powerful means of manipulating domain walls, which is of great interest for several spintronic applications, such as high-density racetrack memory and magnetic domain wall logic. However, the current density required for domain wall motion is still too high to realize low power devices.

It is within this very innovative context that my Ph.D. research has focused on domain wall manipulation in magnetic wires made out of thin film with strong perpendicular magnetic anisotropy combining both spin-polarized current and all-optical switching. Different material structures have been explored, in order to investigate the combined

effects of helicity-dependent optical effect and spin-orbit torque or spin transfer torque on domain wall motion in magnetic wires based on these structures. We show that domain wall can remain pinned under one laser circular helicity while depinned by the opposite circular helicity, and the threshold current density can be greatly reduced by using femtosecond laser pulses. Our findings provide novel insights towards the development of low power spintronic-photonic devices.

Keywords: domain wall, spin-polarized current, femtosecond laser, racetrack memory, spintronics, magnetic multilayered wires

RÉSUMÉ

Depuis la première observation de désaimantation ultra-rapide dans des films de Ni soumis à une excitation laser pulsée, on a assisté à un grand intérêt de comprendre l'interaction entre les impulsions laser ultra-courtes et l'aimantation. Ces études ont conduit à la découverte de la commutation toute optique de l'aimantation dans un alliage de film ferrimagnétique en utilisant des impulsions laser femtosecondes. La commutation toute optique permet un renversement de l'aimantation d'un matériau magnétique sans champ magnétique externe. La direction de l'aimantation résultante est donnée par la polarisation circulaire droite ou gauche de la lumière.

La manipulation de l'aimantation par un faisceau laser a longtemps été limité à un seul type de matériau, mais ce mécanisme s'est avéré être un phénomène plus général qui s'applique à une grande variété de matériaux ferromagnétiques, y compris des alliages, des empilements et des hétérostructures, ainsi que des hétérostructures ferrimagnétiques synthétiques de terres-rares. Récemment, nous avons observé le même phénomène dans des films ferromagnétiques simples, ouvrant ainsi la voie à une intégration de l'écriture toute optique dans les dispositifs spintroniques.

De plus, dans des matériaux de type [Co/Pt] ou [Co/Ni] avec une polarisation de spin élevée et une anisotropie magnétique perpendiculaire contrôlable, un mouvement de parois de domaines induit par un courant polarisé peut être observé dans des pistes magnétiques (couple spin-orbite ou couple de transfert de spin), ce qui présente un grand intérêt pour des applications spintroniques basse consommation et de densité élevée, telles que le concept de mémoire racetrack et la logique magnétique. Cependant, la densité de courant requise pour le mouvement des parois de domaines est encore trop élevée pour permettre la réalisation de dispositifs à faible puissance.

Dans ce contexte innovant, la recherche effectuée dans le cadre de ma thèse s'est concentrée sur la manipulation de parois de domaines dans les pistes fabriquées à partir

de films minces à forte anisotropie magnétique perpendiculaire en combinant à la fois les effets du courant polarisé et ceux de la commutation toute optique. Différents films minces ont été explorés afin d'étudier les effets combinés optiques dépendant de l'hélicité et des couples spin-orbite ou de transfert de spin sur le mouvement des parois de domaines. Nous avons montré que les parois de domaines peuvent rester piégées sous une hélicité circulaire du laser et dépiégées par une hélicité circulaire opposée, et la densité de courant polarisé seuil peut être considérablement réduite en utilisant un laser femtoseconde. Nos résultats sont prometteurs pour le développement de nouveaux dispositifs photoniques-spintroniques de faible puissance.

Mots clés: parois de domaines, courant polarisé, laser femtoseconde, mémoire racetrack, spintronique, fils multicouches magnétiques

GENERAL INTRODUCTION

Spintronics is an emerging technology, which explores the spin of the electrons besides its charge and enables a new degree of freedom for the manipulation of magnetic devices. It is a multidisciplinary topic that combines condensed state physics, microelectronics and materials science. It has attracted great interest since the observation of giant magnetoresistance (GMR) effect by A. Fert at University of Paris-Sud [BAI88] and by Professor P. Grünberg at Jülich Research Centre [BIN89] independently in 1988.

The GMR effect is present in ultra-thin ferromagnetic metal/non-magnetic metal multilayered spin-valve structures and exhibits a large resistance difference between the parallel and antiparallel magnetizations of two adjacent ferromagnetic layers separated by a nonmagnetic layer. This effect has been used in the read head of hard disk drives, which has allowed their tremendous increase in storage density [FUL16]. The Nobel prize in Physics was awarded to A. Fert [FER08] and P. Grünberg [GRU08] in 2007 for the discovery of the GMR effect.

The magnetoresistance ratio of GMR effect in all-metal based spin valves is about 5% at room temperature [HUA08]. Since the discovery of tunnel magnetoresistance (TMR) effect in magnetic tunneling junction (MTJ) containing ferromagnetic metal/insulator/ferromagnetic metal tri-layered structure at room temperature in 1995 [MOO95, MIY95], the magnetoresistance ratio has increased significantly due to the tunneling effect of electrons through the ultrathin insulator [PAR04, YUA04]. The development of advanced MTJs based on CoFeB-MgO materials with TMR ratio up to 230% [DJA05] has enabled the development of magnetic random-access memory (MRAM), a new non-volatile memory technology that has the potential to replace all memory technologies. MRAM has the advantages of non-volatility, high speed, low power, scalability and strong endurance [AKE05]. A MRAM cell stores bits “0” and “1” using a parallel or antiparallel magnetization state of the two adjacent magnetic layers,

where one is the fixed layer and the other is the free storing layer.

The first generation of MRAM was controlled by a magnetic field that is not efficient in terms of power, as an external field needs to be generated and it is difficult to implement this scheme into small devices [ENG05]. In 1996, J. Slonczewski and L. Berger predicted the existence of spin-transfer torque (STT) [SLO96, BER96]: when a spin-polarized current passes through the MTJ, the transfer of angular momentum can enable the magnetic switching of the free layer. It is considered as the greatest discovery after the GMR effect in the area of spintronics with the possibility of manipulating magnetic moment with electrical current instead of magnetic field, which improves the integration of spintronic devices with CMOS technologies. The discovery of the STT effect has led to the development of STT-MRAM, the second generation of MRAM, which has allowed the reduction of power consumption and the realization of smaller cell architecture. This technology has led to the commercialization by Everspin of 64 Mb STT-MRAM in 2012, which has been used in the flight control computer of Airbus A350 aircraft. Other memory companies, including Samsung, GlobalFoundries, TSMC and Intel, are currently producing STT-MRAM for embedded applications.

STT-MRAM still suffers from relatively low storage density. In 2008, S. Parkin *et al.* proposed a new concept of MRAM, the racetrack memory [PAR08]. The data are stored in the form of multiple magnetic domains in nanowires, and domain walls (DWs) separating opposite domains can be moved sequentially in nanowires by spin-polarized current with high speed. Besides the traditional STT effect to move DW, which still needs high current densities, spin-orbit torque (SOT) can also move domain walls, which enables a much higher efficiency [RYU13, EMO13]. SOT induced domain wall needs two main ingredients. First, the presence of Dzyaloshinskii-Moriya interaction (DMI), which originates from the inversion asymmetry in multilayered structures that favors chiral domain wall or skyrmions [THI12]. Secondly, the presence of spin Hall effect that originates from the spin accumulation at the interface between heavy metal and ferromagnetic metal, which induces a vertical spin current that exerts a torque on the chiral domain wall or skyrmions resulting in fast motion [LIU12].

However, the current density required to move the domain walls by SOT along the wire is still in the range of 5×10^{12} A/cm^2, which is still too high to realize low power devices. Ultrashort laser has become an alternative way to manipulate the magnetization after the ultrafast demagnetization of Ni thin film was observed with femtosecond laser pulses [BEA96]. All-optical switching (AOS) was then demonstrated in 2007 [STA07], where left or right circularly polarized laser enables the deterministic switching of perpendicularly magnetized GdFeCo ferrimagnetic film with down or up magnetization direction, which draw the attention of the researchers for its potential to integrate ultra-low power all-optical writing into magnetic storage. S. Mangin *et al.* observed the same phenomenon in ferromagnetic materials in 2014 [MAN14], e.g. Co/Ni and Co/Pt multilayers, which can also be used for current-induced domain wall motion.

The objective of my Ph.D. thesis has been to study the assistance of femtosecond laser pulses on current-induced domain wall motion in magnetic wires for the exploration of ultra-low power spintronic devices. The combined effects of helicity-dependent optical effect and SOT or STT are investigated. In order to study this combination, different material structures are explored, in order to demonstrate all-optical switching and current-induced domain wall motion in the same magnetic wires. Finally, new logic functions are proposed based on domain wall motion by combining current and light.

The manuscript is divided into four chapters. The first chapter “Background and state-of-the-art” consists of the concepts and state-of-the-art of MRAM, domain wall motion and all-optical switching. The second chapter “Experimental tools and samples” presents the experimental equipment and techniques to fabricate the studied samples and to perform the all-optical switching and current-induced domain wall motion experiments. In the third chapter “Material exploration for all-optical switching & current-induced domain wall motion”, three sets of samples with structures suitable for SOT or STT switching are explored. In the fourth chapter “Domain wall motion combining femtosecond laser and microsecond current pulses”, the combined effect of SOT or STT and helicity-dependent optical effect are studied and domain wall logic devices are proposed for future low power applications.

CHAPTER 1 BACKGROUND AND STATE-OF-THE-ART

This chapter is a brief review of the concepts of MRAM, domain wall motion and all-optical switching, which have been used for my Ph.D. research in the following chapters.

1.1 MRAM

MRAM is a nonvolatile memory technology, which started its development in the 1990s. This technology, which has the potential to be a universal memory, includes the write/read speed of Static Random-Access Memory (SRAM), the non-volatility and storage density of flash memory, the reliability of Dynamic Random-Access Memory (DRAM) and a low power consumption due to its nonvolatility and potential low current densities for writing and reading [AKE05].

Different from traditional RAM and Flash technologies, which store data using charges, the data in MRAM are stored magnetically. The typical cell of MRAM is composed of a Magnetic Tunnel Junction (MTJ), which consists of two ferromagnetic thin films separated by an ultra-thin insulator, as shown in Figure 1-1. One (fixed layer) of the ferromagnetic layers is fixed with a large coercivity, while the magnetization direction of the other (free layer) can be changed. This magnetic cell memory stores data depending on the parallel (bit 0) or antiparallel (bit 1) magnetic configuration of the 2 ferromagnetic layers [TEH03, HUA08, WOL10].

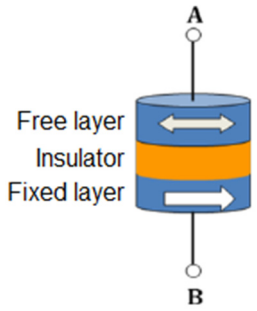

Figure 1-1 The typical structure of MTJ.

For the reading scheme, the most important discovery for the development of MRAM has been the demonstration in 2005 of a high tunneling magnetoresistance (TMR) ratio in CoFeB-MgO based magnetic tunnel junctions. A variation of up to 230% TMR ratio at room temperature has been measured when the magnetic configuration goes from parallel to antiparallel magnetization between the 2 ferromagnetic layers [DJA05]. The writing scheme in MRAM was first based on magnetic field switching generated by a high-density current flowing in write lines of the MRAM cells, as shown in Figure 1-2.

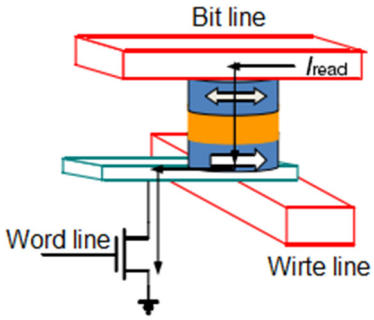

Figure 1-2 The read/write mechanism of field-induced MTJ.

As the size of MTJ becomes smaller toward technology nodes less than 90 nm, larger writing fields were needed, which resulted in higher current densities and interferences between adjacent bits, making the field assisted MRAM non-scalable, as described in Figure 1-3.

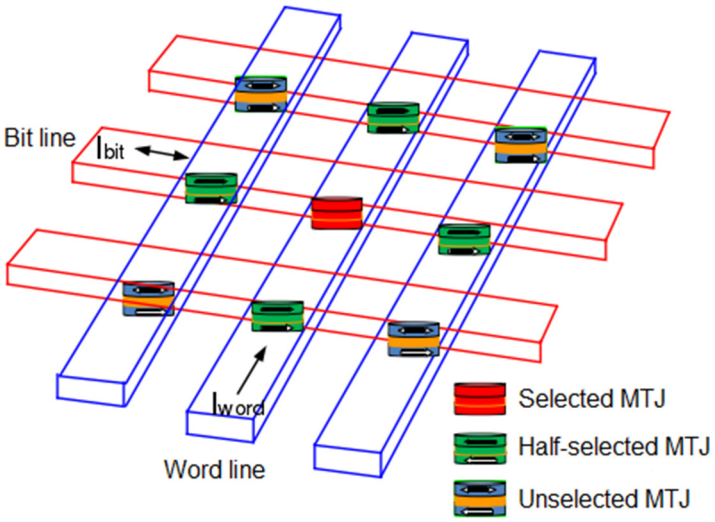

Figure 1-3 The interference between the MTJs in MRAM.

1.1.1 STT-MRAM

In 1996, J. Slonezewski and L. Berger theoretically predicted the STT effect that can induce magnetization switching of magnetic materials under polarized current instead of a magnetic field [SLO96, BER96], which provides a scalable scheme for the writing in MRAM [DIA07], which is shown in Figure 1-4.

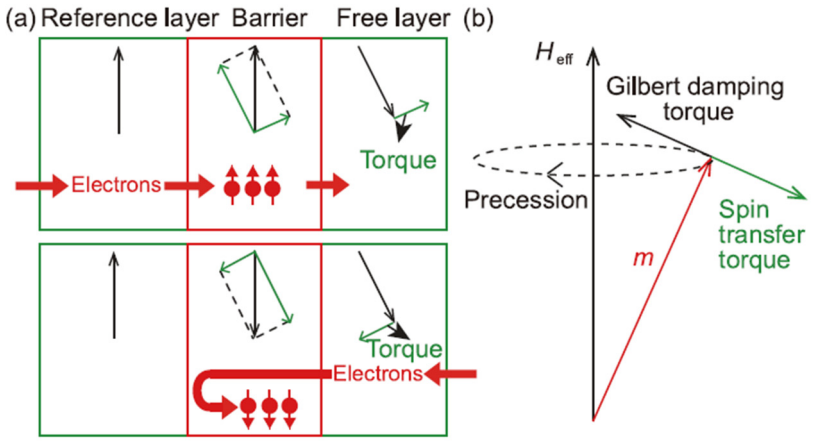

Figure 1-4 (a) The writing mechanism for P state and AP state using STT effect. (b) Effect of STT on the magnetization dynamics [ZHA16].

The reading scheme of STT-MRAM is the same as field assisted MRAM and it is based on a small current to read out the resistance of the device (low or high resistance depending on the parallel or antiparallel state). Figure 1-5 shows a structure of MTJ for STT-MRAM.

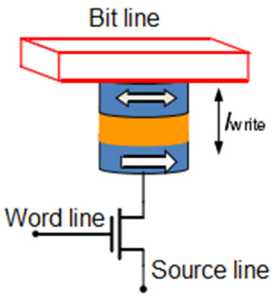

Figure 1-5 The structure of MTJ for STT-MRAM.

The magnetization dynamics induced by STT can be described by the Landau-Lifshitz-Gilbert (LLG) equation as follows:

$$\frac{\partial \boldsymbol{m}}{\partial t} = -\gamma\mu_0 \boldsymbol{m} \times \boldsymbol{H}_{\text{eff}} + \alpha \boldsymbol{m} \times \frac{\partial \boldsymbol{m}}{\partial t} - \frac{\gamma \hbar J P}{2 e t_{\text{F}} M_{\text{S}}} \boldsymbol{m} \times (\boldsymbol{m} \times \boldsymbol{m}_{\text{r}}) \tag{1.1}$$

where $\boldsymbol{m}$ and $\boldsymbol{m}_{\text{r}}$ are the magnetization vectors of free layer and reference layer, $\boldsymbol{H}_{\text{eff}}$ is the effective field, γ is the gyromagnetic ratio, μ_0 is the vacuum permeability, α is the Gilbert damping factor, J is the critical current density, P is the spin polarization ratio, and t_{F} is the thickness of free layer.

Compared to the 1st generation of MRAM, STT-MRAM directly uses current to change the magnetic state of MTJ without magnetic field, which has simpler structure, lower writing energy and higher scalability without interference between memory cells [HOS05]. The first commercial STT-MRAM was launched in 2012 by Everspin.

As shown in Eq. (1.1), the torque depends on the vector product of $\boldsymbol{m}$ and $\boldsymbol{m}_{\text{r}}$. As $\boldsymbol{m}$ and $\boldsymbol{m}_{\text{r}}$ are parallel or anti-parallel before the switching, the torque is small at first and then increases due to thermal fluctuations, resulting in an incubation time that limits the writing time. In order to increase the switching speed, the critical current density for the magnetization switching under STT has to be relatively large, which increases the power consumption and the probability for the breakdown of the MgO barrier.

1.1.2 SOT-MRAM

Recently, a new generation of MRAM driven by SOT has attracted a strong interest.

For SOT-MRAM, the basic structure concerns heavy metal in contact with the free layer of the MTJ with PMA. When the current is injected in-plane into the heavy metal layer with strong spin-orbit coupling (SOC), a vertical spin current is generated, which induces SOT on the magnetization of the free layer. The origin of this torque is still under investigation and is believed to be attributed either to the Rashba effect or to the spin Hall effect (SHE), as shown in Figure 1-6. The Rashba effect is an interfacial effect [MIR10, MIR11, CUB14]. Due to the asymmetry of the “Heavy metal/CoFeB/MgO” tri-layers structure, the current that goes through the heavy metal layer induces an effective field H_{R} along the y direction:

$$\boldsymbol{H}_{\mathrm{R}} = \alpha_{\mathrm{R}} \boldsymbol{z} \times \boldsymbol{J}_c, \tag{1.2}$$

SHE is in turn a bulk effect [HIR99, LIU12, PAI12, SIN15]. The current that goes through the heavy metal induces a pure spin current J_S:

$$\boldsymbol{J}_s = \theta_{\mathrm{SHE}} \boldsymbol{\sigma} \times \boldsymbol{J}_c, \tag{1.3}$$

where θ_{SHE} is the spin Hall angle, σ is the unit vector of the electron spin that is injected into the free layer due to SHE, and J_c is the charge current density.

Such SHE and Rashba effect induce a damping-like (DL) torque and a field-like (FL) torque on the magnetization:

$$\begin{cases} \boldsymbol{\Gamma}_{\mathrm{FL}} = -\gamma\mu_0 \boldsymbol{m} \times \boldsymbol{H}_{\mathrm{R}} = -\gamma\mu_0 \boldsymbol{m} \times \boldsymbol{H}_{\mathrm{FL}}, \\ \boldsymbol{\Gamma}_{\mathrm{DL}} = -\gamma\mu_0 \xi \boldsymbol{m} \times (\boldsymbol{m} \times \boldsymbol{\sigma}) = -\gamma\mu_0 \boldsymbol{m} \times \boldsymbol{H}_{\mathrm{DL}}, \end{cases} \tag{1.4}$$

where H_{DL} and H_{FL} are the effective fields of DL and FL torques.

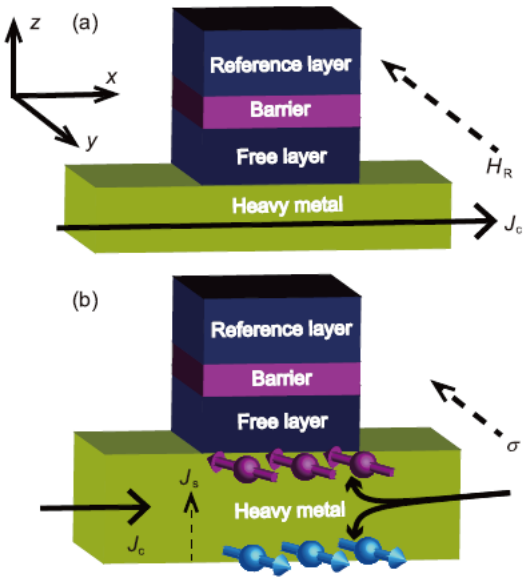

Figure 1-6 The mechanism of SOT-MRAM. Three terminal devices switched by (a) Rashba effect and (b) SHE [ZHA16].

Compared to the two-terminal MTJ structure of STT-MRAM, SOT-MRAM exhibits a more complicated three-terminal MTJ structure (Figure 1-7). The advantage is that the read and write paths are separated, and their optimization could be done separately, which increases the reliability (lower MgO breakdown), the write speed, and decreases

the critical current density for the realization of low power and high-speed data storage [CUB14]. The write speed of SOT is faster since the effective fields H_{DL} and H_{FL} are perpendicular to the magnetization of the free layer, which avoids any incubation time. The critical current density and power consumption of SOT-MRAM is also lower than that of STT-MRAM [LIU12].

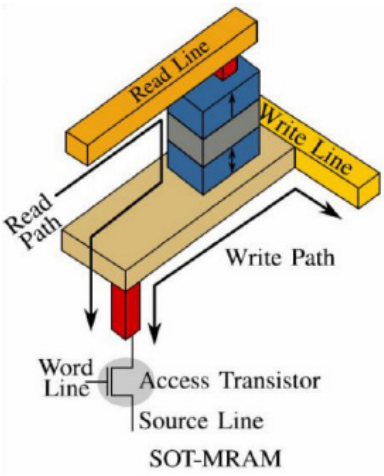

Figure 1-7 The storage unit of SOT-MRAM [OBO15].

Nowadays, the research on SOT-MRAM focuses on the optimization of the writing scheme. For example, the SOT efficiency can be improved and the critical current density can be reduced by increasing the spin Hall angle of heavy metal layer (which reflects the conversion efficiency between charge current and spin current) [ZHA15, NGU16] and by choosing heavy metal materials with high SOC [PAI12, HAN17]. In addition, as the deterministic magnetization switching by SOT normally needs an in-plane field along the direction of the injected current, the field-free switching is been investigated by material selection and structure design [YU14, AKY15, YOU15, TOR15, FUK15, VAN16], which can be ideal for practical applications.

1.2 Dynamics of domain wall motion

The storage of information using magnetic domain walls was first proposed in the 1970s as the “magnetic bubble memory”, where magnetic bubble domains in thin films can store bits of data and move with external magnetic fields [BOB75]. Recently, the

dynamics of domain wall motion has become a research focus for its potential applications in high density memory and logic devices, such as the racetrack memory concept. Racetrack memory is a new concept of data storage device, which has been proposed by S. Parkin *et al.* in 2008, as shown in Figure 1-8 [PAR08]. It combines the potential storage density of hard disk drives and the fast speed of solid-state memory. Racetrack memory stores data in the form of magnetic domains separated by domain walls along magnetic nanowires, where domain walls can be moved at high speed by spin-polarized currents. The distance between adjacent domain walls represents the length of a recording bit, which can be controlled by artificial pinning sites along the nanowires. Since DWs in films with PMA can be as narrow as 1 nm, this concept can reach ultra-high density. Basically, the racetrack memory concept works as a shift register [HAY08]. The domain walls can be written using a fixed writing head (current line on top of the wire for instance), the recording bits (magnetic domains) can move sequentially along the nanowires under a spin polarized current and the direction of magnetization can be read by a fixed read head on top of the wire (MTJ for example).

The key for the realization of racetrack memory is to reliably control the motion of multiple domain walls along the wire that interact very strongly with pinning defects (structural inhomogeneities from materials, extrinsic defects introduced by the patterning techniques). STT-driven DW motion has been first demonstrated, but limited by high current densities. Recently, most studies have focused on using SOT to drive chiral DW motion with a higher efficiency than STT [EMO13, RYU13, YAN15].

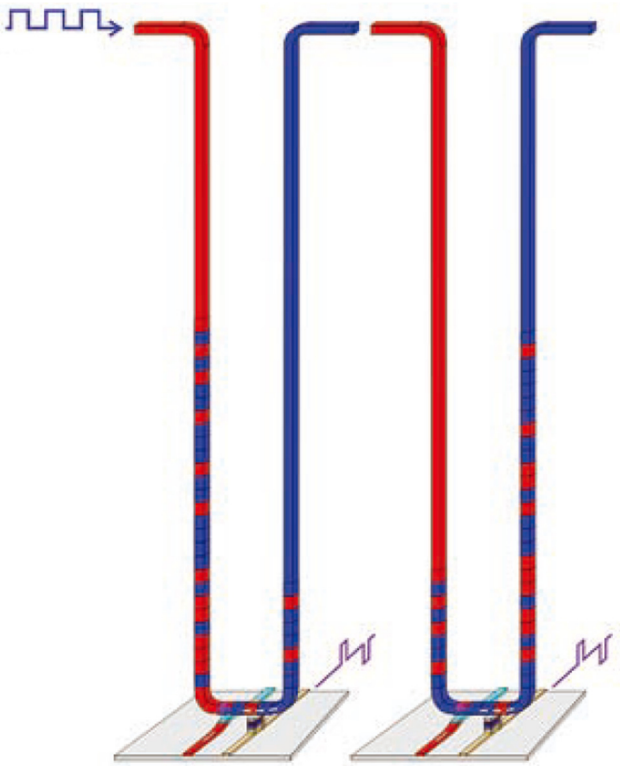

Figure 1-8 The racetrack memory concept [PAR08].

However, the current density required to move domain walls is still too high [KOY11, RYU13, YAN15], which makes this technique difficult to implement for applications. Therefore, the energy consumption still needs to be reduced. For the practical realization of DW-based devices, it is crucial to increase the domain wall velocity, decrease the critical current density and reduce the density of pinning defects that induce random behavior.

1.2.1 Domain wall and Dzyaloshinskii Moriya Interaction (DMI)

The presence of magnetic domain wall results from the competition between anisotropy and exchange energies. In ultra-thin films with perpendicular anisotropy, the energetically favorable structures are Bloch domain walls where the magnetization in the domain wall center is parallel to the domain wall plane. When the films are patterned into small wires, Néel walls are favored where the magnetization in the center is perpendicular to the domain wall plane, in order to reduce the magnetostatic energy due to magnetic charges at the edges of the wires. In both cases, Bloch and Néel walls are not chiral, i.e, they have the same probability to be left-handed or right-handed.

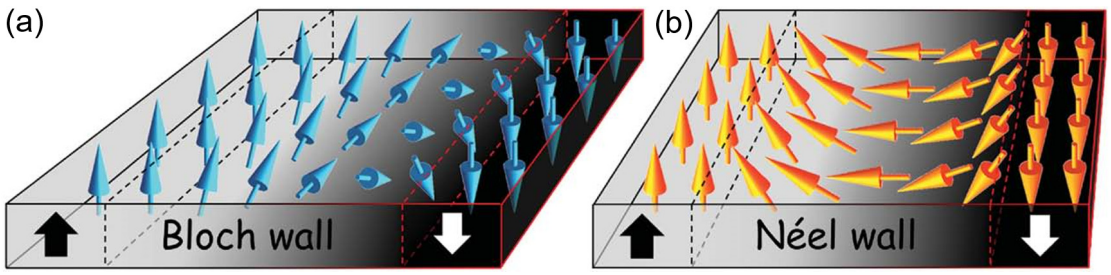

Figure 1-9 Schematic of magnetic domain walls in materials with PMA. (a) Bloch wall and (b) Néel wall [CHE15].

In presence of the Dzyaloshinski-Moriya interaction, chiral Néel walls are favored as described below. The asymmetry exchange effect in interfacial asymmetric structures was first proposed by Dzyaloshinskii based on Landau theory in 1958 to explain the weak magnetism in anti-ferromagnetic materials [DZY58]. Later, Moriya explained this effect by considering SOC, where a super-exchange interaction is present for neighboring spins of asymmetry magnetic insulator [MOR60]. As a result, it was later called Dzyaloshinskii-Moriya Interaction (DMI). Prof. A. Fert predicted the existence of interfacial DMI in heavy metal/ferromagnetic metal thin film structures, where an indirect exchange effect is induced between the non-linear spin in ferromagnetic layer and the heavy metal atom with strong SOC, due to the broken inversion asymmetry [FER90].

The energy of DMI can be expressed quantitatively as [FER17]:

$$E_{\mathrm{DMI}} = -\boldsymbol{D}_{\mathrm{ij}} \cdot (\boldsymbol{S}_{\mathrm{i}} \times \boldsymbol{S}_{\mathrm{j}}) \tag{1.5}$$

where $\boldsymbol{D}_{\mathrm{ij}}$ is the DMI vector, $|\boldsymbol{D}_{\mathrm{ij}}| = D_{\mathrm{DMI}}$ is the magnitude of $\boldsymbol{D}_{\mathrm{ij}}$ as follows:

$$D_{\mathrm{DMI}} = \mu_0 H_{\mathrm{DM}} M_{\mathrm{S}} \Delta_{\mathrm{DW}} \tag{1.6}$$

where μ_0 is the vacuum permeability, H_{DM} is the effective field of DMI, M_{S} is the saturation magnetization, Δ_{DW} is the domain wall width. As shown before, Δ_{DW} is given by $\Delta_{\mathrm{DW}} = (A/K_{\mathrm{eff}})^{1/2}$, where A is the exchange stiffness, K_{eff} is the effective anisotropy. As shown in Figure 1-10, the direction of $\boldsymbol{D}_{\mathrm{ij}}$ is determined by $\boldsymbol{r}_{\mathrm{ij}} \times \boldsymbol{x}$, which is perpendicular to the plane formed by $\boldsymbol{S}_{\mathrm{i}}$, $\boldsymbol{S}_{\mathrm{j}}$ and the neighbor atoms.

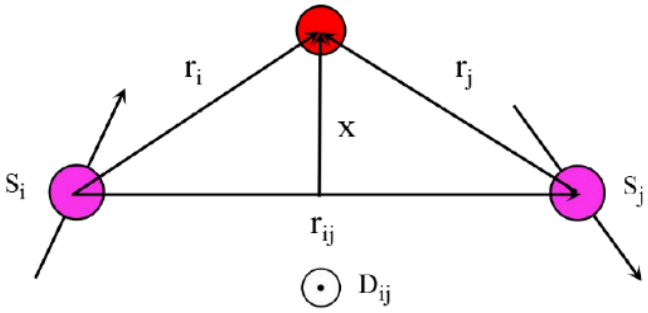

Figure 1-10 Schematic of the DMI field due to the indirect coupling of 2 magnetic atoms [ANT19].

The DMI at the interface of heavy metal/ferromagnetic metal thin film structure provides a new degree for the manipulation of electron spins and induces a variety of spin-dependent phenomena, such as the presence of chiral Néel domain wall [THI12, RYU13, EMO13] or skyrmions [SAM13].

The sign of DMI is determined by the DMI vector $\boldsymbol{D}_{ij}$ in Eq. (1.7) [FER17]:

$$\boldsymbol{D}_{ij} = D_{ij} \cdot (\boldsymbol{z} \times \boldsymbol{u}_{ij}) \tag{1.7}$$

where $\boldsymbol{z}$ is the direction vector of z axis, $\boldsymbol{u}_{ij}$ is the direction vector from $\boldsymbol{S}_i$ to $\boldsymbol{S}_j$.

The chirality of domain wall is related to the sign of DMI as shown in Figure 1-11: right-handed domain wall for negative DMI (clockwise), or left-handed domain wall for positive DMI (anti-clockwise) [BOD07].

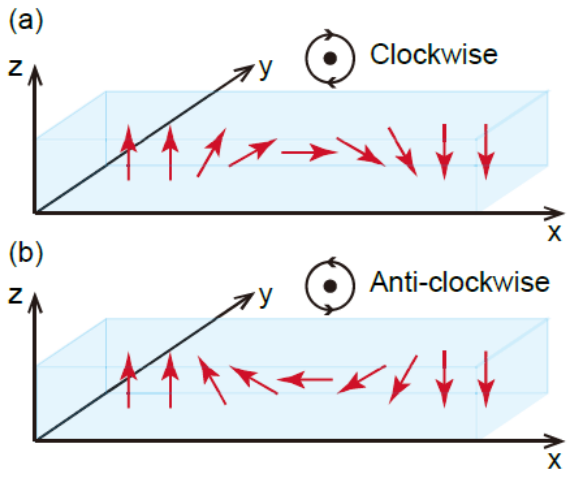

Figure 1-11 Chiral domain walls with (a) right-handed chirality and (b) left-handed chirality. The red arrow represents the direction of magnetization.

For the measurement of DMI, Brillouin Light Scattering (BLS) is commonly used [COR13], which measures the frequency shift of two spin waves with opposite directions to extract the DMI factor. This method is accurate, because the DMI is directly obtained without the use of magnetic parameters, such as the exchange constant A_{ex}, the effective anisotropy K_{eff}. However, the BLS equipment is relatively complex, which limits the application scope of this method.

The more convenient way to measure the DMI value is to measure the velocity of domain wall asymmetry expansion in the creep mode when an in-plane field is applied, as proposed by Je et *al.* in 2013 and experimentally demonstrated in Pt/Co/Pt structure [JE13]. Figure 1-12 shows typical Kerr images of domain wall expansion without and with the in-plane field measured by Kerr microscopy.

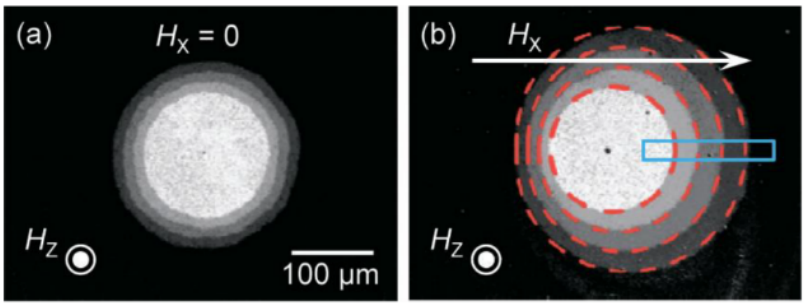

Figure 1-12 Domain wall expansion induced by a perpendicular field H_Z of 3 mT (a) without and (b) with an in-plane field H_X of 50 mT. The images are measured by Kerr microscopy and processed by taking 4 sequential images with a time step of 0.4 s [JE13].

In a structure without DMI or applied in-plane field, the center magnetization direction is parallel to the domain wall plane, resulting in a Bloch wall that reduces the domain wall surface energy, as shown in Figure 1-13 (a). When DMI is present, the center magnetization direction is perpendicular to the domain wall plane, as shown in Figure 1-13 (b). The DMI induces an effective field H_{DM} perpendicular to the domain wall plane, which favors a Néel type domain wall. When an in-plane field H_X is applied in a structure with DMI, if $H_X = H_{DM}$, the effect of DMI will be cancelled out to favor a Bloch wall. As a result, the velocity driven by perpendicular field will reach its minimum. Therefore, the applied H_X could be regarded as the DMI effective field.

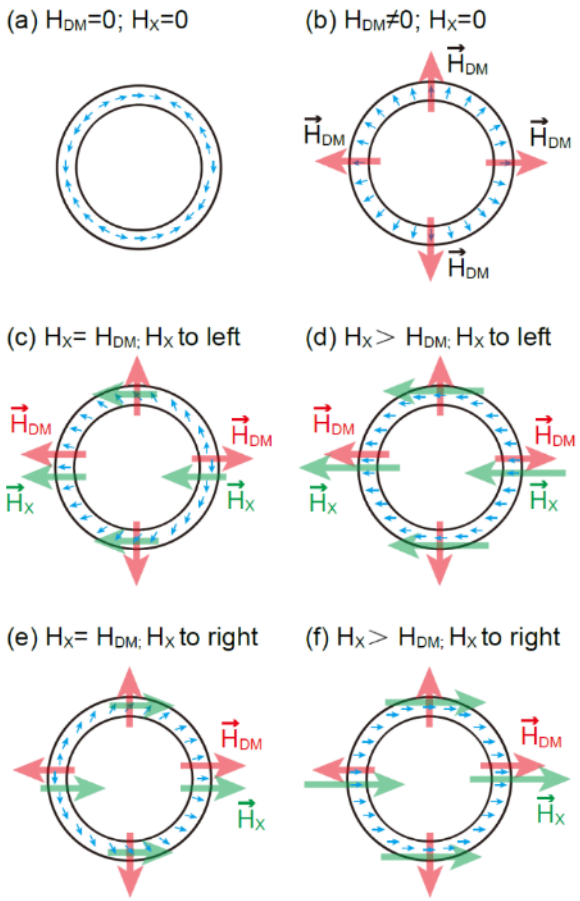

Figure 1-13 Magnetization of domain wall with different DMI strengths and in-plane fields H_X. (a) No DMI without H_X; (b) Strong DMI without H_X; (c) H_X applied toward the left and equals to the DMI effective field H_{DM}; (d) H_X applied toward the left and larger than the DMI effective field H_{DM}; (e) H_X applied toward the right and equals to the DMI effective field H_{DM}; (f) H_X applied toward the right and larger than the DMI effective field H_{DM}. The blue arrow represents the magnetization direction of the domain wall; the red arrow represents the direction of H_{DM}; The green arrow represents the direction of H_X.

In materials without DMI, the interfacial energy of domain wall γ_{DW} is as follows:

$$\gamma_{DW} = 4\sqrt{A_{ex}K_{eff}} \tag{1.8}$$

In sample with DMI, γ_{DW} can be expressed as:

$$\gamma_{DW} = 4\sqrt{A_{ex}K_{eff}} - \pi D \tag{1.9}$$

1.2.2 Domain wall motion regimes

Domain walls could be driven by several excitations including magnetic field [MET07], polarized current [KOY11, RYU13, EMO13, YAN15], spin wave [TAT04, KIM12,

WAN14], thermal gradient [SCH14], electric field [SCH12, FRA15], light [QUE18], etc. Magnetic-field-induced domain wall motion is the basic method to study the rich dynamics of domain wall motion. The research on current-induced domain wall motion has started from the discovery of STT effect. Ever since, spin-polarized current has become the most promising way to manipulate domain wall motion for future applications.

The dynamics of domain wall motion is usually divided into three different regimes (Figure 1-14): a low velocity creep regime where the DW interacts very strongly with pinning defects, a depinning transition regime and a high velocity flow regime [MET07]. Due to the presence of structural inhomogeneities (grain boundaries, grain texture, interface roughness, interface intermixing…), a spatial distribution of magnetic properties is present in the films, which results in a spatial distribution of DW energy responsible for pinning. At zero temperature, a minimum depinning field H_{dep} has to be applied to move the pinned DWs. At $T > 0$ K, DWs can move even at $H_{ext} < H_{dep}$ by thermal activation. In the very low field regime, the thermally activated behavior is described by the very well know creep law corresponding to the competition between an elastic energy (DW energy) and random disorder under a low driving force:

$$v = v_0 \exp[-(\frac{U_c}{k_B T})(\frac{H_{dep}}{H_{ext}})^{\mu}] \tag{1.10}$$

where U_c is the pinning energy barrier, k_B is the Boltzmann constant, T is the temperature, v_0 is the initial velocity, $\mu = 1/4$ is a universal exponent corresponding to the motion of 1D interface (ultra-thin PMA film) in a 2D random disorder.

For $H_{ext} > H_{dep}$, the dynamics of DW motion can be described by an intermediate depinning regime. When H_{ext} equals to H_{dep}, the velocity is given by:

$$v(H_{dep}, T) = v_T(\frac{T}{T_d})^{\psi} \tag{1.11}$$

and when the temperature is near zero:

$$v(H_{ext}, T \ll T_d) = v_H \left(\frac{H_{ext} - H_{dep}}{H_{dep}}\right)^{\beta} \tag{1.12}$$

where v_T and v_H represent the depinning velocities, T_d is the temperature related to the pinning strength, β and ψ are constant [PAR17].

When $H_{ext} >> H_{dep}$, the DW move in the flow regime that can be divided into three regimes: the steady regime, an intermediate chaotic regime above the Walker field H_W and a precessional regime.

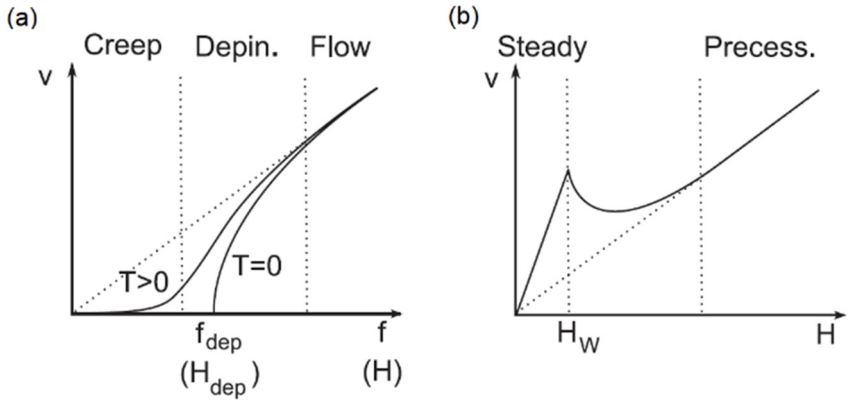

Figure 1-14 (a) The creep, depinning and flow regimes of domain wall motion. The domain wall velocity *v* is driven by a force *f* (magnetic field *H*) at a finite temperature *T*. (b) Regimes of flow motion. The steady and precessional flow regimes are separated by the Walker regime characterized by the Walker field H_W [MET07].

1.2.3 Current-induced domain wall motion

1.2.3.1 Current-induced domain wall motion based on STT

Domain wall motion along nanowires can be driven by spin-polarized current. Current-induced domain wall motion driven by STT was first proposed by *Berger et al.* [BER84]. When a polarized current goes through domain walls, the spin angular momentum of conduction electrons is transferred to the magnetization of the DWs and exerts a torque on the magnetization, which induces their motion. The STT contribution usually consists of two terms. First, the adiabatic component is given by [LI04, BOU11]:

$$\begin{cases} \vec{\tau}_{ad} = (\vec{u} \cdot \vec{\nabla})\vec{m} \\ u = \dfrac{\mu_B g P J}{2 e M_S} \end{cases} \tag{1.13}$$

where μ_B is the Bohr magneton, g is the Laudau factor, P is the polarization, J is the current density and e is the elementary charge.

Then, the nonadiabatic component can be expressed as [ZHA04, THI05]:

$$\vec{\tau}_{na} = \xi[\vec{m} \times (\vec{u} \cdot \vec{\nabla})\vec{m}] \tag{1.14}$$

where is ξ is the nonadiabatic constant.

Both adiabatic and nonadiabatic components may play a significant role in the DW motion [LEG17], but their respective origin is still under discussion. The nonadiabatic term proportional to the current density J acts as an effective field H_{STT} [BOU08].

1.2.3.2 Current-induced domain wall motion based on SOT

Emori *et al.* have found that the combination of DMI and SOT can enable current-induced domain wall motion in Pt/CoFe/MgO and Ta/CoFe/MgO perpendicularly magnetized heterostructures [EMO13]. Figure 1-15 (a) shows domain wall motion in Pt/CoFe/MgO wires. First, the DMI at the interface of Pt/CoFe favors a left-handed Néel type domain wall. When current is injected in the x direction, the SHE in the Pt layer induces spin accumulation along the y direction, which in turn creates a torque on the chiral DWs. The domain wall moves against the current direction, which is opposite to the domain wall motion induced by STT [MOO08, UED15]. With the stabilization of Néel type domain wall in heterostructures due to DMI, SOT can induce DW motion at higher speed. Figure 1-15 (b) illustrates the domain wall velocity as a function of current density and magnetic field along the z direction. The effect of current on domain wall motion is the same as that of magnetic field, which suggests that the effective field of SHE induced by the current is along the z direction. The domain wall motion in Ta/CoFe/MgO structure is in the direction of electrons flow, which can be explained by the opposite spin Hall angle of Ta compared to Pt [LIU12] that induces an effective field of SHE in the opposite direction compared to Pt/CoFe/MgO structure.

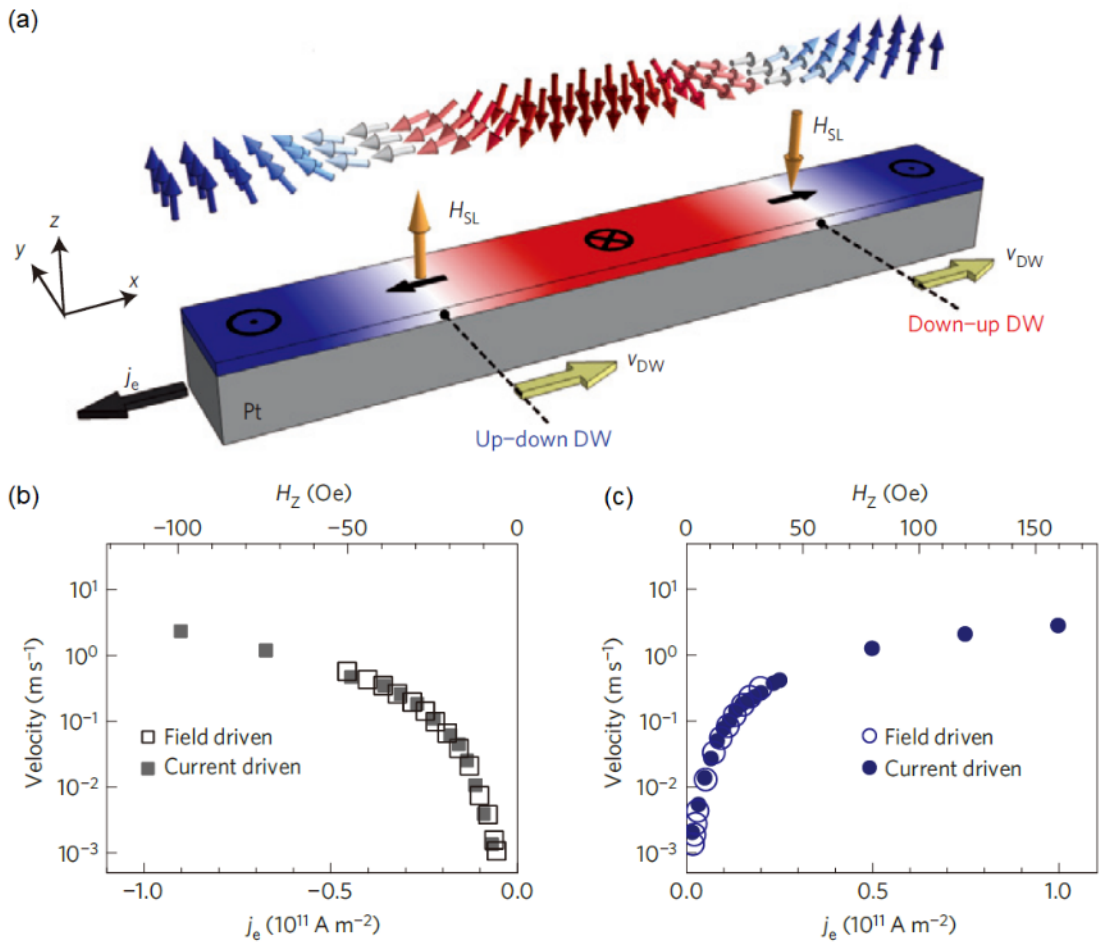

Figure 1-15 (a) Schematic of domain wall motion driven by SOT in Pt/CoFe/MgO wires. The effective field H_{SL} moves the domains in the direction against the j_e with the velocity v_{DW}. (b-c) Domain wall velocity as a function of j_e and applied perpendicular field H_z in (b) Pt/CoFe/MgO and (c) Pt/CoFe/MgO wires [EMO13].

1.2.4 Domain wall motion in Co/Ni multilayers

Co/Ni multilayers have been explored as a very promising system for current-induced domain wall motion. Current-induced domain wall motion in Co/Ni multilayers was first explored by Ravelosona *et al.* in nanowires based on sputtered [Co/Ni] spin valves showing PMA, as Co/Ni multilayers provides higher spin-torque efficiencies [RAV07]. The same structure was used to explore the current-induced domain wall motion by STT, where the non-adiabatic torque dominates the domain wall depinning and creep motion [BUR09]. In 2011, Koyama *et al.* found an "intrinsic pinning" phenomenon by demonstrating the wire width dependence of the threshold current density, where the depinning process is driven by the adiabatic torque in sputtered Co(0.2 nm)/[Ni(0.6

nm)/Co(0.2 nm)]$_4$ nanowires. They also confirmed the intrinsic nature of current-induced domain wall motion by showing that the threshold current density is independent of the external magnetic field and the temperature [UED11, YOS12]. Current-induced domain wall motion was further explored in epitaxial [Co/Ni] multilayers consisting of Al_2O_3/V(5 nm)/Au(1 nm)/Ni(0.2 nm)/[Co(0.5 nm)/Ni(0.6 nm)]$_3$/Au(1.2 nm), where both adiabatic and nonadiabatic components of the STT play a role in the domain wall motion [LEG17]. In 2013, Ryu *et al.* observed domain wall motion in the direction against the electron flow in a perpendicularly magnetized Co/Ni/Co tri-layered wires, which is in the opposite direction of the traditional current-induced domain wall motion by STT. As the Co/Ni/Co layers are sandwiched between Pt layers, the SHE arising from the Pt layer generates spin accumulation and induces a spin-orbit torque on the Co/Ni/Co layers. In addition, the DMI due to the structural inversion asymmetry of the film structure stabilizes a Néel wall structure. Therefore, current-induced domain wall motion driven by SOT has been observed Co/Ni multilayers [RYU13]. In 2015, a velocity up to 750 m/s for current-induced domain wall motion driven by SOT and DMI can be obtained in a synthetic antiferromagnet, which is formed from two perpendicularly magnetized Co/Ni multilayers separated by an ultrathin coupling layer of Ru. This phenomenon is due to the exchange coupling torque that is directly proportional to the strength of the antiferromagnetic exchange coupling between the two sub-layers, in addition to the stabilization of the Néel domain wall structure [YAN15].

1.3 All-optical switching

In 1996, Beaurepaire *et al.* demonstrated ultra-fast demagnetization in ferromagnetic thin film using ultrafast laser pulses, which raised the interest of the researchers. They observed the ultrafast demagnetization of Ni thin films within 1 picosecond (ps) by femtosecond (fs) laser pulses [BEA96]. As the demagnetization duration is much smaller than the spin precession time of around 100 ps, the performance of magnetic memory may be improved greatly. Hereafter, the ultrafast demagnetization of other

magnetic materials has been found, such as 3*d* ferromagnetic metals and rare-earth magnetic metals. All-optical helicity-dependent switching (AO-HDS) was then demonstrated in 2007 by Stanciu *et al.* in Radboud University, where left-circularly (σ-) or right-circularly (σ+) polarized fs laser pulses can deterministically switch the magnetization of perpendicularly magnetized $Gd_{22}Fe_{74.6}Co_{3.4}$ thin films to the up or down direction [STA07]. In 2011, Radu *et al.* discovered a magnetization switching in $Gd_{25}Fe_{65.9}Co_{9.4}$ by a single 60-fs linearly-polarized laser pulse, which can be called as all-optical helicity-independent switching (AO-HIS) [RAD11].

The differences between AO-HIS and AO-HDS are that: AO-HIS can realize magnetization switching with a single pulse independent of the laser helicity, while AO-HDS needs multiple pulses and the magnetization switching direction depends on the helicity. AO-HIS occurs only in ferrimagnetic materials containing Gd, while the materials for AO-HDS was found to be broader when it was observed in ferromagnetic multilayers as Co/Pt and Co/Ni, rare-earth metals as CoTb and CoDy, FePt granular films, etc. [LAM14, MAN 14] Recently, transparent ferrimagnetic dielectric was also found to be appropriated for all-optical switching [STU17]. These researches provide rich material choices for the application of all-optical switching in the magnetic storage and move one step closer to the application of all-optical switching.

AO-HDS has the advantages of faster writing speed and lower power consumption, compared to the current magnetic storage [ELH17]. Instead of magnetic field or current, the use of laser helicity for magnetization switching of magnetic materials lays a foundation for the realization of magnetic storage with all-optical switching based on ultrafast laser. Therefore, all-optical switching can be an important approach for the realization of novel magnetic memory, magnetic sensors and magnetic logic devices, which reveals broad application potentials and great commercial values in the near future.

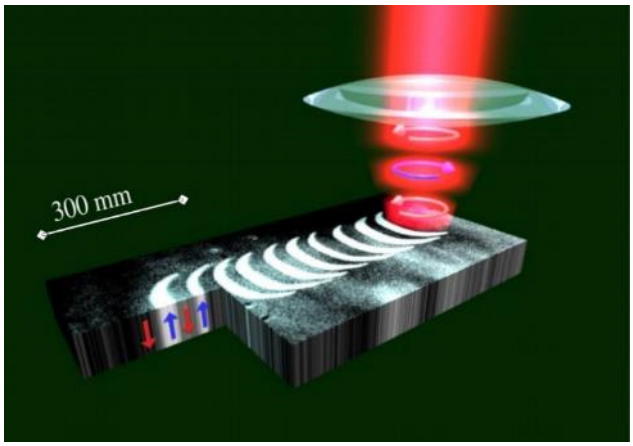

Figure 1-16 Schematic of magnetic storage based on all-optical switching. Circularly polarized laser beam sweeps the magnetic storage medium to write the up and down magnetic domains [STA07].

1.3.1 All-optical helicity-dependent switching in ferromagnetic materials

1.3.1.1 Experimental observation

In 2014, Lambert *et al.* investigated a variety of ferromagnetic multilayers with PMA, which are widely used for the future spintronics memory and logic [LAM14]. They observed the all-optical switching in these materials, which depends strongly on the number of repetitions and the thickness of the ferromagnetic layers. Figure 1-17 shows the results for $[Co(0.4\ nm)/Pt(0.7\ nm)]_N$ multilayers with N = 8, 5 or 3. Thermal demagnetization (TD) was observed for the samples with N = 8 or 5, where multi-domains were formed in the laser sweeping region regardless of the laser helicity, while helicity-dependent all-optical switching was obtained for the sample with N = 3. Figure 1-17 (d) shows the laser power dependence with static laser beam. With increased power, TD appeared with a laser heating above the Curie temperature. With decreased power, σ+ switches the film while σ- has no effect. The same results were also obtained in [Co/Pd], $[Co_{1-x}Ni_x/Pt]$ and [Co/Ni] ferromagnetic multilayers with proper N, thickness and power, which confirm the all-optical switching in a wide range of ferromagnets.

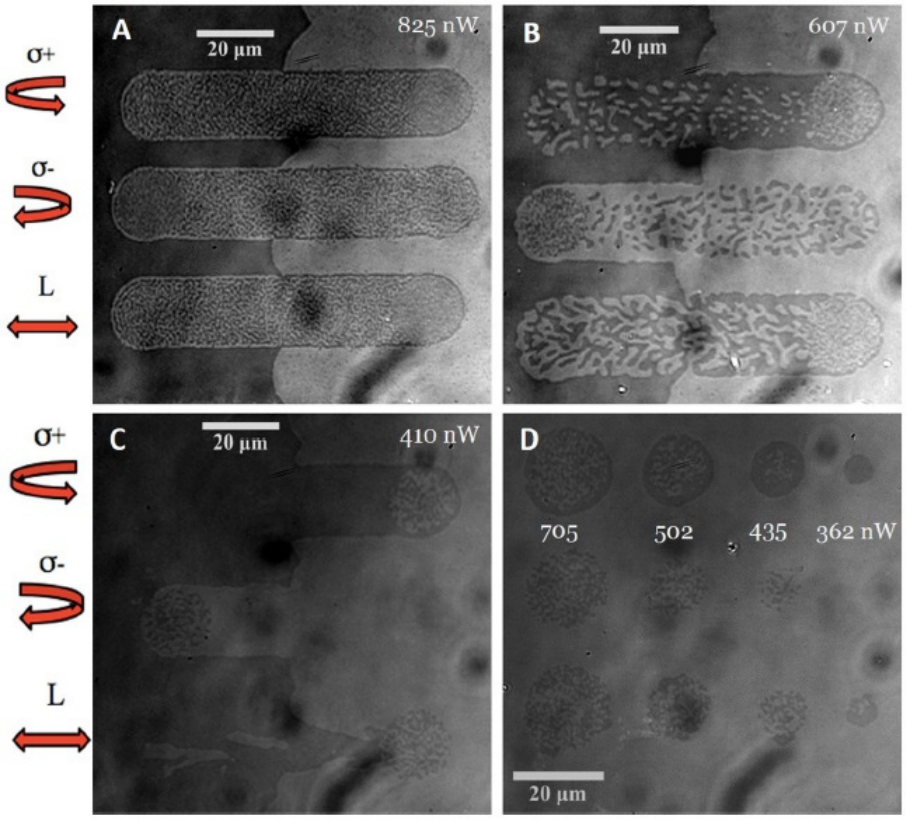

Figure 1-17 (a-c) Kerr images of [Co(0.4 nm)/Pt(0.7 nm)]$_N$ multilayered samples, where (a) N = 8, (b) N = 5, (c-d) N = 3. For (a-c), left-circularly (σ-) or right-circularly (σ+) polarized laser beams are swept over a region of the sample, while for (d), laser beam was fixed at individual spots over a region of the sample with different laser powers [LAM14].

1.3.1.2 Influence of magnetic domain size

In 2016, El Hadri *et al.* investigated the thickness dependence of helicity-dependent all-optical switching in ferromagnetic multilayers, e.g. [Co/Ni], which showed the role of domain size on the helicity-dependent all-optical switching [ELH16]. By reducing the number of repetitions N, the total magnetic layer thickness was reduced and helicity-dependent all-optical switching was observed. The thickness is related to the stable magnetic domain size with the following equation:

$$D = t\exp[\frac{\pi D_0}{2t} + \ln\pi - 1 + \mu(\frac{1}{2} - \ln 2)] \quad (1.15)$$

where $D_0 = \sigma/E_d$ is the dipolar length and $\mu = 1 + E_d/K_u$ is the magnetic susceptibility. $E_d = \mu_0 M_S^2/2$ is the demagnetizing energy per unit volume, $\sigma = 4(A_{ex}K_u)^{1/2}$ is the domain wall energy per unit surface, $K_u = H_K M_S/2$ is the effective anisotropy, and t is the

magnetic thickness.

As a result, if the domain size at room temperature is larger than the laser spot size, helicity-dependent all-optical switching can be achieved.

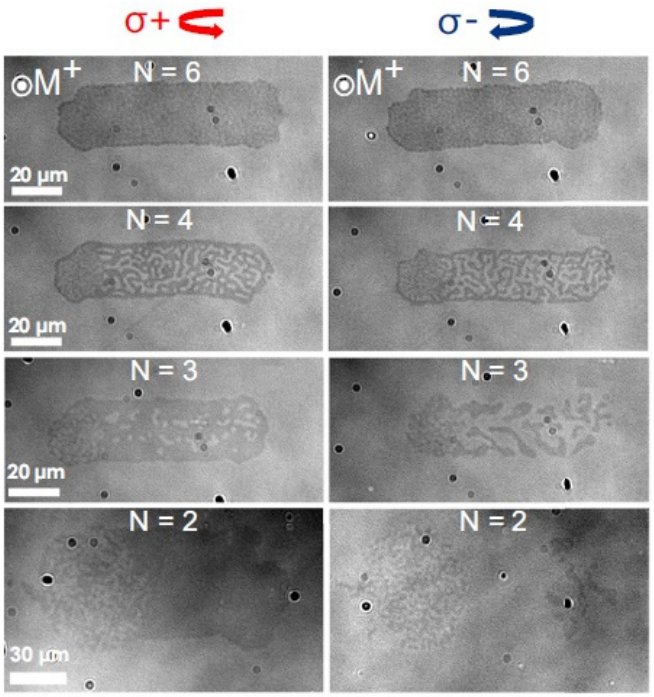

Figure 1-18 Kerr images of $[Co(0.2\ nm)/Ni(0.6\ nm)]_N$ multilayered samples with N from 2 to 6, where left-circularly (σ-) or right-circularly (σ+) polarized laser beam are swept over a region of the sample [ELH16].

1.3.1.3 Mechanism and modeling

The physical origin of all-optical switching comes from the electron-spin interactions on ultrafast scales. The exploration of physical mechanism of all-optical switching concentrates on the effect of the laser pulses, which brings heat and angular momentum to the system. For the ultrafast switching, in 2012, the research group in Radboud University reported the helicity-independent all-optical switching in the same material system [KHO12] where they found the helicity-dependent all-optical switching in 2007 [STA07]. The temperature also affects the all-optical switching, as the process of magnetization switching usually requires the heating of metal electrons beyond the Curie temperature, while the magnetic anisotropy and the magnetization of the material change during the variation of the temperature. Two mechanisms have been proposed to explain the AO-HDS, either the inverse Faraday effect (IFE) or the magnetic circular

dichroism (MCD), and several other parameters also play important roles in the process: transport of hot electrons, transfer of spin angular momentum, and the heat transfer, etc. [MAL08, ESC13, BAT14, BER16, COR16, GOR16] The light absorption in the multilayers, the evolution of electron & phonon temperatures, and the spin precession accompany the effect of laser pulses, which induces the interaction between electron, phonon and spin.

The IFE due to circularly-polarized light can lead to either an effective field or an induced magnetization, whose direction depends on the light polarization and is opposite for left-circularly (σ-) or right-circularly (σ+). In 2016, Cornelissen et *al.* developed a microscopic model for all-optical switching in ferromagnets based on the magnetic three-temperature model (M3TM), where the model describes the interactions between electron, phonon and spin [COR16]. Figure 1-19 shows the simulation results of the magnetic dynamics with the fs laser excitation in Co/Pt multilayers. While linear polarized laser induces only a magnetization quenching followed by a relaxation of magnetization, σ+ and σ- give a magnetization reversal to the up or down states. They also showed that a minimal IFE lifetime of 0.1 ps with an IFE field strength between 10 T and 24 T can achieve the all-optical switching.

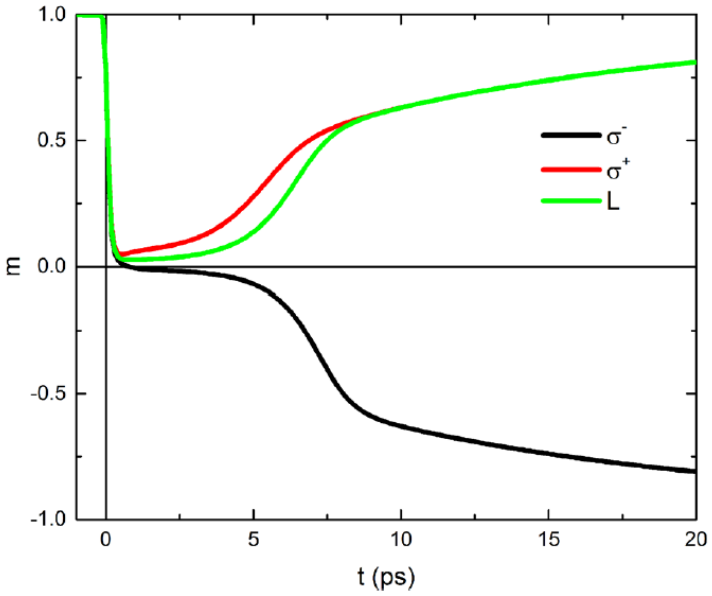

Figure 1-19 The variation of magnetization in regard to the time after the excitation of laser pulses with σ-, σ+ and L [COR16].

The MCD model is based on the fact that left-circularly (σ-) or right-circularly (σ+) polarized laser is absorbed differently for one orientation of the magnetization direction. In 2016, Gorchon *et al.* developed a model for multi-shot helicity-dependent all-optical switching in ferromagnetic materials based on a purely heat-driven mechanism [GOR16]. After the laser excitation, the laser pulse heats the magnetic sample close to the curie temperature T_C, which induces the decrease of magnetic anisotropy. Considering the MCD, the absorptions of light by domains with opposite magnetization directions are different, which induce a difference of magnetic stability. By proper MCD strength and proper heat by the light, stochastic switching happens in the hotter region. With accumulated laser pulses, deterministic magnetization reversal can be achieved, which depends on the laser helicity. Figure 1-20 shows the simulation results based on this model. Magnetization reversal is achieved for a finite number of laser pulses with a certain temperature difference ΔT, a proper laser power and a proper MCD value.

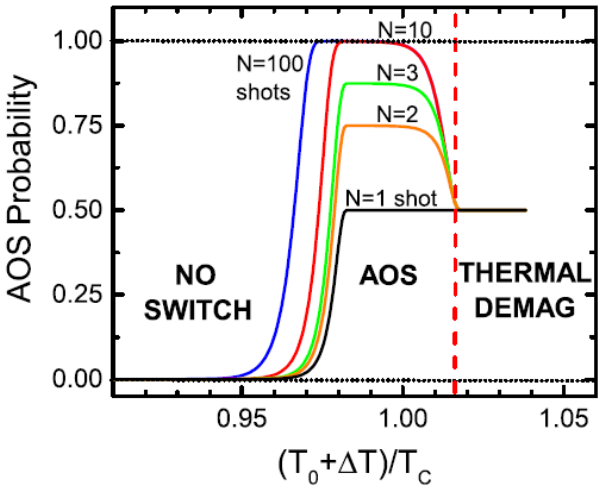

Figure 1-20 The probability of all-optical switching in regard to the laser temperature increase ΔT with different numbers of laser pulses. No switching is observed at low temperature, and all-optical switching takes place with a certain number of laser pulses as the temperature is close to T_C, while TD occurs at high temperature [GOR16].

The research on the mechanism of all-optical switching will promote the development of low-power spintronic storage and logic devices.

1.3.2 Helicity-dependent all-optical domain wall motion in ferromagnetic materials

In order to study the physics of domain wall motion and to provide alternative solutions for domain wall manipulation at low power consumption, several methods have been proposed, such as electric field [LAH12] and ultrafast optics [QUE18]. Indeed, ultrashort laser pulses provide an alternative way for magnetization manipulation [BEA96, STA07, KIR10, ELH17, LIU17]. All-optical helicity-dependent switching was observed in ferromagnetic multilayered thin films using circularly polarized light, where deterministic switching of magnetic states was achieved using laser helicity as a new degree of freedom. It has attracted significant interest because of its potential for the integration of ultra-low power all-optical writing in data storage industries [MAN14, LAM14, ELH16, ELH18, PAR18]. Moreover, fs laser provides a new way for controlling domain wall motion, where all optical helicity-dependent domain wall motion driven by fs laser pulses was demonstrated [QUE18].

Helicity-dependent all-optical domain wall motion was first explored by Yassine *et al.* in Co/Pt multilayers without applying magnetic fields [QUE18]. The ferromagnetic multilayers were glass/Ta(5 nm)/Pt(4.5 nm)/Co(0.6 nm)/Pt(0.7 nm)/Pt(3.8 nm) with PMA. The thin film structure was exposed to a femtosecond laser with a 5 kHz repetition rate, 800 nm wavelength, 40 fs pulse duration and 50 μm full width at half maximum (FWHM). The laser power is below the all-optical switching threshold of 14.5 mJ/cm^2. As shown in Figure 1-21, the laser beam spot is centered on the domain wall and the laser helicity determines the displacement direction of the domain wall motion.

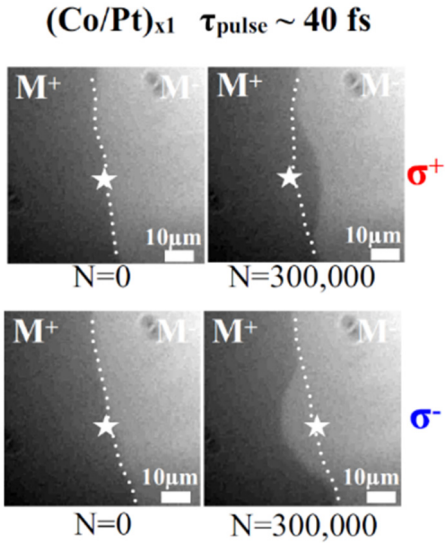

Figure 1-21 Kerr images of domain wall motion in [Co(0.6 nm)/Pt(0.7 nm)] induced by 40 fs left-circular (σ−) and right-circular (σ+) polarized laser pulses. The star indicates the laser beam center and N is the number of laser pulses. The laser beam spot is centered on the wall and the dotted line shows the initial position of the domain wall before the laser exposure [QUE18].

The microscopic origin of this effect can be explained by both IFE and MCD effects. For IFE, the effective field of σ+ induces a domain wall motion for a propagation towards M↓ (M-) domains, while the effective field of σ- induces a domain wall motion for a propagation towards M↑ (M+) domains. For MCD, σ+ induces a hotter region in the M↓ (M-) domains that produces an effective field of MCD and enables the domain wall towards M↓ (M-) domains, while σ- induces a hotter region in the M↑ (M+) domains that produces an effective field of MCD and enables the domain wall towards M↑ (M+) domains.

The authors use the Fatuzzo-Labrune model [FAT62, LAB89] to calculate the DW velocity as well as the DW displacement considering the magnetic relaxation under the assumption of IFE effective field. The model gives the energy needed when an effective field H_{eff} is applied to overcome the pinning energy barrier E and to move the DW within the Barkhausen volume V_{B}, as shown in Eq. (1.16):

$$v = v_0 \exp\left(-\frac{E - 2H_{\text{eff}} M_{\text{S}} V_{\text{B}}}{k_{\text{B}} T}\right) \tag{1.16}$$

1.4 Summary

In this chapter, we have reviewed the concepts and development of MRAM, domain wall motion and all-optical switching. We have distinguished two types of all-optical switching, including AO-HDS and AO-HIS. In particular, we have highlighted the current-induced domain wall motion in Co/Ni multilayers that is widely explored for racetrack memory, and the recent domain wall manipulation with femtosecond laser, which provides a possible way for ultra-low power manipulation of domain walls combining laser and current.

CHAPTER 2 EXPERIMENTAL TOOLS AND SAMPLES

In this chapter, I will first introduce the samples production flow, including thin film deposition, magnetic characterization, microwire fabrication, and then the domain wall motion experiments, including Kerr microscopy and the use of laser and current excitations to drive domain walls.

2.1 Sample deposition and fabrication

In my Ph.D. thesis, I have used different films stacks grown by different deposition techniques including magnetron sputtering and molecular beam epitaxy. I have also used a specific nanofabrication process to develop the microwire for the domain wall motion experiments.

2.1.1 Magnetron sputtering

The sputtering technique is a standard physical vapor deposition (PVD) process to produce high quality magnetic thin film with high production efficiency, strong film adhesion and atomic precision. During the sputtering process, the inert gas in the deposition chamber, usually the argon, will be ionized within an Ar+ plasma. Then, Ar+ ions move toward the cathode under the acceleration of the electric field, and bombard the target material that is deposited on the substrate.

A sputtering process includes the following steps:

1. The inert gas (argon) is ionized within a plasma;
2. The Ar+ ions accelerate under electric field toward the target;
3. The Ar+ ions bombard the surface of the target and the atoms of the material are sputtered from the surface of the target.
4. The sputtered material atoms move towards the substrate in front of the target.

5. The atoms hit the substrate surface to form a film

Figure 2-1 shows the schematic of a thin film deposition process. The conductive target, such as metal, can be deposited with a direct current (DC) power supply, while a radio frequency (RF) power supply is used for the sputtering of insulator target, such as oxides. The base pressure is usually around 10^{-8} Torr while the Ar+ pressure during the deposition is around 10^{-3} Torr.

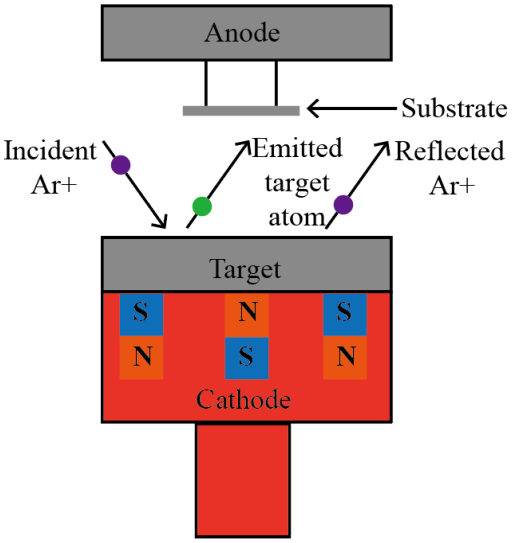

Figure 2-1 Schematic of a thin film deposition process.

In order to increase the plasma efficiency in the chamber, a magnetic field can be added in the cathode to trap the electrons, which increases the probability of collision between electrons and the inert gas. Such magnetron sputtering can promote the ionization of the gas and increase the probability to induce a plasma at low Ar pressure. In addition, the low Ar pressure decreases the gas impurity content and reduces the collision between the Ar+ ions and the material. Figure 2-2 shows a typical magnetron sputtering system and the sputtering process of a metal target.

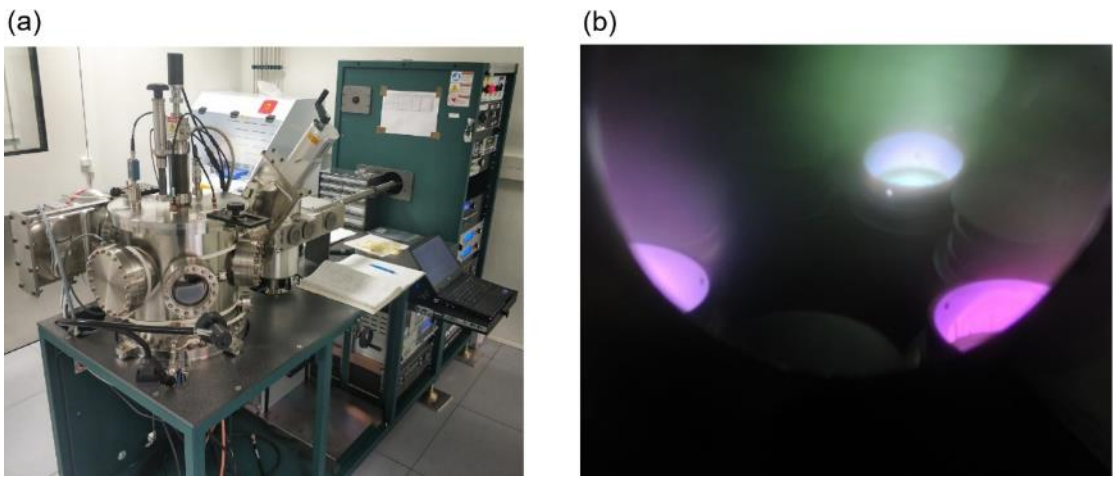

Figure 2-2 (a) Magnetron sputtering system. (b) The sputtering process of a metal target showing the Ar plasma.

Magnetron sputtering is a very versatile film deposition technique, which provides an efficient method to deposit thin magnetic films and multilayers down to a few Angstrom thickness. The films are usually textured with a preferential crystalline direction along the growth direction.

The first set of samples grown by magnetron sputtering in my Ph.D. thesis are made of Pt/Co/heavy metal (HM) tri-layer with a 0.8-nm-thick Co layer sandwiched between a 3-nm-thick Pt layer and a 2-nm-thick HM capping layer, where the capping HM materials are W, Ta or Pd. The stacks were prepared using a Ta (2 nm) seed layer, which ensured the (111) texture of Pt, while the top Pt (3 nm) film forms a protective layer preventing the oxidation of the films.

The second set of samples used in my work are [Co/Ni] multilayers made of Ta(3 nm)/Pt(x nm)/Co(0.3 nm)/Ni(0.6 nm)/Co(0.3 nm)/Pt(y nm) deposited on glass substrates. The Ta (3 nm) seed layer allows good adherence of deposited layers on the glass and ensures the (111) texture of the multilayers.

2.1.2 Molecular Beam Epitaxy (MBE)

MBE is a technique for the epitaxial growth of thin layers of metals, semiconductors or insulators. The term epitaxy comes from the Greek "epitaxis" which means "order from above". We speak of epitaxy when material A manages to find a crystallographic

arrangement with respect to the surface grid of the monocrystalline support B. The deposit of A can then also grow in the form of monocrystal. Epitaxy is therefore a relationship of crystalline order between the support material (the substrate) and the material deposited on this substrate.

In the same way that the water vapor condenses on a glass, the MBE can induce a material vapor that can condense on a substrate. There are several methods to create this vapor: evaporation cells (materials in a crucible are heated above their evaporation temperature), electron guns (bombardment of the material surface induces evaporation of the material) and laser ablation (materials locally heated by a pulse laser beam).

This process of evaporation occurs in a chamber where there is a high vacuum in the order of 10^{-11} Torr, to slow down any pollution of the surface by residual gases (O_2, N_2, CO, CH_4 and H_2 mainly). For example, it takes 10 hours at a pressure of 10^{-10} Torr to cover a surface of 1 cm² with a monolayer of oxygen. An example of an ultra-vacuum system can be seen in Figure 2-3.

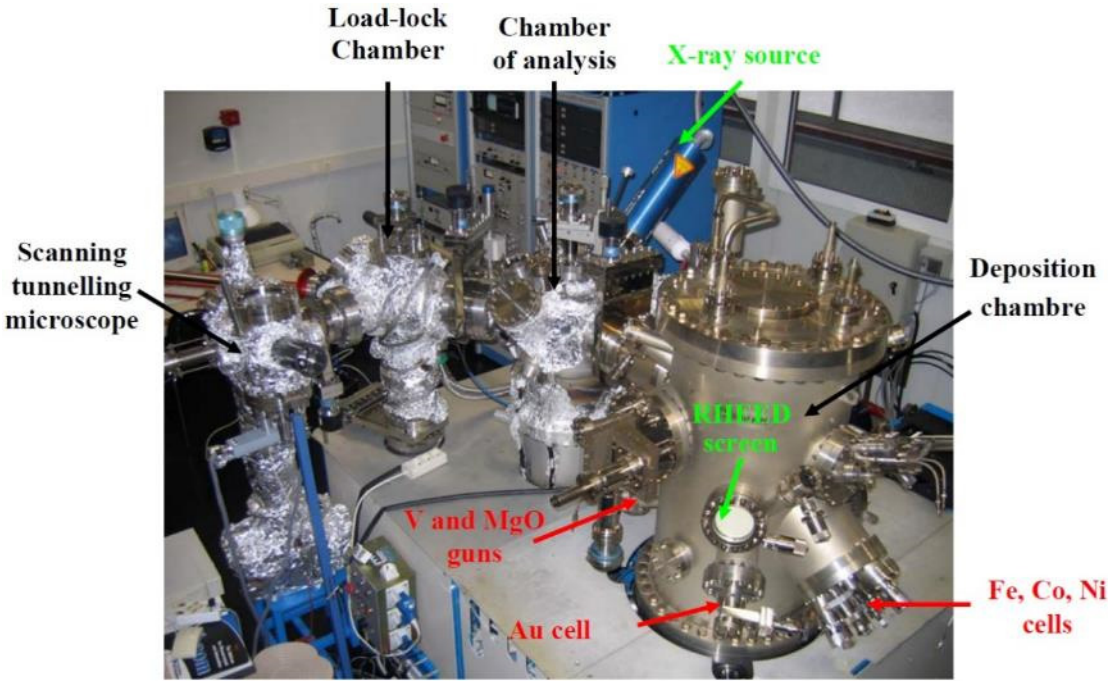

Figure 2-3 Molecular beam epitaxy system.

Surface diffraction reflection high energy electron diffraction (RHEED) is an extremely powerful *in situ* characterization tool. It gives access to crystallographic and

morphological information of the surface during the MBE growth. Thanks to the RHEED oscillations, it also allows the identification of the growth mode, to perform a very accurate calibration of the deposition rates and to determine the variations of the parameter in the growth plane.

The principle of RHEED is simple: a grazing incidence high-energy mono-kinetic beam of electrons (10 to 40 keV) is reflected on the surface of the sample. The diffracted beam, arising from the constructive interferences between the waves scattered by the periodically arranged atoms, forms a diffraction pattern. The diffracted beam is then detected on a fluorescent screen (Figure 2-4).

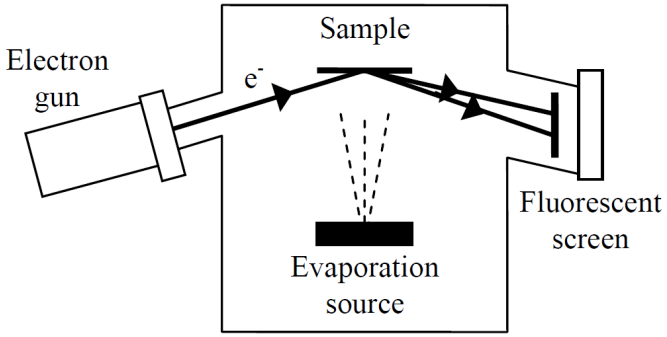

Figure 2-4 Characterization of the crystallographic structure using the RHEED technique.

When the sample is rotated with respect to the normal of the surface, the diffraction patterns corresponding to each crystallographic row are obtained as a function of the angle. With the data of the angles between the different RHEED plates and the distance between diffraction lines, it is possible to obtain the structure of the surface. Surface diffraction RHEED also allows the control of the structure's crystallographic quality (roughness, faceted islands, ...). Indeed, in the case of a smooth surface, it is in the conditions of a diffraction on a two-dimensional system that will give rise to diffraction rods. When the surface becomes rough, we see a diagram of specific points of 3D diffraction superimposed on the 2D rod diagram.

The third set of thin films used in my research are epitaxial stacks of V (5 nm)/Au (6 ML)/Ni (x ML)/[Co (x ML)/Ni (y ML)]$_N$/Au (5 ML) grown by MBE on a single-crystalline sapphire substrate that is priorly outgassed *in situ* (ML represents

monolayer). The seed layer of V provides a good adhesion of the deposited layers on the sample. The Au layer is annealed at 700 K after its deposition at room temperature, which ensure the smoothness of this layer. V and Co are deposited by an electron gun, while Au and Ni are evaporated by the Knudsen cells at 1550 K and 1625 K. The crystalline structures and the deposited rates of Au and Ni layers have been verified by RHEED during the process, as shown in Figure 2-5.

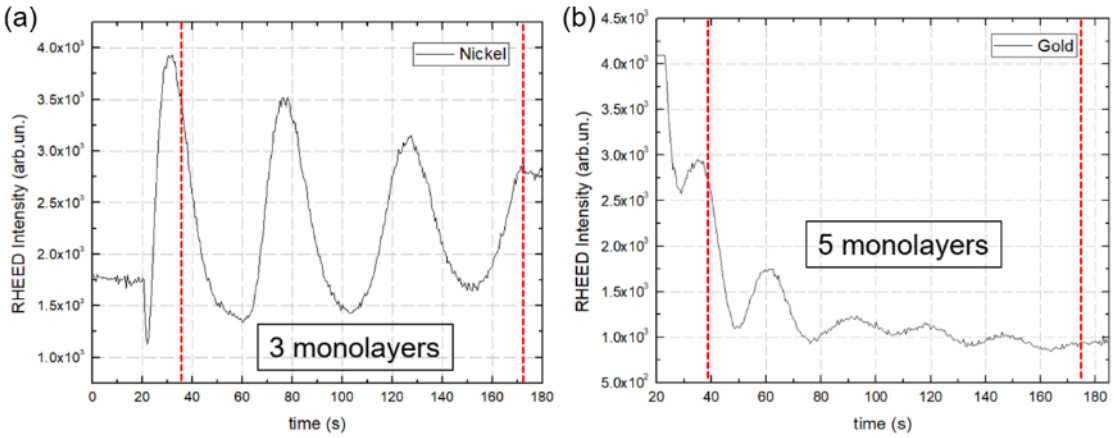

Figure 2-5 RHEED intensity oscillations recorded during the growth of (a) the first Ni (3 ML) layer and (b) the last Au (5 ML) layer of V (5 nm)/Au (6 ML)/Ni (3 ML)/[Co (3 ML)/Ni (3 ML)]2/Au (5 ML) structure.

2.1.3 Magnetic characterization

After the thin film deposition, magnetic characterization is conducted. The coercivity (H_c), the saturation magnetization (M_S) and the direction of magnetization, which are 3 important factors for the magnetic properties, can be measured by vibrating sample magnetometer (VSM). During the VSM measurement, samples are first saturated by a strong magnetic field. Then, sinusoidal physical vibration is applied by a piezoelectric material. The induced voltage can be sensed by a built-in coil and amplified by the lock-in amplifier, which is proportional to the magnetization of the measured sample. The induced electromotive force in the detective coil originates from the change of the magnetic dipolar field that is proportional to the sample magnetization. Therefore, the magnetization $M = kV$, where V is the measured voltage and k is a constant which can be calibrated by a standard sample [FON56, FON 59]. By sweeping the magnetic field, the hysteresis loop of the sample can be obtained.

The measurement accuracy of VSM is around 10^{-5} to 10^{-6} emu. In order to measure samples with weak magnetic signal, Superconducting Quantum Interference Device (SQUID) can be used, as shown in Figure 2-6. A superconducting coil allows the application of magnetic fields ranging from -7 to 7 Tesla and a cryostat allows the application of temperatures ranging from 1.5 K to 400 K. The measurement is based on the flux quantization and the Josephson effect (quantum tunneling). The key component is a superconducting loop with Josephson junctions, which is used to detect the flux change and to convert the flux change into voltage. Two superconductors are separated by a thin tunneling barrier, which forms the Josephson junction. When the junction is biased by a proper current, a macroscopic quantum interference is induced, where the voltage across the junction is proportional to the flux change in the superconducting loop. The sensitivity of SQUID can reach 10^{-8} emu. However, the measurement speed is relatively low.

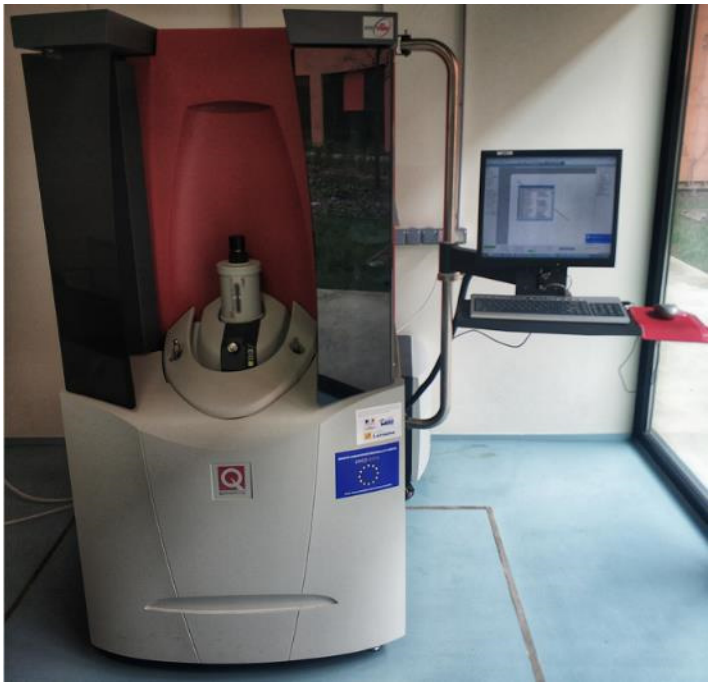

Figure 2-6 SQUID-VSM from Quantum Design, Inc.

Alternating gradient magnetometer (AGM) measures the force generated by the magnetic sample under non-uniform magnetic field to obtain the sample's magnetic moment, which also has high sensitivity up to 10^{-8} emu. The gradient coils in

conjunction with the electromagnet produce alternating gradient field, and the periodic alternating electromagnetic force is applied on the sample. This applied force is proportional to the alternating gradient field and the magnetic moment of the sample. By transferring from the quartz sample holder to the compact transducer, the force signal can be converted into voltage signal. AGM has high sensitivity and fast measurement speed, but the sensitivity decreases to 10^{-5} emu in high or low temperature environment.

2.1.4 Optical lithography

In order to fabricate microwires for our experiments, the thin films are patterned into wires using ultraviolet (UV) lithography and ion beam etching (IBE). The metal electrodes are obtained via lift-off technique after a second UV lithography and the deposition of an electrode metal film by electron beam evaporation.

During the microwire fabrication process, the lithography is the most important and difficult step, to realize the minimum feature size of the patterns. Figure 2-7 shows the MJB4 machine from SUSS MicroTec company, which is used for the lithography of micrometer device.

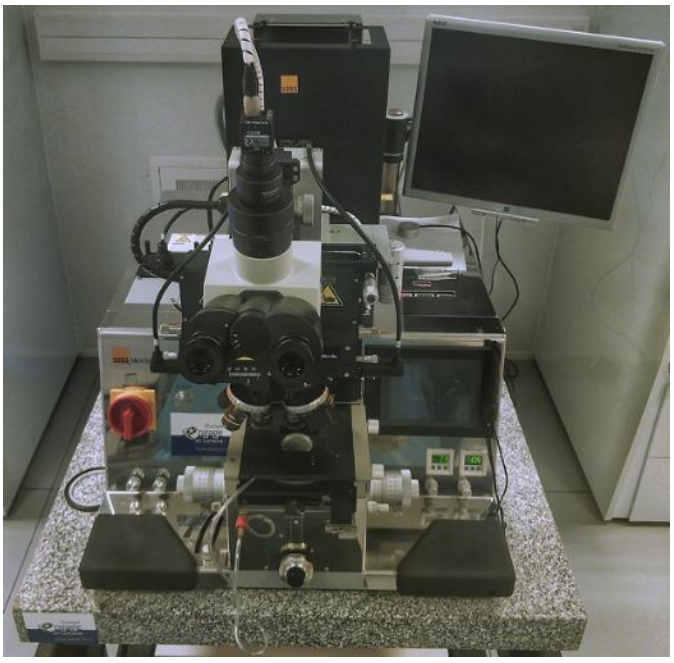

Figure 2-7 UV lithography mask aligner MJB4 from SUSS MicroTec.

UV lithography utilizes the UV light to pattern the photoresist spinned on a thin film or substrate. The photoresist is an organic material whose solubility can be changed after radiation using UV light or ion beam. Using spin coating, the photoresist is deposited uniformly on the thin film with the centrifugal force generated by high-speed rotation. The photoresist can be divided into two categories: positive or negative. For the former, the region exposed to the UV is dissolved in the developer, whereas for the latter, the region exposed to the UV is kept after the developing process.

Figure 2-8 Spin coater SPIN150 from SPINCOATING.

The process is based on transferring the pattern from the lithography mask to the photoresist. The pattern on the lithography mask is made of opaque chromium metal area. Similar to a photography process, during the optical lithography process, the properties of the photoresist are changed under the UV light. Then, the chemical developing process in a specific developer removes part of the photoresist, depending on whether it is positive or negative.

2.1.5 Ion Beam Etching (IBE)

The ion beam etching process enables the transfer of pattern from the photoresist to the substrate (or thin films). IBE is an anisotropy dry etching technology using energetic argon ions. During the IBE process, electrons are used to induce an Ar+ plasma. Then, the argon ion beam is accelerated to bombard the sample, where the photoresist serves

as a mask. The area that are not protected are etched down to the substrate.

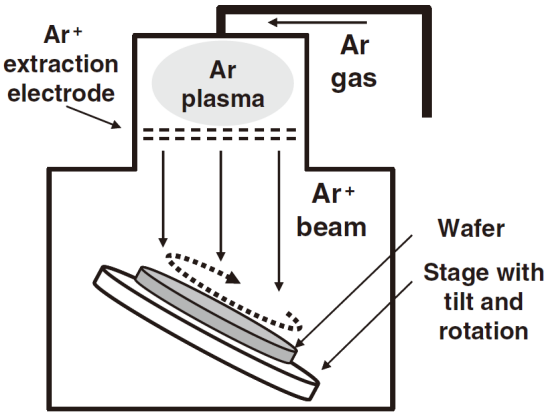

Figure 2-9 Schematic of the IBE process [SUG09].

Although the argon ions have good directionality, as the selectivity of the physical etching is relatively poor, the etch-resistant capability of the photoresist should be considered. In the meantime, as redeposition phenomenon is observed during the IBE process, the etching tilt angle should be optimized. The choice of the end point for the etching process is a crucial factor. Secondary ion mass spectroscopy (SIMS) is usually used for the end-point detection. Figure 2-10 shows the IBE system with SIMS detection that I have used during my Ph.D.

Figure 2-10 Planetary Etch System (PSIBE) from 4wave.

After the IBE process, the photoresist is removed using a specific chemical remover, and a second UV lithography steps as well as a dissolution in the developer is conducted before the deposition of the electrodes. The alignment process between the first and second lithography process is crucial, as minor alignment error will induce misalignment of the whole pattern. As a result, alignment marks are added on the lithography mask for a precise alignment process.

2.1.6 E-beam evaporation

E-beam evaporation is used for the final step of electrode metal deposition. Figure 2-11 shows an example of the electron beam evaporation machine I have used in my Ph.D.

Figure 2-11 Electron beam evaporation system MEB400s from PLASSYS.

The microwire with the metal electrodes is obtained by a lift-off process after electrodes' deposition with the electron beam evaporation.

2.1.7 Microwire fabrication

Using the techniques described above, the thin magnetic structures were patterned into wires using UV lithography with Ar+ ion etching down to the glass substrate. Thereafter, metal contacts were obtained via lift-off technique after a second UV lithography and deposition of electrodes by e-beam evaporation. Figure 2-12 shows the full fabrication process flow of magnetic microwire that I have developed during my Ph.D. research.

Details are as follows:

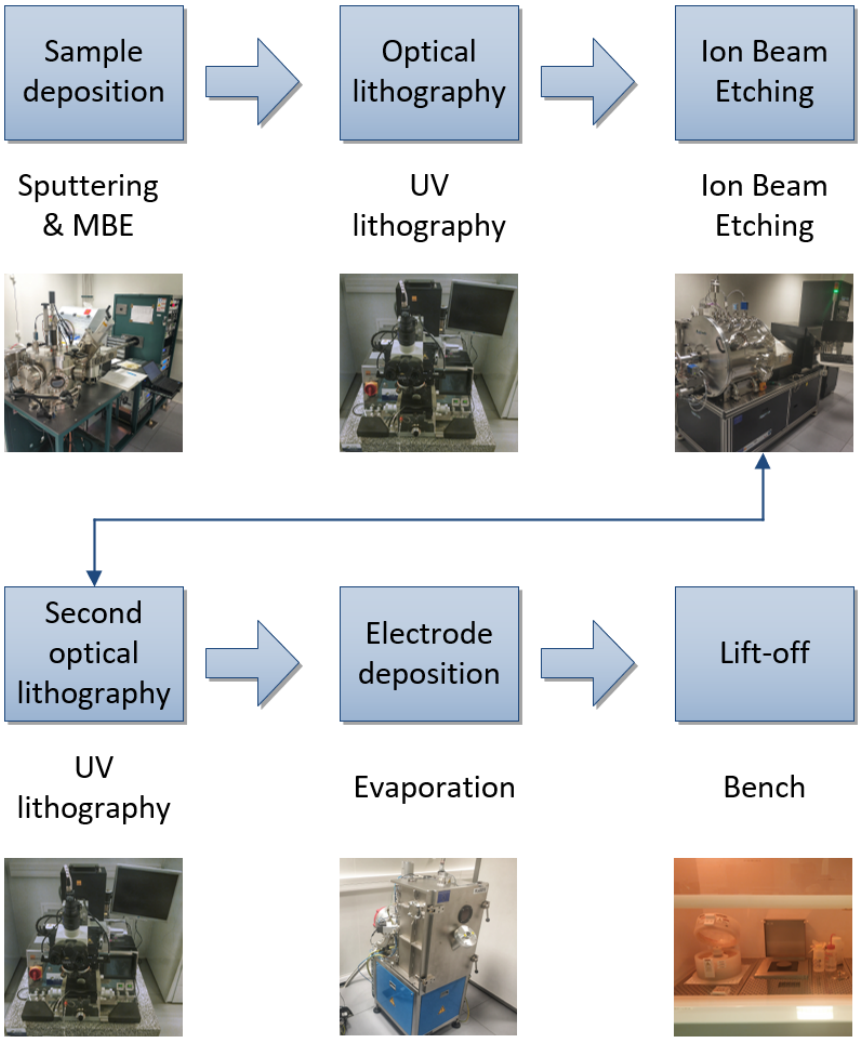

Figure 2-12 Process flow for the fabrication of magnetic microwires.

The photoresist S1813 is deposited uniformly on the samples by spin coater SPIN150 with a spinning speed of 10000 turns/min, an acceleration of 4000 turns/min/s during 40 s. Then, the samples are annealed on a hotplate during 60 s at 390 K. The layouts of the photomasks for the first and second UV lithography are shown in Figure 2-13.

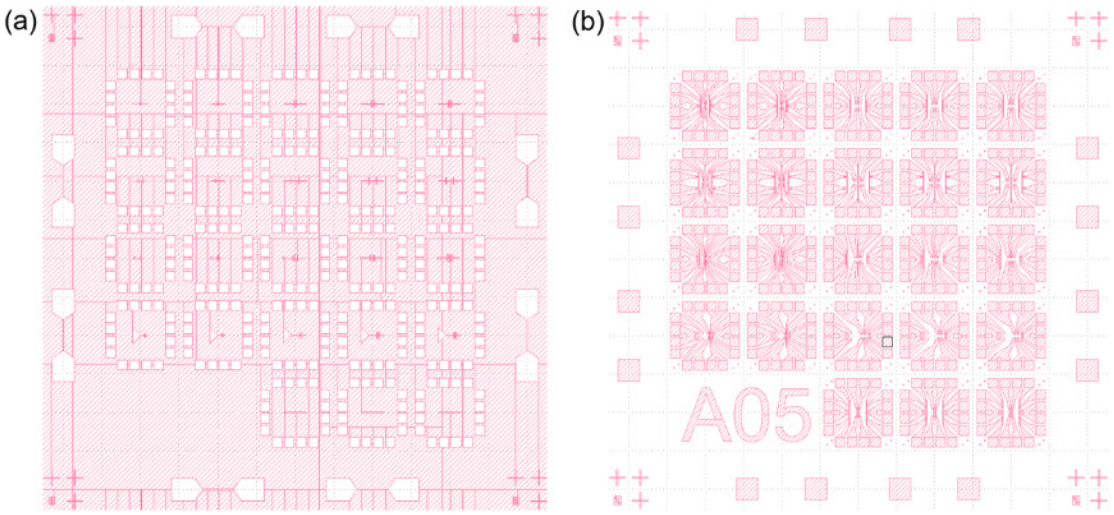

Figure 2-13 Layouts of the photomasks for the (a) first and (b) second UV lithography.

The details for the first photomask (connection pads and microwires) and second photomask (electrodes) are shown in Figure 2-14.

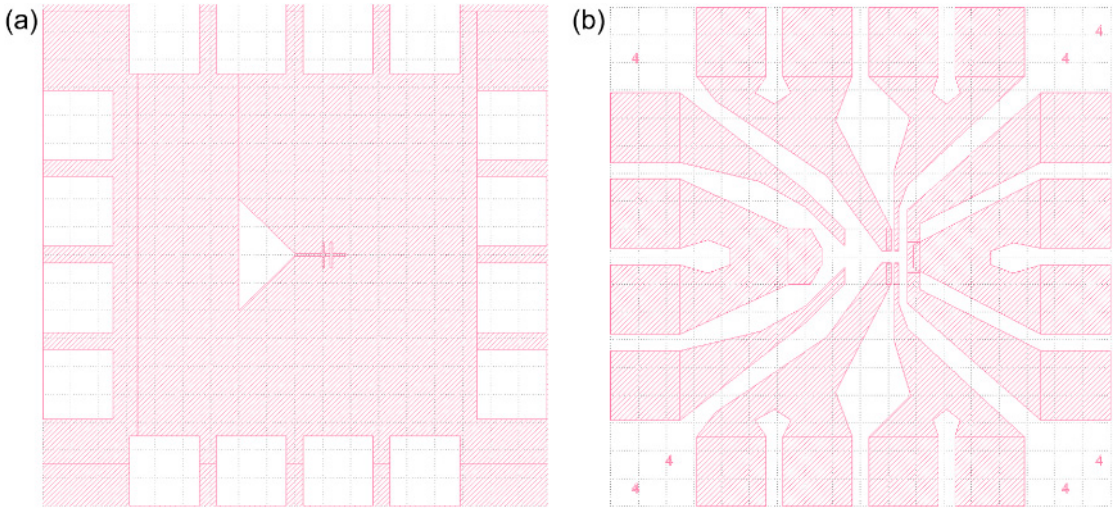

Figure 2-14 Layouts of a single microwire for the (a) first and (b) second UV lithography.

The UV insolation is conducted by the MJB4 machine from SUSS MicroTec company with a flux of 137.6 mJ/cm^2 during 20 s. The insolated samples are then developed in MF319 solvent during 40 s at room temperature and rinsed by deionized water during 20 s at room temperature. Figure 2-15 (a) shows the microscope images of the microwires after the first UV lithography, where the photoresist remains on the region of the microwires and the connection pads to protect them during the etching process. The IBE is then used to remove the thin films in the region without the photoresist. The

etching angle and ejected power are 10 degree and 71 W, respectively. Figure 2-15 (b) shows the screenshots of the SIMS measurement, which indicate the etching stop points by the end-point detection.

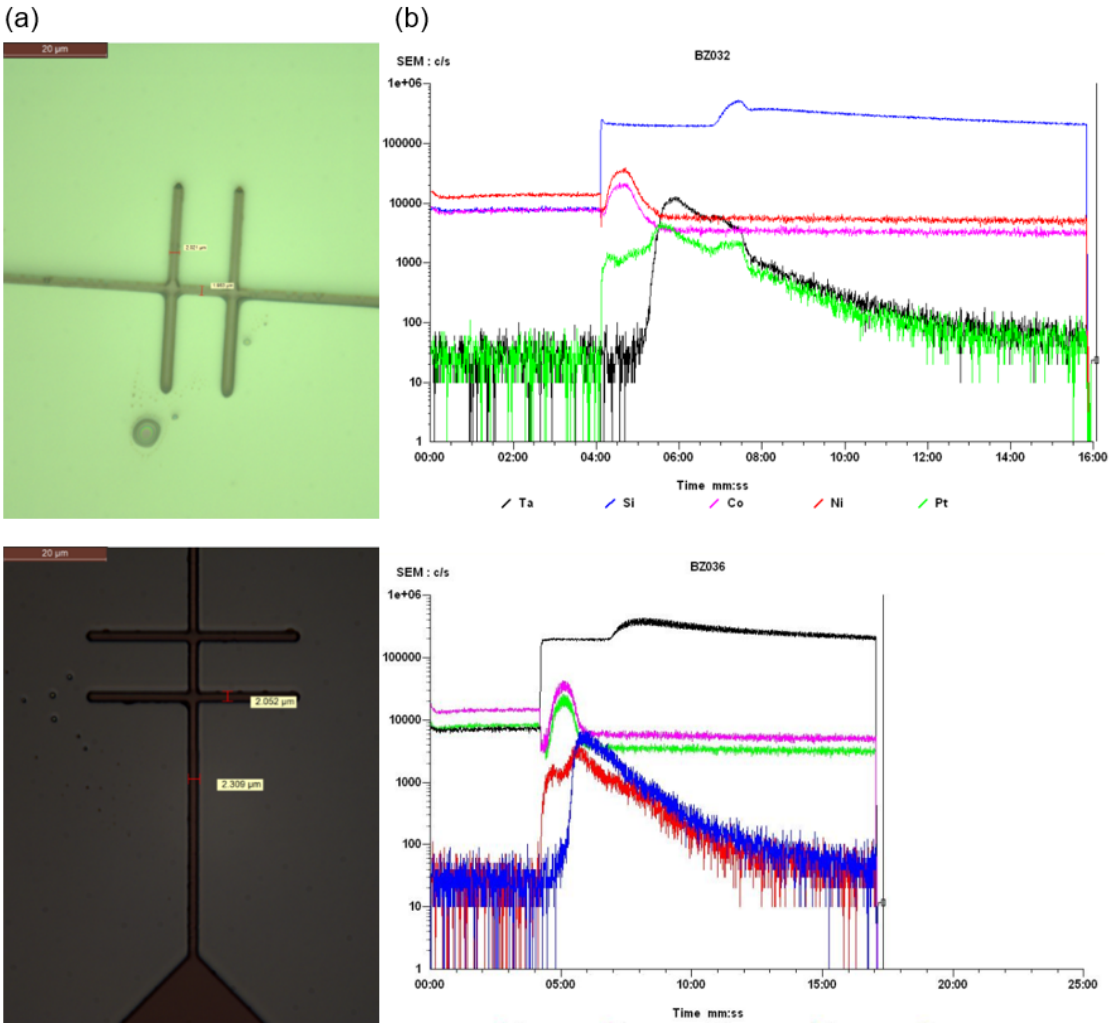

Figure 2-15 (a) Microscope images of the microwires after the first UV lithography and (b) SIMS measurement for the IBE process of the microwires for (top) Ta(3 nm)/Pt(5 nm)/Co(0.3 nm)/Ni(0.6 nm)/Co(0.3 nm)/Pt(2 nm) and (bottom) Ta(3 nm)/Pt(3 nm)/Co(0.3 nm)/Ni(0.6 nm)/Co(0.3 nm)/Pt(3 nm).

The remained photoresist is removed via a lift-off process using acetone during 12 hours at room temperature, followed by a rinse during 20 s at room temperature in deionized water (see the microscope images in Figure 2-16).

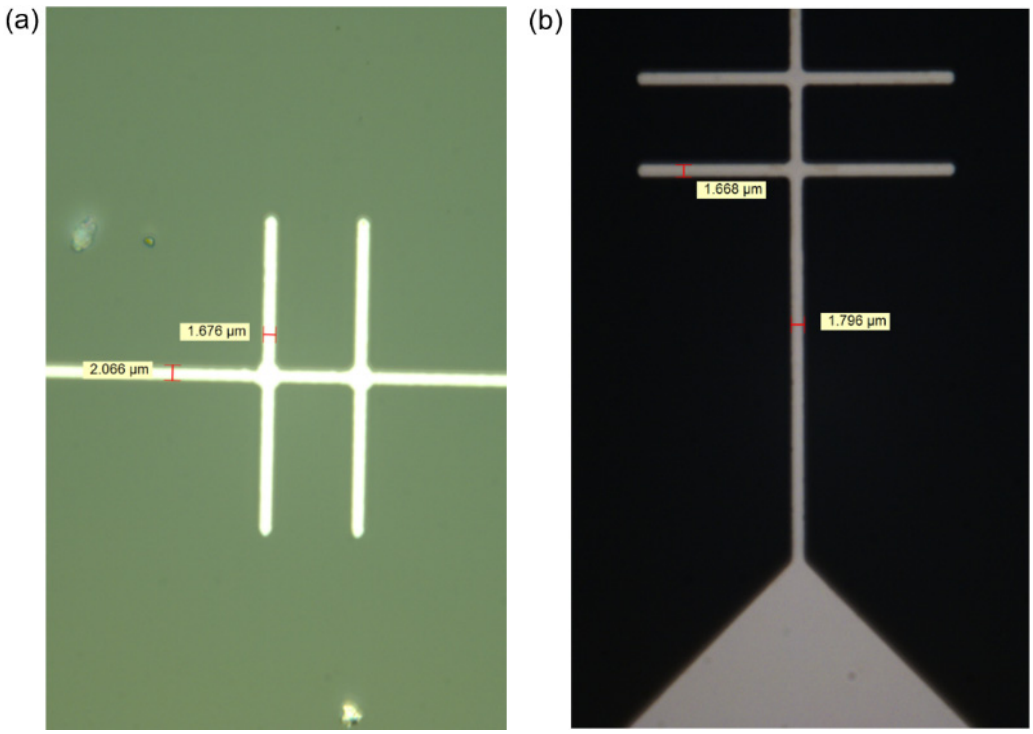

Figure 2-16 Microscope images of the microwires after the first lift-off process for (a) Ta(3 nm)/Pt(5 nm)/Co(0.3 nm)/Ni(0.6 nm)/Co(0.3 nm)/Pt(2 nm) and (b) Ta(3 nm)/Pt(3 nm)/Co(0.3 nm)/Ni(0.6 nm)/Co(0.3 nm)/Pt(3 nm).

For the second UV lithography, the photoresist LOR3A is deposited uniformly on the samples by the spin coater SPIN150 with a spinning speed of 7000 turns/min, an acceleration of 4000 turns/min/s during 40 s before the deposition of photoresist S1813. Then, the recipes for the spin coating of photoresist S1813, UV insolation, development and rinse are the same as the first UV lithography. Figure 2-17 shows the microscope images after the second UV lithography and before the following electron beam evaporation and lift-off process.

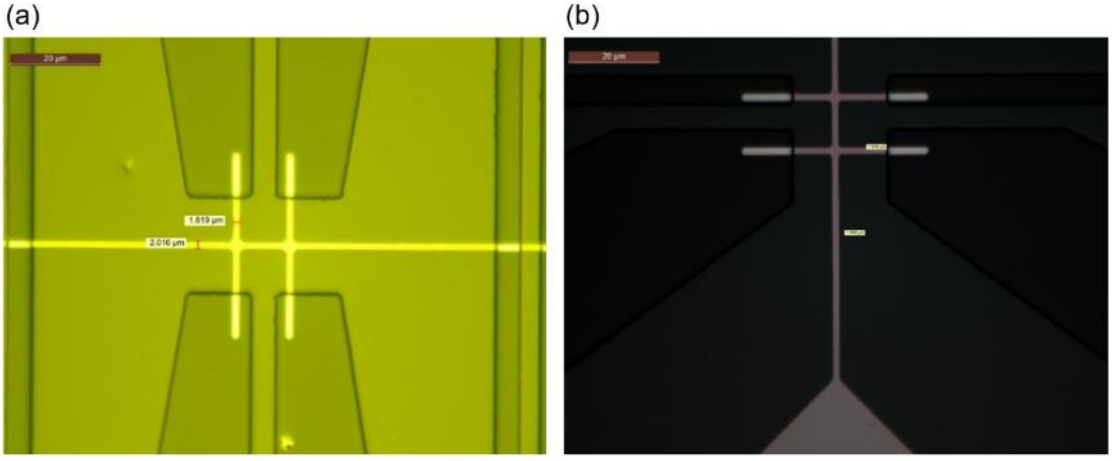

Figure 2-17 Microscope images of the microwires after the second UV lithography for (a) Ta(3 nm)/Pt(5 nm)/Co(0.3 nm)/Ni(0.6 nm)/Co(0.3 nm)/Pt(2 nm) and (b) Ta(3 nm)/Pt(3 nm)/Co(0.3 nm)/Ni(0.6 nm)/Co(0.3 nm)/Pt(3 nm).

The electrodes of Ti (10 nm)/Au (100 nm) are then deposited by electron beam evaporation and the remained photoresist is removed via a lift-off process by the remover 1165 during 1 hours at 350 K with 20 s ultrasonic cleaning every 15 min, followed by a rinse during 20 s at room temperature by deionized water, where the microscope images are shown in Figure 2-18.

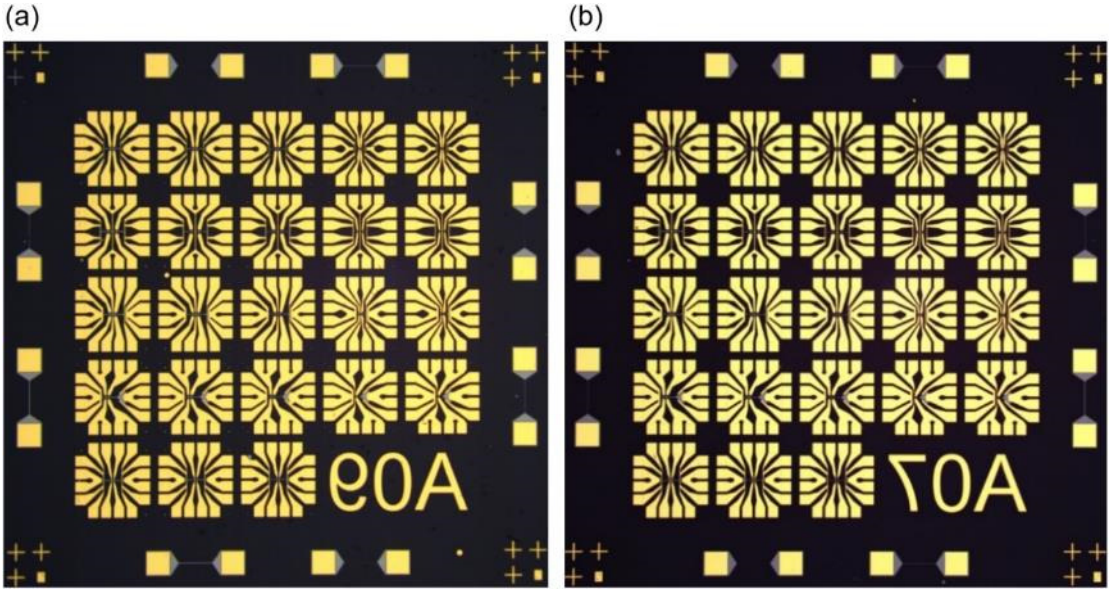

Figure 2-18 Microscope images of the microwires after the second lift-off process for (a) Ta(3 nm)/Pt(5 nm)/Co(0.3 nm)/Ni(0.6 nm)/Co(0.3 nm)/Pt(2 nm) and (b) Ta(3 nm)/Pt(3 nm)/Co(0.3 nm)/Ni(0.6 nm)/Co(0.3 nm)/Pt(3 nm).

2.2 Magneto-optical Kerr microscopy

Magneto-optical Kerr microscopy is based on the Kerr effect. The Kerr effect was discovered by John Kerr in 1877, as shown in Figure 2-19. Similar to the Faraday effect, the polarized light is reflected by the surface of the magnetic material and the polarization direction of the reflected light changes. After linear polarization of the incident light and the filtration of the emitted light by an analyzer, the intensity of the light after the analyzer can be detected by the optical sensing component, in order to obtain the magnetization of the material.

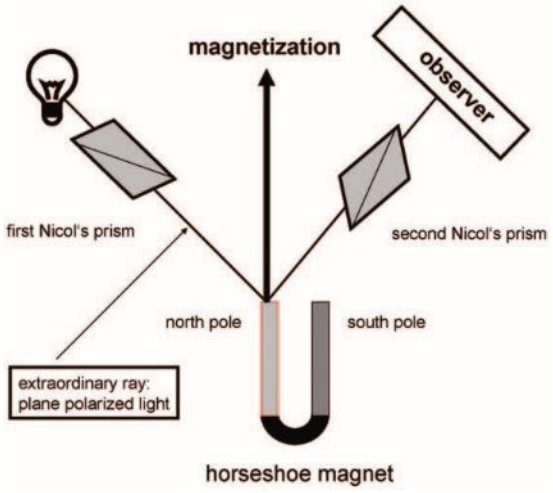

Figure 2-19 The set-up used by John Kerr to discover the magneto-optic Kerr effect [WEI08].

The Kerr effect can be measured in three configurations depending on the plane of incidence of light and the sample surface: polar, longitudinal and transverse, as shown in Figure 2-20 [OAK05]

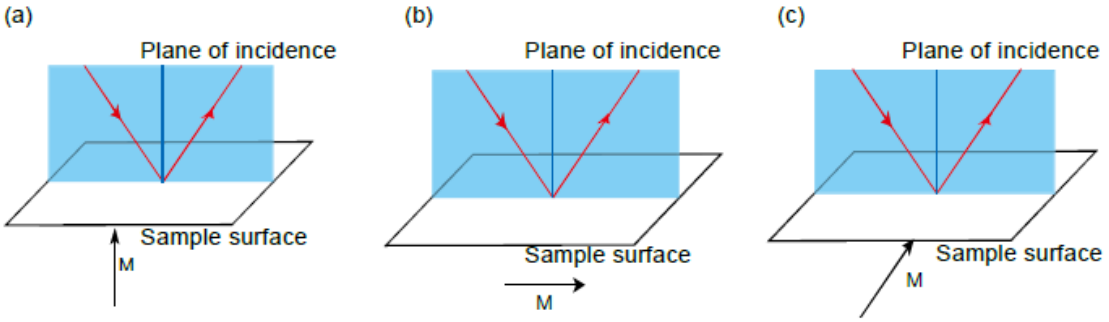

Figure 2-20 The schematic for three types of magneto-optic Kerr effect. (a) Polar Kerr effect. (b) Longitudinal Kerr effect. (c) Transverse Kerr effect [OAK05].

In my Ph.D., I have used the polar Kerr effect. Thanks to the high sensitivity of the polar Kerr effect, a Kerr microscope can detect the magnetization of thin film sample down to 1 nm with a spatial resolution down to a few 100 nm depending on the light wavelength used for the experiment

A typical configuration for a polar Kerr microscope is shown in Figure 2-21. The basic principle is as follows: the light is emitted from the light source and is focused through a converging lens. Then, a polarizer polarizes the light into linearly polarized light. Next, the polarized light is reflected by a beam splitter and enters into the objective. The light

goes through the objective and is reflected on the sample surface. After the reflected light gets out of the objective, part of the light goes through the beam splitter and the analyzer, and finally goes into the camera for imaging, where the light is captured by the charge coupled device (CCD) camera. As the polarization direction of the polarizer and the analyzer is nearly perpendicular, and the polarization direction of the light will change after the reflection through the magnetic sample, the magnetization state of the sample can be identified by the intensity of the light, as the Kerr rotation angle is related to the intensity and angle of the sample magnetization.

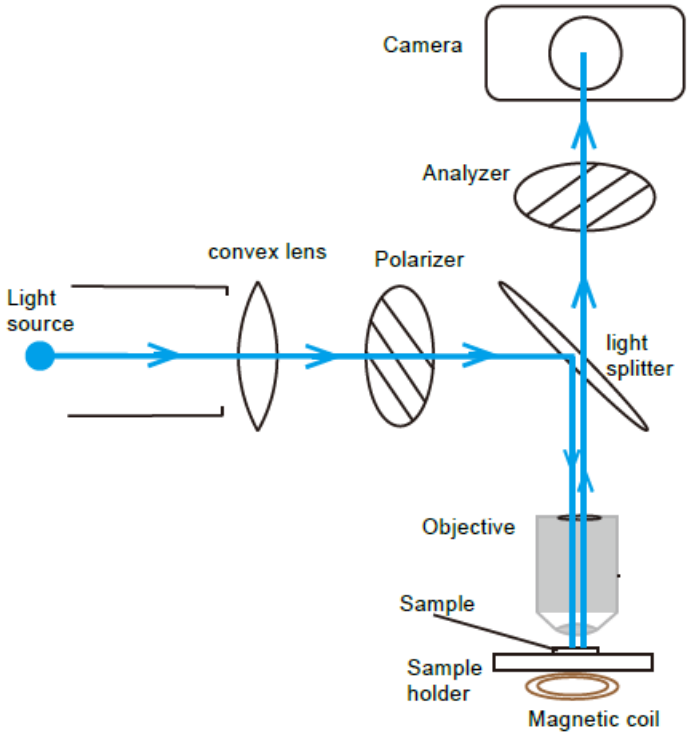

Figure 2-21 Schematic of a polar Kerr microscope [ZHA18].

Figure 2-22 shows the polar Kerr microscope used in the experiments. The light source is a blue light emitting diode (LED) with a wavelength of 450 nm. The objective with 100x magnification and 0.8x aperture allows the observation of wires with width as small as 200 nm.

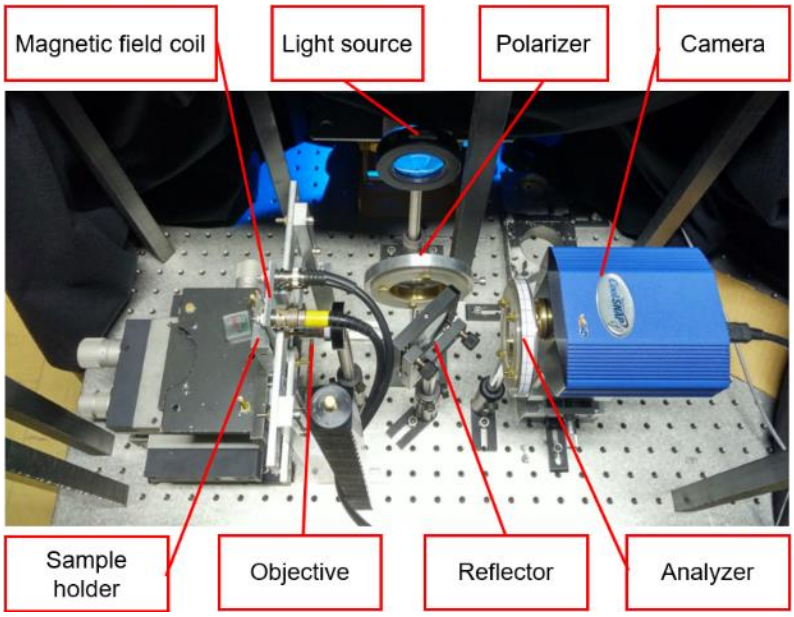

Figure 2-22 The set-up of the Kerr microscope [ZHA18].

Figure 2-23 shows the Kerr image of the fabricated microwire and its magnetic contrast of the domain wall by image difference technique, both obtained with the Kerr microscope.

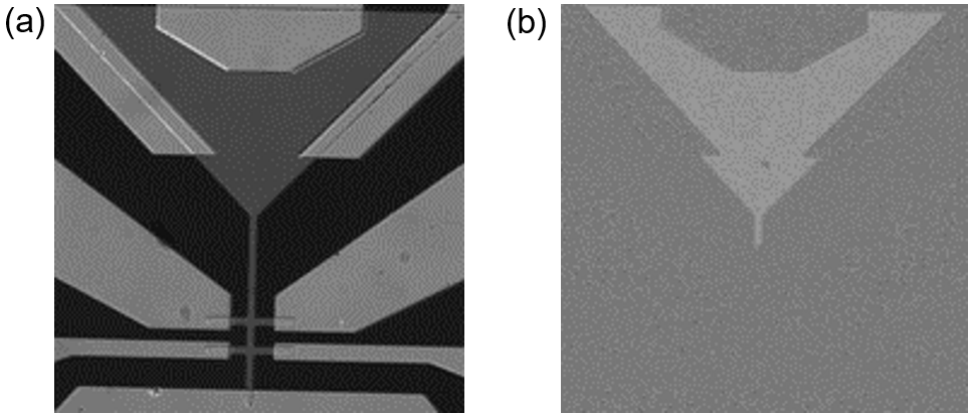

Figure 2-23 Kerr image of (a) the fabricated microwire and (b) its magnetic contrast of the domain wall by image difference technique.

2.2.1 Field configuration for field-driven domain wall motion

In order to investigate the field-driven domain wall motion, pulses of perpendicular field generated by a micro-coil is used. The magnetic coil can generate pulse field down to a few microseconds. As the rise time of the pulse field is proportional to the coil inductance L and L raises with increased coil turns, the number of coil turns should be reduced to decrease the rise time. However, less coil turns lead to smaller pulse field.

As a result, there is a trade-off for a pulse field between the small rise time and the large field amplitude. The configuration of the coil is shown in Figure 2-24. The sample is sandwiched between two plastic plates fixed by a solid holder with screws. A hole on the left plate enables the observation of the sample by the objective. The coil is mounted on a support and the coil center is along the axis of the lens. As the sample holder and the coil holder are fixed independently, the sample can be moved freely with the objective always pointing to the center of the coil.

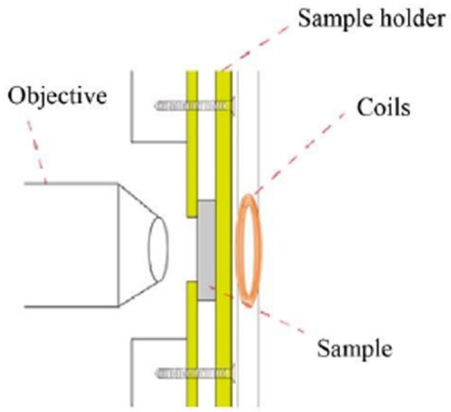

Figure 2-24 Configuration to integrate a magnetic coil close to the sample [ZHA18].

Figure 2-25 shows the power supply circuit to induce short pulses of perpendicular magnetic field. A function generator controls the gate voltage applied on a transistor, in order to turn on or off the power switch. The resistance (0.2 Ω) in the circuit is in parallel with an oscilloscope that is used to observe the waveform. Power source can be a battery or a voltage supply. The amplitude of the generated magnetic field can be calculated by the following formula:

$$H = (U_{\text{oscillo}}\ \text{mV}/1000)/0.2\ \Omega \times 10.2\ \text{mT/A} \qquad (2.1)$$

where U_{oscillo} is the voltage value measured by the oscilloscope and H is the magnetic field generated by the coil. The coil used for nucleation can reach a maximum field amplitude of 1000 Oe with a minimum pulse duration around 5 μs as the rise time is relatively large. The coil used for domain wall motion could only reach a maximum field amplitude of 300 Oe, but its rise time is much better with a minimum pulse duration around 2 μs.

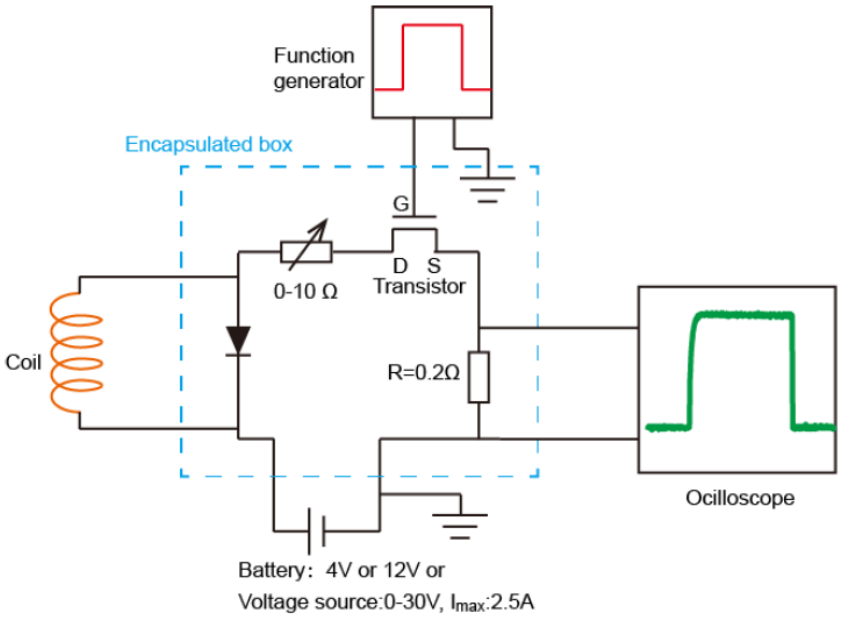

Figure 2-25 P supply circuit used to induce pulses of magnetic field in the Kerr microscope set-up [ZHA18].

The nucleation of the domain wall requires a large but short pulse field as a large amplitude ensures the domain wall nucleation while a short duration prevents the complete switching of the whole domain. First, a large and long pulse field is applied to saturate the sample in one magnetization direction. Then, a large but short pulse field is applied to the sample with the opposite direction to nucleate a domain wall. The nucleation usually takes place in the large triangle pad due to its large surface.

The measurement of domain wall velocity also requires a short pulse duration, in order to make sure that the propagation for each pulse doesn't switch the whole wire. An example of the field signal for domain wall motion is shown in Figure 2-26. The velocity is obtained by dividing the domain wall displacement distance observed in the Kerr microscope by the pulse duration of the magnetic field. More specifically, two Kerr images are taken before and after the applied pulse field with a duration of t. By subtracting the two images, the domain wall displacement D under the field pulse can be obtained and the velocity $v = D/t$ can be determined.

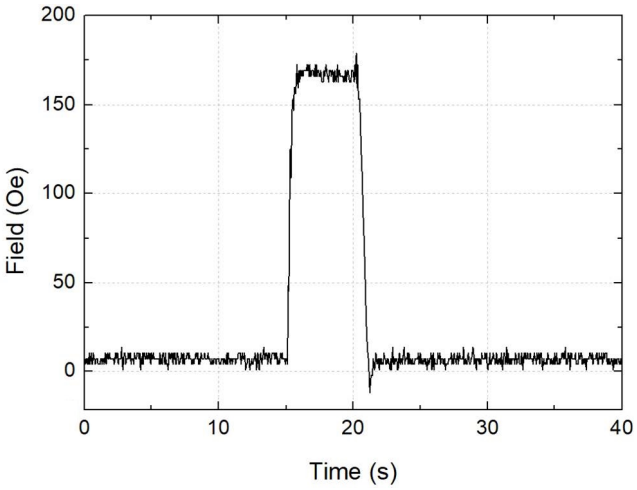

Figure 2-26 Field pulses signal with a duration of 5 μs.

2.2.2 Field configuration for DMI measurement

In order to measure the DMI value of the thin film, an in-plane field is also added, which is induced by electromagnet with a soft iron core, as shown in Figure 2-27.

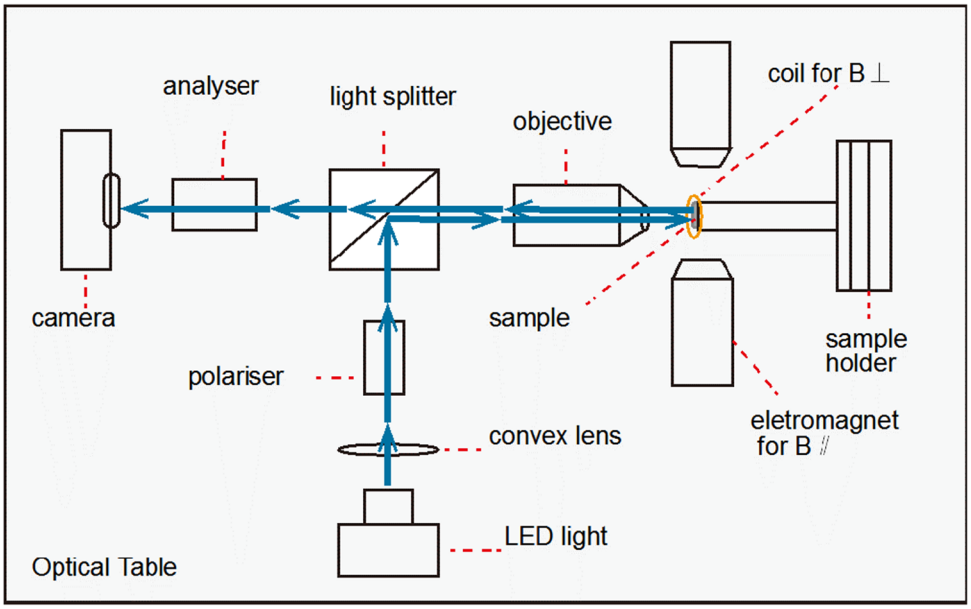

Figure 2-27 The magnet configuration and the optical path for the DMI measurement set-up.

The DMI measurement procedure is as follows: The sample is first saturated by a large perpendicular magnetic pulse field along one magnetization direction. Next, a magnetic field in the opposite direction and proper amplitude/pulse duration is applied for nucleating a reversed domain and a first Kerr image is captured. In-plane and

perpendicular field is then applied simultaneously in order to induce the expansion of the reversed domain and a second Kerr image is taken. By doing the image difference, we can observe an asymmetric expansion of domain bubbles as illustrated in Figure 1-12. The domain wall displacement along or against the in-plane field d_+ or d_-, and the domain wall velocity $v_+ = d_+/t$ and $v_- = d_-/t$ can be obtained, where t is the pulse duration of the perpendicular field. By keeping the same perpendicular field and changing the amplitude of the in-plane field with a fixed step, the domain wall velocity under different direction of the in-plane fields can be obtained and the DMI effective field can be determined, as shown as an example in Figure 2-28.

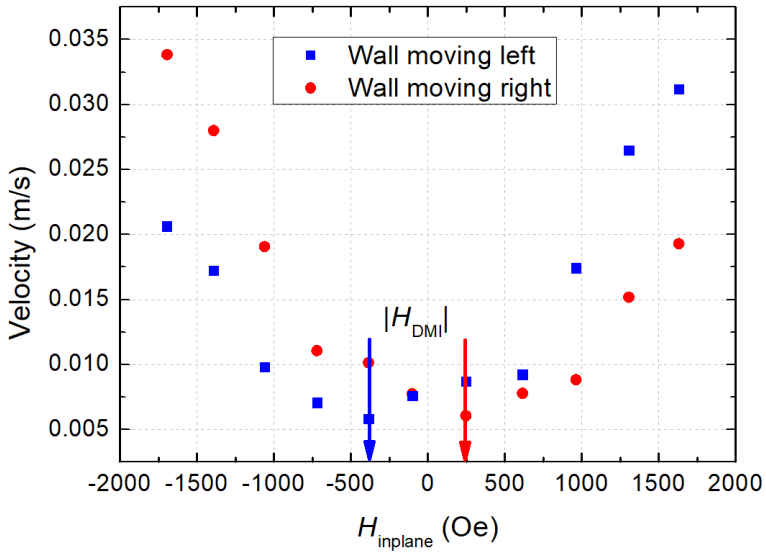

Figure 2-28 Field-induced domain wall propagation velocities in a Ta/Pt/Co/Ni/Co/Pt thin film as a function of the in-plane applied field $H_{inplane}$. $H_{inplane} > 0$ when its direction is to the left. The perpendicular field is fixed at 60 Oe with the direction out of the film and an effective DMI field H_{DMI} of +300 Oe is determined.

2.3 Femtosecond pulse laser

For the observation of all-optical switching, ultrafast laser pulses with femtosecond duration and high energy were used. The laser source consists of an oscillator and an amplifier, which produces ultrashort pulse trains and increases the pulse energy, respectively.

A Ti: sapphire femtosecond laser with a 5 kHz repetition rate, a wavelength of 800 nm

and a pulse duration of 35 fs, was used to perform the optical excitation. The Gaussian profile laser spot with a FWHM of approximately 47 μm was focused on the sample.

The set-up consists of three parts. The first part is the laser beam, which goes through four optics before illuminating the sample surface: a Glan-Taylor polarizer to linearly polarize the laser, a half-wave plate to induce a phase difference of π for power adjusting, a quarter-wave plate to obtain right-circularly (σ+) or left-circularly (σ−) light and a convex lens to focus the laser beam on the sample surface with a spot size of 50 μm. Secondly, the optical response to the laser excitation in the magnetic samples is probed by a Kerr microscope combining a LED light source and a pair of polarizer-analyzer which is crossed to obtain the maximum magneto-optical contrast. In the reflection mode of Kerr microscope, a circular polarization with 90% of helicity is obtained. Finally, the magnetic domains are imaged with a CCD camera, along with a microscope objective. An IR filter is added to block the laser beam.

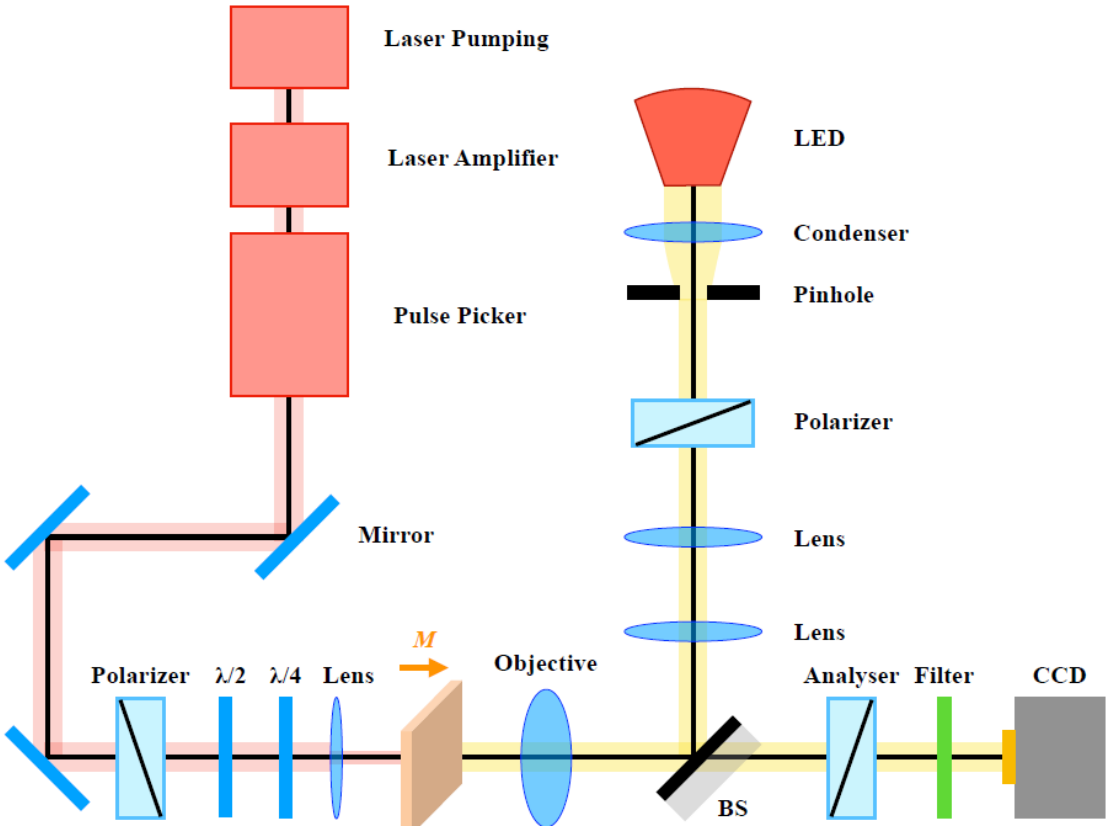

Figure 2-29 The Kerr imaging set-up for the observation of fs-laser induced magnetization

[QUE18].

2.4 Electrical characterization

In order to perform the electrical characterization, the sample holders based on printed circuit boards are made with the connection pads linking the 16 pins connector. The sample sticks on the sample holder. The electrodes of the microwire in the sample is then connected to the pads on the sample holder by wire-bonding.

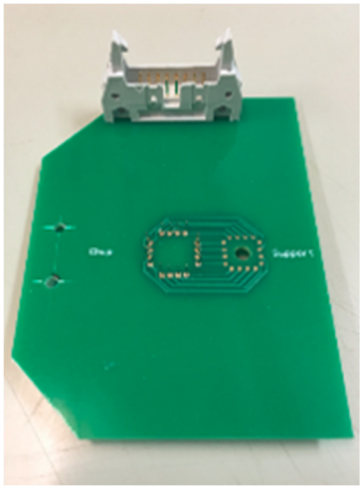

Figure 2-30 The sample holder based on printed circuit boards with the connection pads linking the 16 pins connector.

Wire bonding is a technique used in the integrated circuit packaging industry. By using the metal filament with a diameter of 15-50 μm, the microwire electrode can be connected to the sample holder pad without taking extra area. It has two bonding points, where the first one in the sample holder pad and the second one in the microwire electrode. The metal filament can go through the capillary to make the first bonding point, where the filament is attached to the sample holder pad. Next, the capillary induces the filament towards the second bonding point, where the filament is attached to the microwire electrode and is then been cut.

Figure 2-31 The wire bonding machine from WESTBOND.

In order to investigate the domain wall motion combining field and current pulses, current pulse generation function is added in the Kerr microscope set-up with pulse field configuration. The pulse generator can supply a voltage pulse up to 20V to the connected sample wire through the 16 pins connector. The voltage pulse is applied simultaneously with the magnetic field pulse.

For the experiments of domain wall motion combining laser and current pulses, microsecond current pulses are injected into the wire using a Tektronix AFG3012B Arbitrary/Function Generator, and synchronized with the laser signal.

2.5 Summary

In this section, we have presented the material deposition, microwire fabrication process, the Kerr microscope and femtosecond laser set-ups used in my Ph.D. research. In the two following chapters, I will introduce the development of specific materials and the characterization of the microwires, and the results on domain wall experiments combining current and laser.

CHAPTER 3 MATERIAL EXPLORATION FOR ALL-OPTICAL SWITCHING AND CURRENT-INDUCED DOMAIN WALL MOTION

In this chapter, I will explore the all-optical switching effect in three sets of samples that have been previously used for SOT or STT switching. Then, on 1 set of samples showing AOS, I will study current-induced domain wall motion.

3.1 Sputtered Pt/Co/heavy metal (HM) structure

3.1.1 Magnetic properties

Pt/Co/HM tri-layered structures with interfacial PMA are currently under intensive research for several emerging spintronic effects, such as SOT switching [WOO14, HUA15] and domain wall motion [MIT09, HAA13]. HM materials are used as capping layers to generate the structural asymmetry and to enhance the interfacial effects. For instance, the Pt/Co/Ta structure attracts a lot of attention as it may exhibit large DMI [MOR16], which is essential for the current-induced domain wall motion based on SOT [RYU13].

The samples Ta (2 nm)/Pt (3 nm)/Co (0.8 nm)/HM (2 nm)/Pt (3 nm) grown by magnetron sputtering as described in 2.1.1 are shown in Figure 3-1. The magnetic properties were studied by using AGM at room temperature to obtain the interfacial PMA through K_{eff}*t_{eff}, where the effective magnetic anisotropy energy K_{eff} is as follows [YAK15]:

$$K_{eff} = \frac{1}{2} H_K M_S \tag{3.1}$$

where H_K and M_S represent the anisotropy field and the saturation magnetization, respectively.

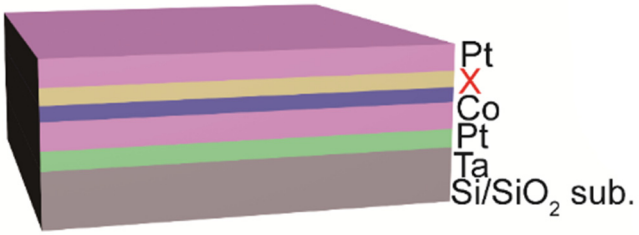

Figure 3-1 Schematic of the Ta/Pt/Co/Capping layer/Pt stack structure.

Figure 3-2 shows the hysteresis loops of Ta (2 nm)/Pt (3 nm)/Co (0.8 nm)/Capping layer (2 nm)/Pt (3 nm) stacks with magnetic fields in-plane and out-of-plane, where the capping materials are W, Ta and Pd. With a saturation field H_S smaller than 200 Oe from the out-of-plane curve, the structures Pt/Co/Ta and Pt/Co/Pd both show perpendicular anisotropy.

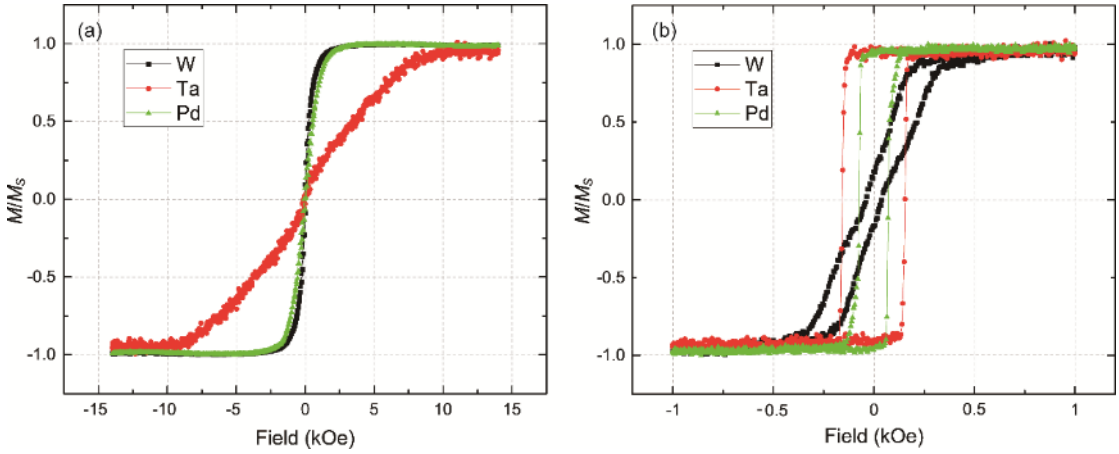

Figure 3-2 Hysteresis loops with in-plane (a) and out-of-plane (b) field for Ta (2 nm)/Pt (3 nm)/Co (0.8 nm)/Capping layer (2 nm)/Pt (3 nm) stacks with different capping HM materials: W, Ta, Pd.

The quantity K_{eff}*t_{eff}, derived from the saturation magnetization M_S*t_{eff} and the anisotropy field H_K, can be estimated by using Eq. (3.1). The structure with a Ta capping layer has a K_{eff}*t_{eff} value of 0.28 erg/cm^2, which is much larger than the value of 0.09 erg/cm^2 for Pd and 0.05 erg/cm^2 for W, indicating a strong PMA for the Pt/Co/Ta tri-layers. Except from the contribution of the same bottom Pt/Co interface, the Co/Ta interface shows a larger interfacial PMA contribution than Co/Pd and Co/W interfaces.

Table I. Measured magnetic properties of Ta (2 nm)/Pt (3 nm)/Co (0.8 nm)/Capping layer (2 nm)/Pt (3 nm) thin film structures.

Capping materials	H_c Oe	M_S*t_{eff} [a] emu/cm^2	H_K [b] Oe	K_{eff}*t_{eff} erg/cm^2
W	38	0.91×10^{-4}	1120	0.05
Ta	155	0.76×10^{-4}	7265	0.28
Pd	72	1.23×10^{-4}	1520	0.09

[a] M_S*t_{eff} is obtained by dividing the measured moment by the area of the Co magnetic layer

[b] H_K is obtained by extracting the field corresponding to 90% of the measured moment along the hard axis

3.1.2 All-optical switching results

Based on the strong PMA of the Pt/Co/HM samples deposited on Si/SiO_2 substrate, the all-optical switching is performed on the samples deposited on the glass substrates by laser pulses with a wavelength of 800 nm, a pulse duration of 35 fs and a 5 kHz repetition rate. After saturating the thin films under a large perpendicular magnetic field, the laser beam was swept over the film surface without any applied magnetic field or current. Only TD was observed in the Pt/Co/W ultra-thin film as reported in Figure 3-3 (a) for a laser power of 0.38 mW, which may be due to the size of stable magnetic domains after the laser-induced heating that is smaller than that of the laser spot at room temperature, which will be discussed in the following 3.3.4 section [ELH16].

For Pt/Co/Ta and Pt/Co/Pd ultra-thin films, there is no good contrast for the observation of the domain switching, which may be due to the capping heavy metals. Figure 3-3 (b) indicate that higher laser power burns the sample, while the magnetic domain switching induced by the lower laser power cannot be observed due to the bad contrast.

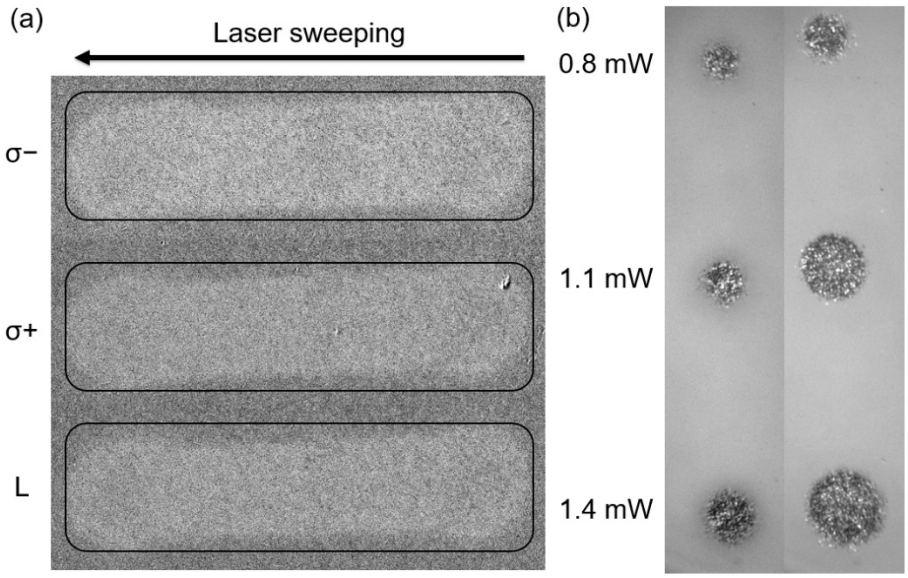

Figure 3-3 (a) Kerr images of the Ta (2 nm)/Pt (3 nm)/Co (0.8 nm)/W (2 nm)/Pt (3 nm) thin film. Linear (L), right-circularly (σ+) and left-circularly (σ-) polarized laser beams are swept over the film with a power of 0.38 mW. (b) Kerr images of the (left) Ta (2 nm)/Pt (3 nm)/Co (0.8 nm)/Pd (2 nm)/Pt (3 nm) and (right) Ta (2 nm)/Pt (3 nm)/Co (0.8 nm)/Ta (2 nm)/Pt (3 nm) thin film. Linear (L) laser beam shined on the films with a power of 0.8, 1.1, 1.4 mW.

3.2 Epitaxial Au/Co/Ni/Co/Au structure

3.2.1 Magnetic properties

[Co/Ni] multilayers have been reported to have a high spin polarization and a large spin-orbit effect, and their PMA can be easily tuned [DAA92, GIR09, RYU14, AND18]. Furthermore, [Co/Ni] multilayers are widely used for current-induced domain wall motion [BUR09, KOY11, LEG17, LEG18] and all-optical helicity-dependent switching has also been reported in [Co/Ni] [LAM14, ELH16], which makes [Co/Ni] an ideal system for studying the combined effect of spin-polarized current and femtosecond laser.

Epitaxial stacks of V (5 nm)/Au (6 ML)/Ni (x ML)/[Co (x ML)/Ni (y ML)]$_N$/Au (5 ML) grown by MBE are as described in 2.1.2. Thin film magnetic characteristics were studied by using SQUID-VSM at room temperature. Figure 3-4 shows the hysteresis loops of the stacks with the magnetic fields in-plane or out-of-plane, showing the perpendicular magnetization of the samples.

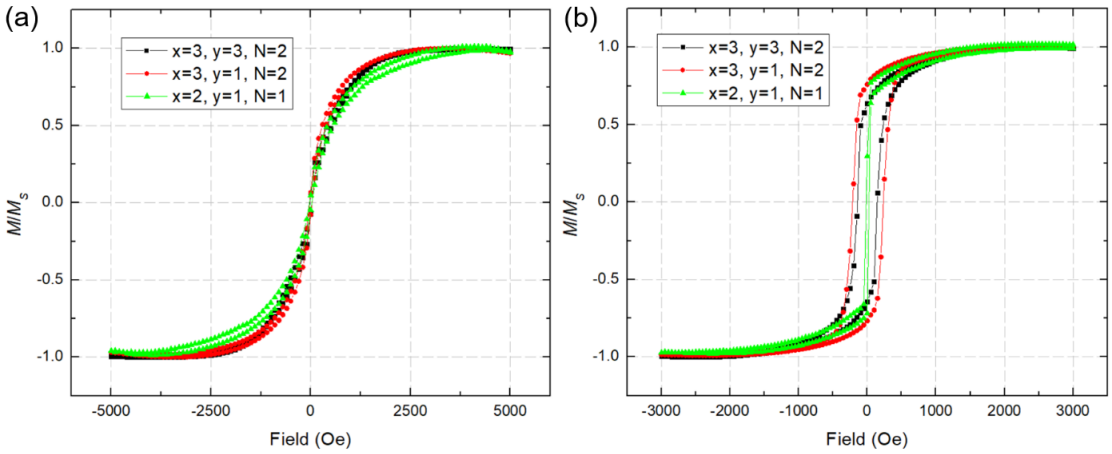

Figure 3-4 Hysteresis loops with the field in-plane (a) and out-of-plane (b) for V (5 nm)/Au (6 ML)/Ni (x ML)/[Co (x ML)/Ni (y ML)]$_N$/Au (5 ML).

The quantity K_{eff}*t_{eff}, derived from the saturation magnetization M_S*t_{eff} and the anisotropy field H_K, can be estimated by using Eq. (3.1), indicating the PMA of the epitaxial [Co/Ni] multilayers.

Table II. Measured magnetic properties of V (5 nm)/Au (6 ML)/Ni (x ML)/[Co (x ML)/Ni (y ML)]$_N$/Au (5 ML) thin film structures.

N	x	y	H_c Oe	M_S*t_{eff} [a] emu/cm^2	H_K [b] Oe	K_{eff}*t_{eff} erg/cm^2
2	3	3	140	3×10^{-4}	1550	0.233
2	1	3	170	1.2×10^{-4}	1800	0.108
1	1	2	20	0.5×10^{-4}	2000	0.05

[a] M_S*t_{eff} is obtained by dividing the measured moment by the area of the Co/Ni magnetic layer

[b] H_K is obtained by extracting the field corresponding to 90% of the measured moment along the hard axis

3.2.2 All-optical switching results

Based on the PMA of the epitaxial [Co/Ni] samples, the all-optical switching is performed on the samples by laser pulses with a wavelength of 800 nm, a pulse duration of 35 fs and a 5 kHz repetition rate. After saturating the thin films under a large perpendicular magnetic field, the laser beam was swept over the film surface without any applied magnetic field or current. Only TD is observed in the V (5 nm)/Au (6 ML)/Ni (3 ML)/[Co (3 ML)/Ni (3 ML)]$_2$/Au (5 ML) structure as reported in Figure 3-5 (a) for a laser power of 5 mW, which may be due to the size of stable magnetic domains after the laser-induced heating that is smaller than that of the laser spot at room temperature [ELH16]. As the size of magnetic domains increases gradually by lowering the total magnetic thickness, we decrease the thickness of the Co magnetic layer. However, TD still remains with the broken domains in V (5 nm)/Au (6 ML)/Ni (3 ML)/[Co (1 ML)/Ni (3 ML)]$_2$/Au (5 ML) thin film as reported in Figure 3-5 (b) for a laser power of 2 mW. Although the domain size increases, it is still smaller than the laser spot size. The calculation of the domain size will be detailed in the following 3.3.4 section. If we continue to decrease the thickness of both Co and Ni magnetic layers, the magnetic layer of V (5 nm)/Au (6 ML)/Ni (2 ML)/[Co (1 ML)/Ni (2 ML)]$_1$/Au (5 ML) stack is too thin to have a good contrast for the observation of the domain switching. Figure 3-5 (c) indicate that higher laser power burns the sample, while the magnetic

domain switching induced by the lower laser power cannot be observed due to the bad contrast.

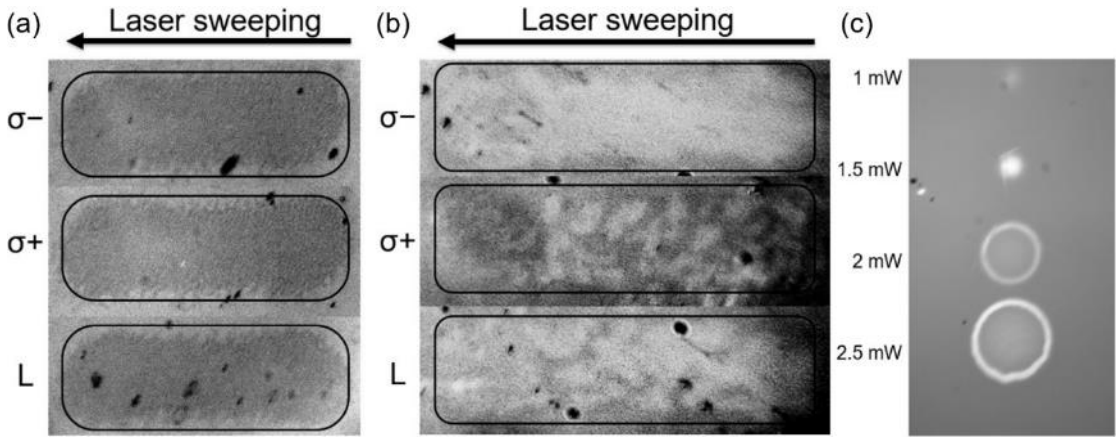

Figure 3-5 (a) Kerr images of the V (5 nm)/Au (6 ML)/Ni (3 ML)/[Co (3 ML)/Ni (3 ML)]$_2$/Au (5 ML) thin film. Linear (L), right-circularly (σ+) and left-circularly (σ-) polarized laser beams are swept over the film with a power of 5 mW. (b) Kerr images of the V (5 nm)/Au (6 ML)/Ni (3 ML)/[Co (1 ML)/Ni (3 ML)]$_2$/Au (5 ML) thin film. Linear (L), right-circularly (σ+) and left-circularly (σ-) polarized laser beams are swept over the film with a power of 2 mW. (c) Kerr images of the V (5 nm)/Au (6 ML)/Ni (2 ML)/[Co (1 ML)/Ni (2 ML)]$_1$/Au (5 ML) thin film. Linear (L) laser beam shined on the film with a power of 1, 1.5, 2, 2.5 mW.

3.3 Sputtered Pt/Co/Ni/Co/Pt structure

3.3.1 Magnetic properties

DC magnetron sputtering machine was used to grow the [Co/Ni] multilayered thin films of Ta(3 nm)/Pt(x nm)/Co(0.3 nm)/Ni(0.6 nm)/Co(0.3 nm)/Pt(y nm) as described in 2.1.1. Thin film magnetic properties were characterized by SQUID-VSM at room temperature. For Ta(3 nm)/Pt(5 nm)/Co(0.3 nm)/Ni(0.6 nm)/Co(0.3 nm)/Pt(2 nm) stack, the hysteresis loop measured with a magnetic field applied perpendicular to the plane of the layers demonstrates the perpendicular anisotropy of the thin film in Figure 3-6 (a), and we obtain a coercivity field H_c of 35 Oe and a saturation magnetization M_S of 770 emu/cm^3.

The sample of Ta(3 nm)/Pt(3 nm)/Co(0.3 nm)/Ni(0.6 nm)/Co(0.3 nm)/Pt(3 nm) also shows strong PMA [Figure 3-6 (b)], where a coercivity field H_c of 25 Oe and a saturation magnetization M_S of 770 emu/cm^3 are measured.

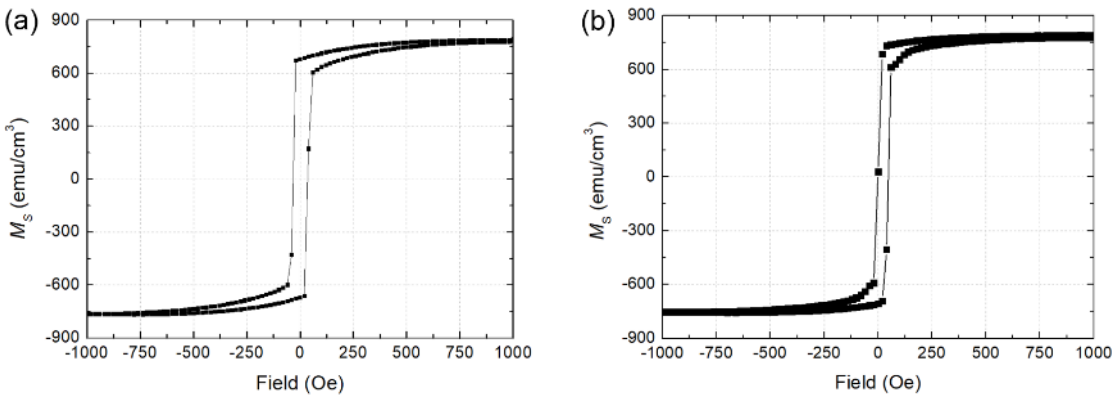

Figure 3-6 Out-of-plane hysteresis loops obtained by measuring the magnetization as a function of the field applied perpendicular to the thin films for (a) Ta(3 nm)/Pt(5 nm)/Co(0.3 nm)/Ni(0.6 nm)/Co(0.3 nm)/Pt(2 nm) and (b) Ta(3 nm)/Pt(3 nm)/Co(0.3 nm)/Ni(0.6 nm)/Co(0.3 nm)/Pt(3 nm).

3.3.2 DMI in thin films

DMI is essential for current-induced domain wall motion based on SOT [RYU13, EMO13] since it allows the formation of Néel DW wall that can be moved efficiently.

The effective DMI field H_{DMI} of the film was measured through the asymmetric expansion of domain bubbles in the creep regime using the Kerr microscope described in Chapter 2. Figure 3-7 shows the domain wall propagation velocities when a perpendicular field and an in-plane field $H_{inplane}$ are applied simultaneously. For a fixed perpendicular field of 60 Oe, the minimum domain wall velocity appears at $|H_{inplane}|$ around 300 Oe for Ta(3 nm)/Pt(5 nm)/Co(0.3 nm)/Ni(0.6 nm)/Co(0.3 nm)/Pt(2 nm) films [Figure 3-7 (a)] and around 100 Oe for Ta(3 nm)/Pt(3 nm)/Co(0.3 nm)/Ni(0.6 nm)/Co(0.3 nm)/Pt(3 nm) structures [Figure 3-7 (b)], which indicates DMI fields H_{DMI} of +300 Oe and +100 Oe, respectively. It is noted that a sizable H_{DMI} of +100 Oe is obtained in the latter symmetric sample, which may be due to the different deposition quality of the bottom Pt/Co and top Co/Pt interfaces.

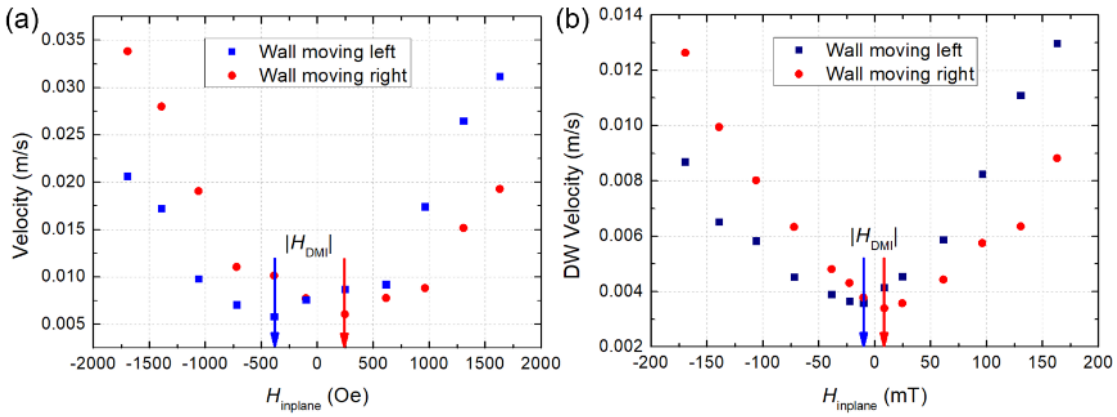

Figure 3-7 Field-induced domain wall propagation velocities in the creep regime as a function of the in-plane applied field $H_{inplane}$ for the Co/Ni/Co thin films of (a) Ta(3 nm)/Pt(5 nm)/Co(0.3 nm)/Ni(0.6 nm)/Co(0.3 nm)/Pt(2 nm) and (b) Ta(3 nm)/Pt(3 nm)/Co(0.3 nm)/Ni(0.6 nm)/Co(0.3 nm)/Pt(3 nm). The perpendicular field is fixed at 60 Oe.

3.3.3 All-optical switching results for thin films

First, the all-optical helicity-dependent switching process is demonstrated. After saturating the thin films under a large perpendicular magnetic field, the laser beam was swept over the film surface without any applied magnetic field or current. A clear AO-HDS effect is observed in the Co/Ni/Co ultra-thin film as reported in Figure 3-8 for a fluence of 9 mJ/cm^2.

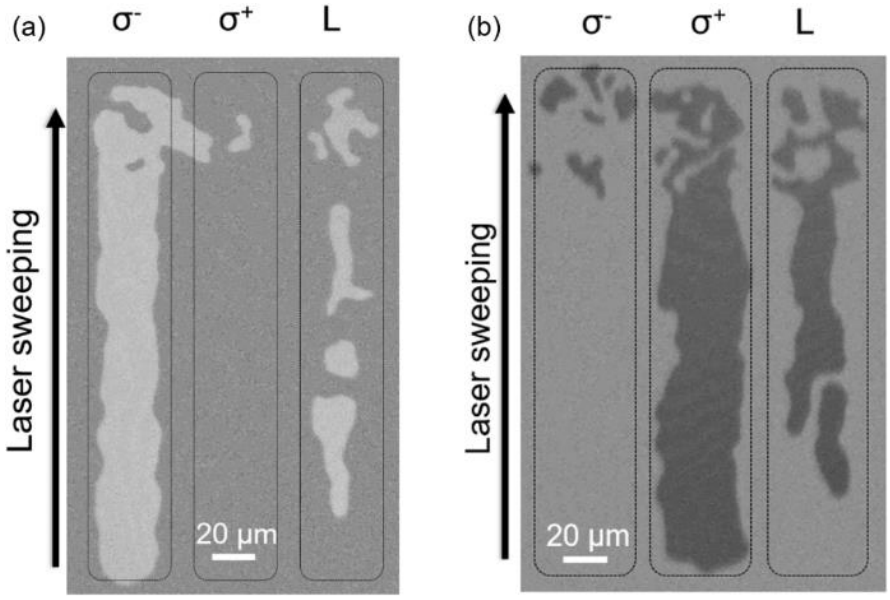

Figure 3-8 Kerr images of the Co/Ni/Co thin films of (a) Ta(3 nm)/Pt(5 nm)/Co(0.3 nm)/Ni(0.6 nm)/Co(0.3 nm)/Pt(2 nm) and (b) Ta(3 nm)/Pt(3 nm)/Co(0.3 nm)/Ni(0.6 nm)/Co(0.3 nm)/Pt(3 nm). Linear (L), right-circularly (σ+) and left-circularly (σ-) polarized laser beams are swept over the film with a fluence of 9 mJ/cm^2. The initial magnetization

saturation direction is M↑ and the white contrast corresponds to a reversal to magnetization M↓ for (a). The initial magnetization saturation direction is M↓ and the black contrast corresponds to a reversal to magnetization M↑ for (b).

3.3.4 Criterion for the observation of all-optical switching by domain size calculation

It is noted that the sputtered Co/Ni multilayered thin films show AO-HDS, while the sputtered Pt/Co/HM and epitaxial Co/Ni stacks do not show AO-HDS. The reason may be attributed to the equilibrium size of magnetic domains forming during the cooling process in the thin films, which is related to its magnetic properties, such as the magnetic thickness t, magnetization saturation M_S, anisotropy field H_K, exchange constant A_{ex}, as shown in Eq. (1.15). The different deposition methods result in different thin film qualities, which induce different magnetic parameters and domain sizes D for the three sets of samples. As a result, as shown in Table III, the sputtered Co/Ni samples 1 and 2 have domain sizes larger than the laser spot size of approximately 50 μm, while the domain sizes for epitaxial Co/Ni stacks 3, 4 and sputtered Pt/Co/HM stacks 6, 7, 8 are smaller than 50 μm. Although the epitaxial Co/Ni sample 5 has a domain size larger than the laser spot size, but AO-HDS is not observed due to the thin magnetic layer that induces a bad contrast. According to the criterion in reference [ELH16], AO-HDS is only observed in sputtered samples 1 and 2.

Table III. Measured magnetic parameters and calculated domain sizes of the three sets of samples.

Structure (thickness in nm)	t nm	M_S emu/cm^3	H_K Oe	A_{ex} erg/cm	D μm
1. Ta(3)/Pt(5)/Co(0.3)/Ni(0.6)/Co(0.3)/Pt(2)	1.2	770	6942	0.88×10^{-6}	2×10^{6}
2. Ta(3)/Pt(3)/Co(0.3)/Ni(0.6)/Co(0.3)/Pt(3)	1.2	770	6896	0.88×10^{-6}	1.8×10^{6}
3. V(5)/Au(1.2)/Ni(0.6)/$[Co(0.6)/Ni(0.6)]_2$/Au(1)	2.4	1250	1550	0.88×10^{-6}	3.8×10^{-3}
4. V(5)/Au(1.2)/Ni(0.6)/$[Co(0.2)/Ni(0.6)]_2$/Au(1)	1.6	750	1800	0.88×10^{-6}	2.9
5. V(5)/Au(1.2)/Ni(0.4)/$[Co(0.2)/Ni(0.4)]_1$/Au(1)	0.6	800	2000	0.88×10^{-6}	6.7×10^{5}
6. Ta(2)/Pt(3)/Co(0.8)/W(2)/Pt(3)	0.8	2090	1120	1.2×10^{-6}	2.4×10^{-4}
7. Ta(2)/Pt(3)/Co(0.8)/Ta(2)/Pt(3)	0.8	2034	7265	1.2×10^{-6}	3.1
8. Ta(2)/Pt(3)/Co(0.8)/Pd(2)/Pt(3)	0.8	1926	1520	1.2×10^{-6}	3.1×10^{-3}

3.3.5 Current-induced domain wall motion in Ta(3 nm)/Pt(3 nm)/Co(0.3 nm)/Ni(0.6 nm)/Co(0.3 nm)/Pt(3 nm) structure

10 μs current pulses at a 5 kHz frequency were applied across the 4 μm wire. It is confirmed that μs current pulses alone with a current density lower than 16.5×10^6 A/cm^2 cannot move the domain wall.

3.3.5.1 The SOT contribution

The second harmonic technique described in reference [KIM13] was used to quantify the SOT contribution in the sample. The inset of Figure 3-9 (a) shows the optical image of the 10 μm Hall bar as well as the experimental geometry. A sinusoidal current with a maximum value of I_{ac} oscillating at f = 133.33 Hz was injected along the x-direction, while the first harmonic voltage V_ω and the second harmonic voltage $V_{2\omega}$ were measured along the y-direction with lock-in amplifiers. The in-plane magnetic field $H_{x(y)}$ was applied along the x- or y-direction. The spin Hall angle θ_{SH}, the DL effective field ΔH_x, and the FL effective field ΔH_y can be deduced from the following equation:

$$\Delta H_{x(y)} = -2\frac{\partial V_{2\omega}}{\partial H_{x(y)}} / \frac{\partial^2 V_\omega}{\partial H_{x(y)}^2} \tag{3.2}$$

$$\theta_{SH} = -\frac{2eM_S t_f}{\hbar} \times \frac{\Delta H_x}{J_{ac}} \tag{3.3}$$

where e is the electron charge and t_f is the thickness of the ferromagnetic layer. By parabolic fitting of the first harmonic signal and linear fitting of the second harmonic signal, $\partial V_{2\omega}/\partial H_{x(y)}$ and $\partial^2 V_\omega/\partial H^2_{x(y)}$ can be obtained, and $\Delta H_{x(y)}$ can be deduced from Eq. (3.2). In Figure 3-9 (a), the θ_{SH} was calculated from the DL effective fields ΔH_x with Eq. (3.3) and was plotted as a function of J_{ac}, considering $J_{ac} = I_{ac}/(t\times w)$ with sample thickness t = 10.2 nm, width w = 10 μm and the sinusoidal current with a maximum value of I_{ac}. Although the thicknesses are the same for the top and bottom Pt layers, we still have an average θ_{SH} of 0.04, which may be due to the different deposition qualities of the bottom Pt/Co and top Co/Pt interfaces. Figure 3-9 (b) shows the effective field $\Delta H_{x(y)}$ as a function of different J_{ac}, where the effective DL torque

efficiency $\Delta H_x/J_{ac}$ = 1.3 Oe/(10^6 A/cm^2) and the effective FL torque efficiency $\Delta H_y/J_{ac}$ = 0.13 Oe/(10^6 A/cm^2) were extracted by linear fitting of the curve. The FL torque induces a negligible Rashba effect, which is consistent with the results for Pt/Co/Pt structure [HAA13].

As the effective DMI field of +100 Oe is not sufficient to favor a left-handed chiral Néel domain walls [TET15], the SOT with a θ_{SH} of 0.04 and $\Delta H_x/J_{ac}$ of 1.3 Oe/(10^6 A/cm^2) cannot induce domain wall motion with only current pulses, but it may favor the domain wall motion against the electron flow [EMO13]. However, the following domain wall motion experiment combining current and field shows that the domain wall propagates in the direction of the electron flow. Therefore, the SOT contribution for the domain wall motion is negligible and the propagation in the direction of electron flow is due to the STT contribution.

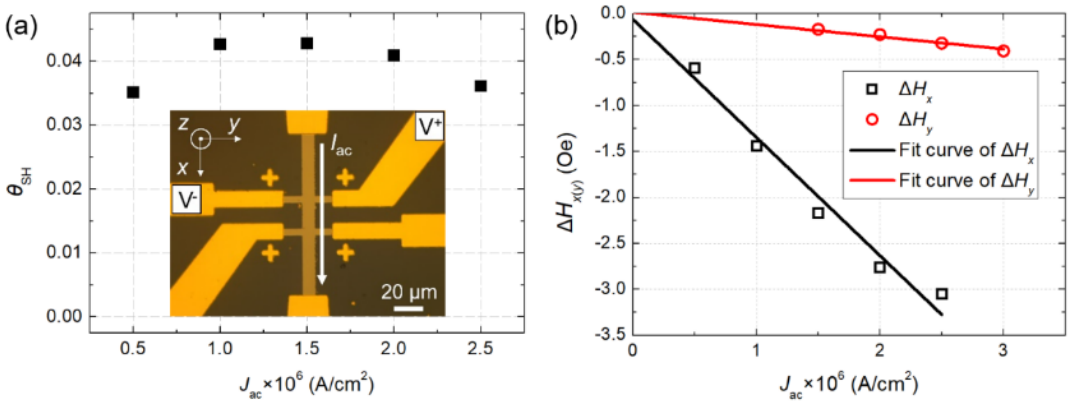

Figure 3-9 Measurements on Ta(3 nm)/Pt(3 nm)/Co(0.3 nm)/Ni(0.6 nm)/Co(0.3 nm)/Pt(3 nm) Hall bar. (a) The spin Hall angle θ_{SH} as a function of J_{ac} using the second harmonic technique. The inset shows the microscope image of the 10 μm Hall bar and the schematic illustration of the second harmonic experimental geometry. (b) The DL effective field ΔH_x and FL effective field ΔH_y deduced from the above measurements as a function of J_{ac}. The open symbols were extracted by fitting the first and second harmonic signals, and the solid curves correspond to linear fittings. The torque efficiency is given by the slope of the linear fitting $\Delta H_{x(y)}/J_{ac}$.

3.3.5.2 The STT contribution

To quantify the STT contribution, we performed the experiment with μs field pulses applied perpendicular to the sample. Field and current pulses were synchronized with both 2 μs pulse duration and 0.5 μs delay. After the nucleation of a single domain wall

in the wire, 7.3×10^6 A/cm^2 or 14.6×10^6 A/cm^2 current pulses were injected synchronously with different field pulses. The domain wall displacement after each synchronized pulse was measured by the image difference technique. The domain wall velocity is calculated by dividing the domain wall displacement by 2 μs (the pulse duration). Figure 3-10 (a) displays the domain wall velocity plotted as a function of the magnetic field H_{pulse}. The black curve with square symbol shows the field-driven domain wall motion without current pulses. Both positive and negative currents increase the domain wall velocity, while the increase is more significant for negative currents.

In order to estimate the contribution from STT, ΔH is introduced as the average field shift compared to the curve without current pulses [LEG17]. Figure 3-10 (b) shows ΔH as a function of current density J and the fitted curve using $\Delta H = +\varepsilon J+\eta J^2$, where ε = -0.6 Oe/(10^6 A/cm^2) and η = 0.29 Oe/(10^6 A/cm^2)^2. Both adiabatic and nonadiabatic components may play a significant role in the domain wall motion in the investigated wire. The nonadiabatic term proportional to the current density (εJ) acts as an effective field of STT H_{STT} [BOU08]. The quadratic adiabatic term (ηJ^2) may be related to Joule heating, where it contributes to an increase of temperature by $T+\delta J^2$ with a constant δ. The temperature rise due to Joule heating of current pulses can be estimated by the following equation [CUR10]:

$$\Delta T = \frac{RI^2 \times \{\ln[16K / dCw^2)] + \ln(\tau_{pulse})\}}{2\pi lK} \tag{3.4}$$

where the specific heat C = 750 J kg^{-1} K^{-1}, thermal conduction K = 1.4 W m^{-1} K^{-1}, density d = 2500 kg/m^3 for the glass substrate, R = 1350 Ω, ω = 4 μm, l = 94 μm for the wire, and the pulse duration τ_{pulse} = 2 μs. With the current density between 7.3×10^6 A/cm^2 and 14.6×10^6 A/cm^2, the temperature rise from an injected current pulse is around 5.75 K-23 K.

Therefore, the temperature rise due to Joule heating may contribute to the increase of domain wall velocity as Joule heating helps the domain wall to overcome the pinning energy barrier [BOU11], while the velocity increases more in the negative current case

as the negative current gives a positive H_{STT}.

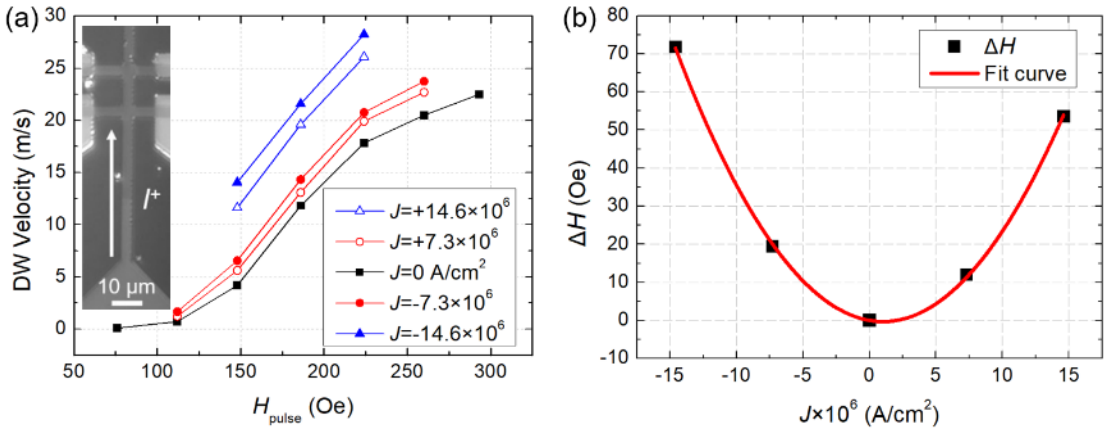

Figure 3-10 Measurements on Ta(3 nm)/Pt(3 nm)/Co(0.3 nm)/Ni(0.6 nm)/Co(0.3 nm)/Pt(3 nm). (a) domain wall velocity as a function of the magnetic field H_{pulse} for different current pulses. Current pulses of 7.3×10^6 A/cm^2 or 14.6×10^6 A/cm^2 were injected synchronously with the magnetic field pulses, where the pulse duration is both 2 µs with 0.5 µs delay. (b) ΔH as a function of current density J, where ΔH is the average field shift compared to the curve without current pulses. ΔH is positive if the shift is to the left. The black symbols were extracted from the experimental data and the red curve was fitted by $\Delta H = +\varepsilon J+\eta J^2$.

3.3.6 Current-induced domain wall motion in Ta(3 nm)/Pt(5 nm)/Co(0.3 nm)/Ni(0.6 nm)/Co(0.3 nm)/Pt(2 nm) structure

The presence of the Pt layer can induce SHE, which converts the charge currents into pure spin currents perpendicular to the electrical current [HOF13]. In order to obtain the domain wall motion induced by SOT, according to reference [RYU13], we adjust the thickness of top Pt and bottom Pt layers. Therefore, both Pt layers act as a spin current source with opposite spin direction. Since the spin Hall current depends on the layer thickness [LIU11], a net spin Hall current is expected to occur in our sample with a direction of the effective field H_{SHE} that is along $\boldsymbol{m}\times(\boldsymbol{z}\times\boldsymbol{j_e})$ [EMO13], where $\boldsymbol{m}$, $\boldsymbol{z}$ and $\boldsymbol{j_e}$ are unit vectors along the magnetization, z axis and electron flow, respectively.

8 µs current pulses with a current density of 16.5×10^6 A/cm^2 at a 5 kHz frequency were applied during 10 seconds without any magnetic field or laser beam after the nucleation of a reversed domain in the wire. This results in domain wall propagation against the electron flow, as shown in Figure 3-11 (a). With an effective DMI field

H_{DMI} of +300 Oe that favors a left-handed chiral Néel domain walls [JE13, TET15], H_{SHE} enables the domain wall propagation against the electron flow, which is consistent in our case with current-induced domain wall motion driven by SOT. After the nucleation of a reversed domain in the wire, a current density lower than 15×10^6 A/cm^2 with a 5 kHz frequency and a 10 µs pulse duration cannot move the domain wall, which defines the current density threshold value.

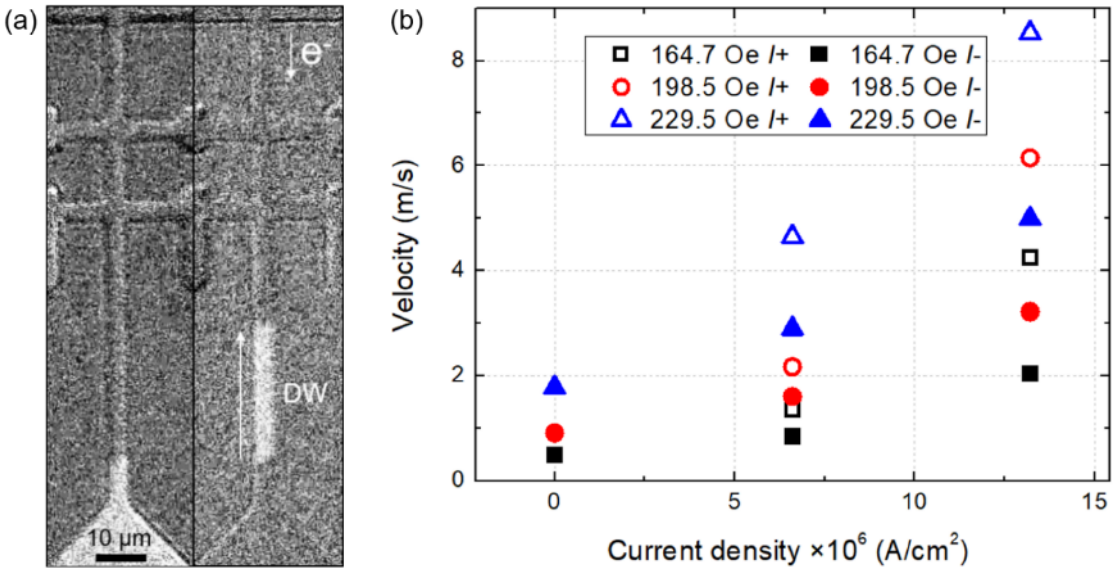

Figure 3-11 (a) Kerr images of 4 µm Co/Ni/Co ferromagnetic wires. 8 µs current pulses with a density of 16.5×10^6 A/cm^2 at a 5 kHz frequency were injected during 10 seconds after a nucleation of a reversed domain in the wire. The initial magnetization saturation direction is M↑ and the white contrast corresponds to a reversal to magnetization M↓. (b) Domain wall velocity as a function of the current amplitude with different field amplitudes and current polarities. Current pulses of 6.6×10^6 A/cm^2 or 13.2×10^6 A/cm^2 were injected synchronously with 5 µs field pulses of 164.7 Oe, 198.5 Oe or 229.5 Oe.

The contribution of Joule heating and SOT on the domain wall motion is demonstrated by performing field-driven current-assisted domain wall velocity measurements, indicating that the Joule heating increases the domain wall velocity by helping the domain wall to overcome the pinning energy barrier [BOU11], while SOT assists the domain wall motion against the direction of electron flow.

Details are as follows: a magnetic coil was introduced to apply microsecond magnetic field pulses homogeneously over the sample. A Kerr microscope was used to quantify the domain wall displacement. Field and current pulses were synchronized with both 5

μs width and no delay between them.

The domain wall nucleation took place in the triangle pad with a large pulse field. Then a sequence of synchronized pulses was injected in the wire. Domain wall velocity after each sequence was measured by the image difference, which is plotted in Figure 3-11 (b). 5 μs current pulses of 6.6×10^6 A/cm^2 or 13.2×10^6 A/cm^2 were injected synchronously with the field pulses of 164.7 Oe, 198.5 Oe or 229.5 Oe. The current polarity was varied, while the field direction was fixed. Compared to the displacement with only pulse field, the pulse current contributes in two ways: first of all, it helps the domain wall to overcome the pinning energy barrier due to Joule heating, which promotes the propagation of domain wall along the direction of pulse field [BOU11]. Secondly, the domain wall propagates more if the electrons of the current go against the domain wall propagation direction, which shows that it promotes the propagation against the direction of the electron flow due to SOT.

3.3.7 All-optical switching results for microwires

After saturation under a large perpendicular magnetic field, the laser beam with a fluence of 9 mJ/cm^2 was swept along the wires under no magnetic field nor current. Figure 3-12 indicates that the AO-HDS process is still observed in the 4 μm Co/Ni/Co ferromagnetic wire after the patterning. The study of the fluence dependence shows that the minimal fluence for observing the AO-HDS in such condition is 4.5 mJ/cm^2, which corresponds to the threshold fluence.

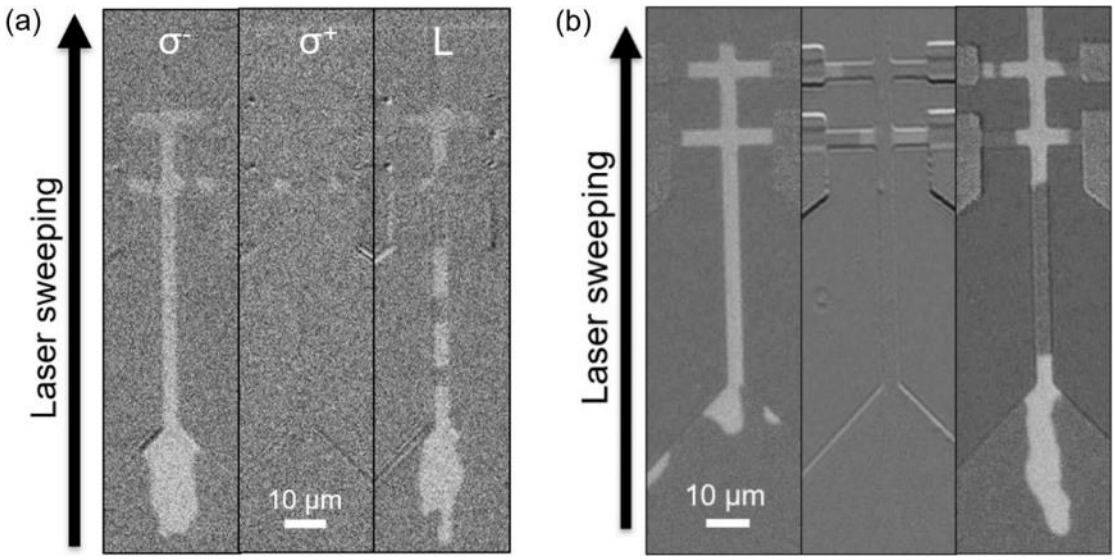

Figure 3-12 Kerr images of 4 μm Co/Ni/Co ferromagnetic wires of (a) Ta(3 nm)/Pt(5 nm)/Co(0.3 nm)/Ni(0.6 nm)/Co(0.3 nm)/Pt(2 nm) and (b) Ta(3 nm)/Pt(3 nm)/Co(0.3 nm)/Ni(0.6 nm)/Co(0.3 nm)/Pt(3 nm). Linear (L), right-circularly (σ+) and left-circularly (σ-) polarized laser beams were swept over the wire with a fluence of 9 mJ/cm^2. The initial magnetization saturation direction is M↑ and the white contrast corresponds to a reversal to magnetization M↓.

3.4 Summary

In this section, we have presented the magnetic properties, all-optical switching results for three sets of samples, including sputtered Pt/Co/heavy metal structure, epitaxial Au/Co/Ni/Co/Au structure and sputtered Pt/Co/Ni/Co/Pt structure. Only sputtered Pt/Co/Ni/Co/Pt structures show all-optical helicity-dependent switching, which is explained by the all-optical switching criterion. We have then conducted current-induced domain wall motion experiments in sputtered Pt/Co/Ni/Co/Pt samples. The SOT contribution of Ta(3 nm)/Pt(3 nm)/Co(0.3 nm)/Ni(0.6 nm)/Co(0.3 nm)/Pt(3 nm) sample is relatively small and its STT contribution dominates, while by adjusting the thickness of top Pt and bottom Pt layers, Ta(3 nm)/Pt(3 nm)/Co(0.3 nm)/Ni(0.6 nm)/Co(0.3 nm)/Pt(3 nm) sample is SOT-dominated, which can be used for the following investigation of the combined effect of SOT or STT and helicity-dependent optical effect.

CHAPTER 4 DOMAIN WALL MOTION COMBINING FEMTOSECOND LASER AND MICROSECOND CURRENT PULSES

In this chapter, we will explore the combined effect of SOT or STT and helicity-dependent optical effect. We will also investigate the different contributions of current and laser to manipulate the domain wall and a domain wall logic structure based on this effect will be proposed for future applications.

4.1 Combined effect of helicity-dependent optical effect and SOT in Ta(3 nm)/Pt(5 nm)/Co(0.3 nm)/Ni(0.6 nm)/Co(0.3 nm)/Pt(2 nm) structure

4.1.1 Experimental set-up

To investigate the interplay between SOT and helicity-dependent optical effect on the domain wall motion, microsecond current pulses and laser pulses with a pulse duration of 35 fs were synchronized at a 5 kHz repetition rate (Figure 4-1). A Kerr microscope was used to image the magnetic configuration of the investigated samples. The magnetic contrast was enhanced by subtracting two pictures taken before and after the domain wall nucleation, current injection or laser excitation, where the initial magnetization saturation direction is up (M↑) and the white contrast corresponds to a reversal to down magnetization (M↓).

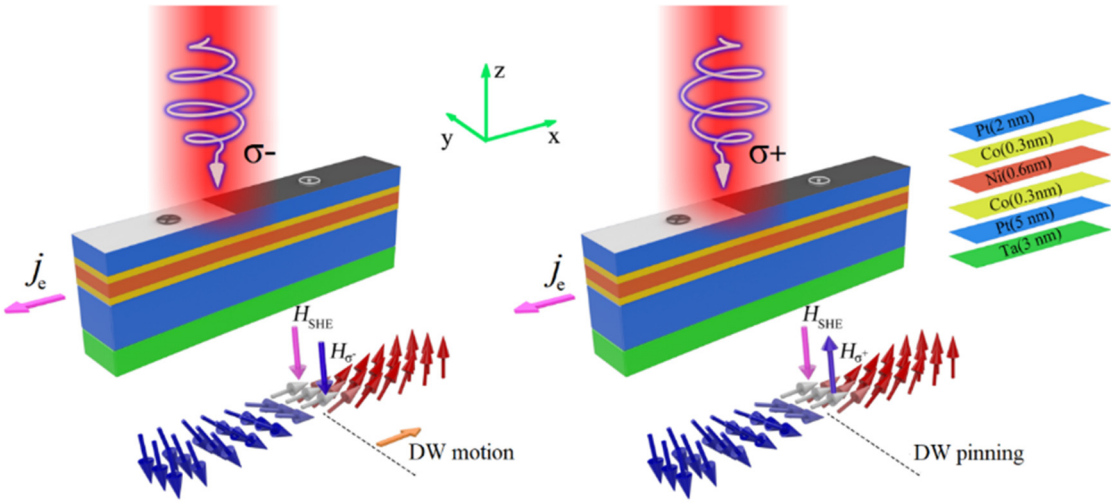

Figure 4-1 Schematic of the experimental set-up: A current pulse is injected along the 4 μm Co/Ni/Co ferromagnetic wire, while a synchronized femtosecond laser beam shines on the wire. Grayscale topside displays Kerr images from a left-handed chiral Néel domain wall nucleated in the wire. The effective field H_{SHE} moves domain walls in the direction against electron flow j_e, while the right-circularly (σ+) or left-circularly (σ-) polarized laser beam favors M↑ or M↓.

4.1.2 Domain wall motion combining synchronized femtosecond laser pulses and short current pulses

In the following, we will show the combined effect of synchronized femtosecond laser pulses and short current pulses on domain wall motion in Co/Ni/Co ultra-thin film wires with perpendicular anisotropy.

Based on the presence of all-optical helicity-dependent switching and current-induced domain wall motion in 4 μm Co/Ni/Co ferromagnetic wires, the experiments combining helicity-dependent optical effect and SOT were performed with current densities and laser fluences below the threshold values defined in the previous chapter, and a single domain wall was priorly nucleated in the wire after a magnetization saturation with M↑.

Figure 4-2 (a) shows domain wall motion after 10 seconds of laser pulses with 4 mJ/cm^2 fluence and 5 kHz repetition rate together with synchronized current pulses of 7.3×10^6 A/cm^2 and 10 μs pulse duration. The center of the laser spot is placed 8 μm away from the domain wall, as indicated by the star in Figure 4-2 (a). The left-circularly (σ-) polarized laser beam induces a larger domain wall displacement since the domain wall moves further than the position of the beam, while linear (L) polarized laser beam

induces a moderate domain wall propagation up to the beam center, whereas the right-circularly (σ+) polarized laser beam doesn't lead to any domain wall motion. The beam center corresponds to the hottest region [inset of Figure 4-2 (a)], which induces the domain wall propagation up to this point with linear (L) due to Gaussian laser heating. The measurements obtained for the two helicities demonstrate that domain wall can remain pinned when the laser beam shines with one circular helicity while it is depinned when using the opposite circular helicity. This clearly demonstrates that the laser polarization offers a new degree of freedom to control domain wall motion. It also shows that the domain wall moves against the direction of the electron flow, which confirms the effect of SOT. The dashed lines in Figure 4-2 correspond to the initial domain wall position. With the reversed current, the domain wall moves in the opposite direction as a propagation towards M↓ domains, which is also against the direction of electron flow, and the role of left-circularly (σ-) and right-circularly (σ+) polarized laser reverses as σ+ favors a propagation towards M↓ domains [Figure 4-2 (c)]. With the inputs of synchronized laser and current pulses below threshold, a large domain wall displacement can only be realized with both left-circularly (σ-) polarized laser beam and current injection, which can be exploited for magnetic domain wall logic.

The domain wall motion was further studied by increasing the current density up to 14.6×10^6 A/cm^2, which is still below the threshold value for domain wall motion. The center of the laser spot was placed 20 μm away from the domain wall, as indicated by the star in the inset of Figure 4-2 (b). Because of the Gaussian distribution of the laser intensity, the domain wall can propagate over a large distance as shown in the inset of Figure 4-2 (b), as a linear (L) laser beam shines on the sample, where the dashed lines correspond to the initial domain wall position. The video of the domain wall motion was recorded and the time evolution of the domain wall velocity was obtained by detecting the distance travelled by the domain wall along the wire using the APREX TRACK software. By the integration of the domain wall velocity in regard to the time evolution, the displacement as a function of the laser polarization is shown in Figure 4-2 (b). Three regimes can be distinguished: domain wall propagates slowly at first

and moves rapidly as it gets close to the center of the laser spot, then it slows down and stops. The contribution of Gaussian laser heating around the beam spot on the domain wall motion is confirmed. With the increased current density, SOT enables the domain wall propagation regardless of the laser polarization. Still some helicity-dependence optical effect is clearly demonstrated and left-circularly (σ-) polarized laser beam gives the maximum velocity for a domain wall propagation towards M↑ domains. With the reversed current, the domain wall moves in the opposite direction as a propagation towards M↓ domains, which is also against the direction of electron flow, and right-circularly (σ+) polarized laser beam induces a larger velocity as it favors a propagation towards M↓ domains [Figure 4-2 (d)]. The experiments were repeated, and the above conclusions can be confirmed.

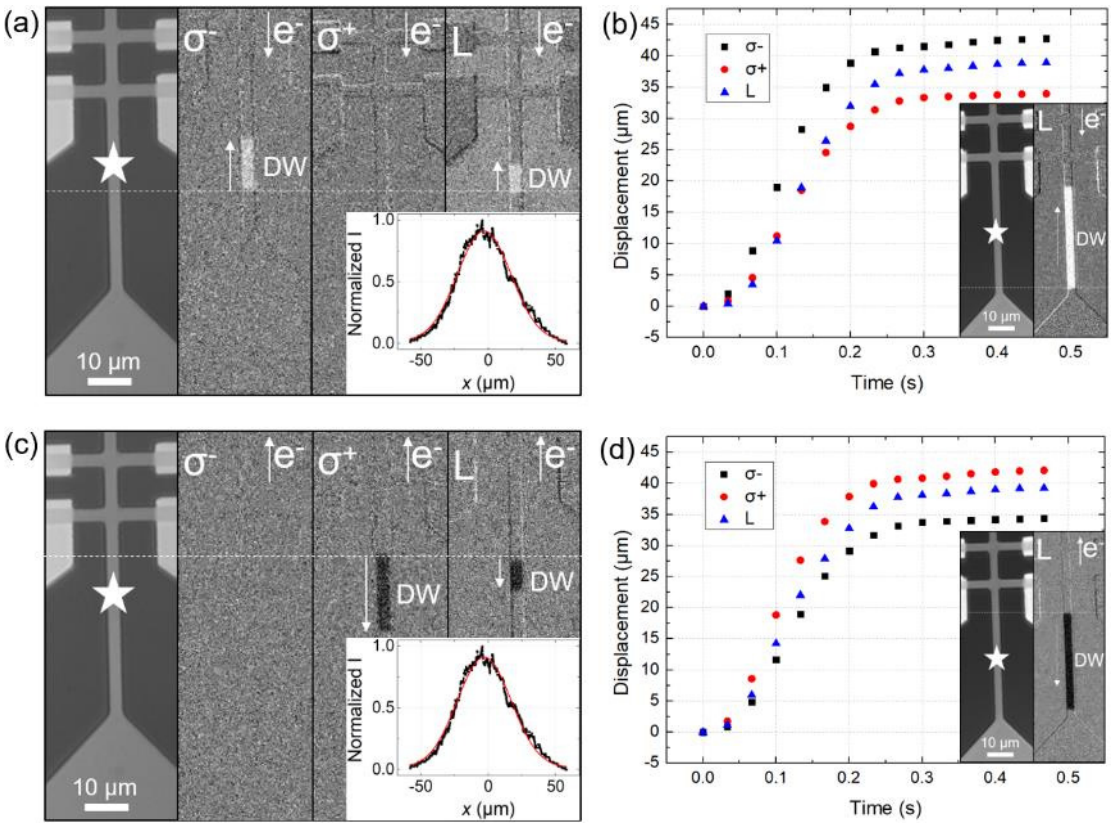

Figure 4-2 (a and c) Kerr images of a 4 μm Co/Ni/Co ferromagnetic wire. Linear (L), right-circularly (σ+) and left-circularly (σ-) polarized laser beams shine on the sample with a fluence of 4 mJ/cm^2 for 10 seconds, together with synchronized 10 μs current pulses of 7.3×10^6 A/cm^2 (5 kHz repetition rate), both of which are below the threshold value for domain wall motion. Inset: Gaussian profile of the laser spot with a FWHM of 47 μm. (b and d) Time evolution of the domain wall displacement of a 4 μm Co/Ni/Co ferromagnetic wire from domain wall video recording and analysis with the APREX TRACK software as a

function of the laser polarization, where the current density was increased to 14.6×10^6 A/cm^2. Inset: Kerr images of a 4 μm Co/Ni/Co ferromagnetic wire, which shows the domain wall motion with Linear (L) laser beam. The initial magnetization saturation direction is M↑ and the white contrast corresponds to a reversal to M↓ for (a) and (b). The initial magnetization saturation direction is M↓ and the black contrast corresponds to a reversal to M↑ for (c) and (d).

4.1.3 Effect of synchronization delay between the electron and light stimuli on domain wall motion

In order to determine the respective contributions of current pulses and laser pulses, the synchronization delay between the electron and light stimuli, and the duration of current pulses were varied. In this experiment, the center of the laser spot was placed close to the domain wall, as indicated by the star in Figure 4-3 (a). During 10 seconds, linear (L) laser pulses with a 4 mJ/cm^2 fluence and current pulses of 11×10^6 A/cm^2 were injected in the wire with a 5 kHz repetition rate. The synchronization delay between the laser pulses and the current pulses was then adjusted. Both the laser fluence and the current density were below the threshold values for domain wall motion, and a single domain wall was priorly nucleated in the wire after a magnetization saturation with M↑.

Results are shown in Figure 4-3 (a). For both 5 μs and 10 μs current pulse durations, we can observe that the domain wall propagates the same distance if the laser pulses and the current pulses are synchronized. In this case, the two effects act simultaneously and the domain wall propagation is limited by the competition between the Gaussian laser heating, SOT and the pinning. The bottom dashed line corresponds to the initial domain wall position. The study on the effect of the synchronization delay on the domain wall motion shows that the domain wall propagates less when the current pulse is injected after the laser pulse and the domain wall propagation distance is smaller for 100 μs delay than 50 or 150 μs.

As the absorption of laser energy occurs only in the electronic bath, the laser pulses induce a large increase of electron temperature T_e. Then, the electronic thermal bath is coupled to that of the phonons, which induces a fast decrease of temperature to a stable value. The center of the laser beam spot normally corresponds to a maximum

temperature of 600 K [QUE18]. The temperature increases ΔT due to the current heating from an injected current pulse [CUR10] can be estimated by Eq. (3.4), where the specific heat C = 750 J kg^{-1} K^{-1}, thermal conduction K = 1.4 W m^{-1} K^{-1}, density d = 2500 kg/m^3 for the glass substrate, R = 1.2 kΩ, ω = 4 μm, l = 94 μm for the wire. With the current density J of 11×10^6 A/cm^2 and the pulse duration τ_{pulse} of 5 μs or 10 μs, the temperature increase from an injected current pulse is 38 K or 59 K. The wire temperature increase as a function of time can be estimated, as shown in Figure 4-3 (b). When the current pulse comes 50 μs after the laser pulse, the residual laser heating helps the spin-orbit torque to move the domain wall. When the delay is 100 μs, the residual laser heating is small when the following current pulse is injected, while the residual heating of this current pulse is small when the following laser pulse arrives, but they can induce a shorter domain wall displacement distance. In the case of 150 μs, a larger displacement can be obtained due to the larger residual current heating. The table of Figure 4-3 (a) shows the domain wall displacement distance for each pulse duration and synchronization delay. The integration of residual temperature increases ΔT in regard to the time is indicated by the blue shadow area in Figure 4-3 (b) for each pulse duration and synchronization delay, where a larger blue shadow area (integration of ΔT in regard to the time) induces a larger domain wall displacement. The larger displacement with 10 μs current pulse duration than that with 5 μs shows the role of current heating, as 10 μs current pulse induces a larger ΔT with a longer applied time.

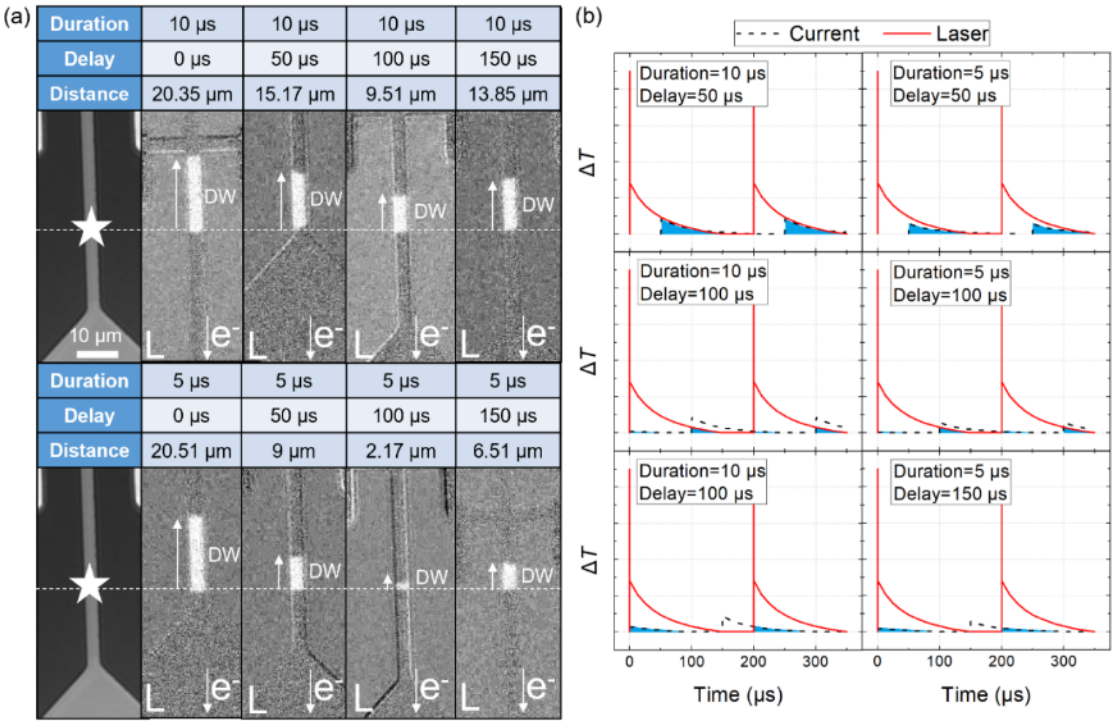

Figure 4-3 (a) Kerr images of 4 µm Co/Ni/Co ferromagnetic wires. Linear (L) laser beam shines on the sample with a fluence of 4 mJ/cm² for 10 seconds, together with current pulses of 11×10⁶ A/cm² and 10 µs or 5µs pulse duration with a synchronization delay of 0, 50, 100, 150 µs (200 µs period), both of which are below the threshold values for domain wall motion. The initial magnetization saturation direction is M↑ and the white contrast corresponds to a reversal to M↓. The domain wall displacement distances are shown in the table for each pulse duration and synchronization delay. (b) Schematic of the wire temperature increase Δ*T* due to the laser pulses (red solid lines) and the current pulses (black dashed lines) as a function of time with the synchronization delay of 50, 100 or 150 µs (200 µs period). The integration of residual temperature increases Δ*T* in regard to the time is indicated as a blue shadow area for each pulse duration and synchronization delay.

4.1.4 Energy consumption

To quantify the energy consumption in the presence of laser pulses, we have compared the current-induced domain wall motion as shown in Figure 3-9 (a) and the domain wall motion combining synchronized current pulses and laser pulses as shown in Figure 4-2 (a) with left-circularly (σ-) polarized laser beam.

For the 1st case, the current energy per pulse gives $E_{current} = U^2t/R = 5.4\times10^{-7}$ J with a voltage of 9 V (corresponding to 16.5×10^6 A/cm^2), a pulse duration of 8 µs and a wire resistance of 1.2 kΩ. 10 seconds of current pulses with a 5 kHz frequency give 50000 pulses, which enable a domain wall displacement of 18.5 µm for a total energy of

14.6×10^{-4} J/μm. For the 2nd case, we estimate the current energy per pulse $E_{current}$ = 1.3×10^{-7} J with a voltage of 4 V (corresponding to 7.3×10^{6} A/cm^2), a pulse duration of 10 μs and a wire resistance of 1.2 kΩ, and the laser energy per pulse $E_{laser} = P/f$=0.7×10^{-7} J with a laser power of 0.35 mW (corresponding to 4 J/cm^2) and a 5 kHz repetition rate. A domain wall displacement of 15.3 μm is obtained with 50000 synchronized pulses and a total energy of 6.5×10^{-4} J/μm is deduced.

Therefore, we can conclude that in the presence of circularly polarized laser pulses, the energy consumption and the threshold current density due to SOT for domain wall motion can be reduced by more than 50% in the investigated wire.

4.1.5 Modeling

The above results demonstrate that domain wall motion is driven by the combination of helicity-dependent optical effect, heating from laser pulses and SOT. In order to analyze the different contributions, we have used the Fatuzzo-Labrune model [FAT62, LAB89] to evaluate the domain wall velocity and displacement under the combined action of laser pulses and current pulses:

$$v = v_0 \exp\left(-\frac{E - 2H_{eff}M_S V_B}{k_B T}\right) \tag{4.1}$$

where E is the pinning energy barrier to be overcome in order to enable the domain wall motion within the Barkhausen volume V_B, H_{eff} is an effective field that contains the contribution from the laser pulses and the current pulses.

The SOT can be described by an effective field H_{SHE} originating from the SHE whose direction favors domain wall propagation against the direction of electron flow [RYU13]: $H_{SHE} = (\hbar\theta_{SH}J)/(2eM_St)$, where $\hbar = h/2\pi$ and h is the Planck constant, e represents the elementary charge, θ_{SH} is the Spin Hall angle, t stands for the total thickness of the ferromagnetic layers. The Gaussian laser heating due to the laser profile [inset of Figure 4-2 (a)] gives a Gaussian distribution of temperature T and we assume that the center of the laser beam corresponds to a maximum temperature of 600 K for

linear polarization [QUE18]. The laser helicity induces an effective field H_σ and the direction of H_σ depends on the laser helicity.

A current density J of 7.3×10^6 A/cm^2 and 10 μs pulse duration gives a H_{SHE} of 16 Oe with M_S = 770 emu/cm^3, t = 1.2 nm and θ_{SH} = 0.04, and also a temperature increase ΔT of 25.8 K to T according to Eq. (3.4). σ- and σ+ induce the H_σ that favors M↓ and M↑, respectively, where $|H_\sigma|$ equals to 3 Oe. As the domain wall velocity v is a function of the Gaussian distribution of H_σ and T related to the laser position x with $v = dx/dt = f(x)$, by solving the equation, the domain wall displacement x as a function of the time t can then be obtained, as shown in Figure 4-4, where $V_B = 10^{-23}$ m^{-3} is in the same order of magnitude of V_B for Co ultrathin films with PMA [KIR93] and $v_0 = 2\times10^{12}$ μm/s is the initial DW velocity. The SOT enables the domain wall motion against the direction of the electron flow. Domain wall motion moves significantly with left-circularly (σ-) laser pulses due to the laser helicity, and Gaussian laser heating enables the domain wall motion to the beam center with linear (L) light, while right-circularly (σ+) laser pulses give almost no domain wall motion. The simulations as shown in Figure 4-4 (a) tend to indicate the dominated role of the laser polarization with smaller current density, which provide the domain wall motion results similar to those previously described in Figure 4-2 (a).

With a larger H_{SHE} of 32 Oe and a higher ΔT of 103.3 K corresponding to J of 14.6×10^6 A/cm^2, the domain wall displacement is shown in Figure 4-4 (b), where the larger spin-orbit torque induces the domain wall motion regardless of the laser polarization. The three regimes of domain wall displacement confirm the effect of Gaussian laser heating, while SOT plays a dominant role on the domain wall velocity, which is in agreement with the experimental results as shown in Figure 4-2 (b).

In addition, based on the above conditions, implementing only current pulses or laser pulses into the model gives a vanishing domain wall velocity and displacement profile. Therefore, the main results of domain wall motion experiments combining current pulses and laser pulses are well reproduced.

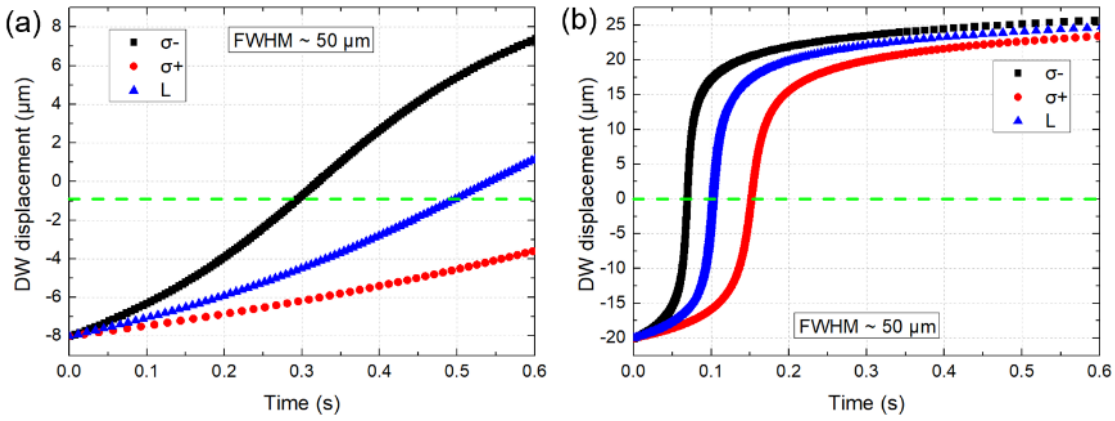

Figure 4-4 Time-dependent simulations of the domain wall displacement based on the Fatuzzo-Labrune model. The domain wall motion is induced by synchronized current pulses and linear (L), right-circularly (σ+) or left-circularly (σ-) polarized laser pulses with (a) a H_{SHE} of 16 Oe, a Gaussian distribution of H_σ and T with a FWHM of ~50 μm, (b) a H_{SHE} of 32 Oe, a Gaussian distribution of H_σ and T with a FWHM of ~50 μm. Similar results for the domain wall displacement as shown in Figure 4-2 (a) and Figure 4-2 (b) are obtained in (a) and (b), respectively. The green dashed line corresponds to the position of the laser beam center.

4.2 Combined effect of helicity-dependent optical effect and STT in Ta(3 nm)/Pt(3 nm)/Co(0.3 nm)/Ni(0.6 nm)/Co(0.3 nm)/Pt(3 nm) structure

4.2.1 Domain wall motion combining synchronized femtosecond laser pulses and short current pulses

As 10 μs current pulses with a current density lower than 16.5×10^6 A/cm^2 and a 5 kHz frequency cannot move the domain wall in the 4 μm wire, the current pulses were synchronized with the 5-kHz-repetition-rate laser pulses. The inset of Figure 4-5 displays the laser intensity as a function of the distance from the laser beam center. The beam diameter (FWHM) is 47 μm. The center of the laser spot, indicated by the star in Figure 4-5, was placed at 8 μm away from the domain wall. In the following, a single domain wall was nucleated in the wire before the experiments and laser fluences below the threshold were used to assist the current-driven domain wall motion.

Figure 4-5 shows domain wall motion assisted by left-circularly (σ-) polarized, linear (L) polarized, and right-circularly (σ+) polarized laser pulses. The Kerr images were

taken after applying both current pulses of 7.3×10^6 A/cm^2 and laser pulses of 4 mJ/cm^2 for 10 seconds. The right-circularly (σ+) laser beam favors a large domain wall displacement as the domain wall moves further than the center of the beam, while linear (L) polarized laser beam induces a moderate domain wall displacement towards the beam center. In contrast, the left-circularly (σ-) polarized laser beam pins the domain wall.

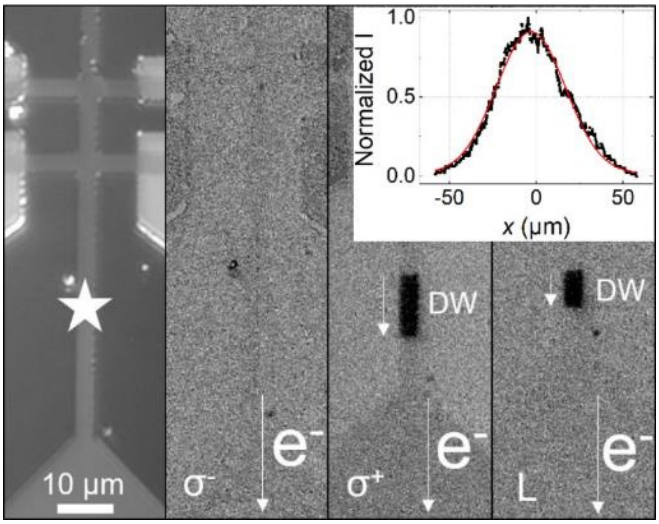

Figure 4-5 Kerr images of the 4 μm wire after linear (L), right-circularly (σ+) and left-circularly (σ-) polarized laser beams shined at a fixed point indicated by the star (8 μm away from the domain wall) on the wire with a fluence of 4 mJ/cm^2 below the all-optical helicity-dependent switching threshold for 10 seconds, together with synchronized current pulses of 7.3×10^6 A/cm^2 and 10 μs pulse duration (5 kHz repetition rate). The initial magnetization saturation direction is M↓, and the black contrast corresponds to a reversal to M↑. Inset: Gaussian profile of the laser spot with a FWHM of 47 μm.

4.2.2 Modeling

As the SOT contribution is excluded and the STT contribution is estimated, we can model the combined effect of STT and the fs laser beam. For the circularly polarized laser beam, the roles of the temperature and the effective field need to be distinguished. As the domain wall displacement induced by right-circularly (σ+) polarized laser beam exceeds the beam center and left-circularly (σ-) polarized laser beam doesn't induce any domain wall motion in Figure 4-5, the laser helicity can be interpreted as an effective field H_σ and the direction of H_σ depends on the laser helicity. H_σ can be explained by the IFE [COR16, QUE18], where σ− favors a reversal to M↓ and σ+ favors

a reversal to M↑. MCD can also induce an effective field. As σ- is more absorbed by the M↑ domain and σ+ is more absorbed by the M↓ domain [GOR16, QUE18], a difference in absorption of M↑ and M↓ domains results in an additional temperature gradient and an effective field of MCD across the domain wall, where σ- favors a propagation towards M↑ domain and σ+ favors a propagation towards M↓ domain [SCH14, QUE18]. For linear (L) polarized laser beam without IFE or MCD, our results in Figure 4-5 show that the domain wall propagates towards the hot region at the beam center due to the laser temperature distribution [inset of Figure 4-5].

The Fatuzzo-Labrune model [FAT62, LAB89] described in Eq. (4.1) can be used to evaluate the domain wall velocity under the combined action of the laser pulses and the current pulses, where $H_{eff} = H_\sigma + H_{STT}$ is an effective field that contains the contribution from helicity-dependent fs laser and STT, and $H_{STT} = \varepsilon J$.

The laser beam can be regarded as a Gaussian distribution of effective field H_σ and temperature T, where H_σ and T represent the contribution from laser helicity and laser temperature distribution, respectively. We assume that the center of the laser beam gives a maximum temperature of 600 K [QUE18] and a $|H_\sigma|$ of 3 Oe. A current density J of 7.3×10^6 A/cm^2 gives a $|H_{STT}|$ of 4.38 Oe and a temperature rise of 29 K to T according to Eq. (3.4) with the pulse duration τ_{pulse} of 10 μs. As the domain wall velocity v is a function of the Gaussian distribution of H_σ and T related to the laser position x with $v = dx/dt = f(x)$, by solving the equation, the domain wall displacement x as a function of the time t can then be obtained with $V_B = 10^{-23}$ m^{-3}, $v_0 = 2\times10^{12}$ μm/s, as shown in Figure 4-6. The σ+, linear, and σ- beams induce large, moderate, and small domain wall displacements, respectively. The simulation results are in agreement with the experiment in Figure 4-5. Based on those parameters, implementing only current pulses or laser pulses into the model gives a vanishing domain wall velocity, which explains why only the current pulses or laser pulses (below all-optical switching threshold) cannot drive the domain wall motion in our system.

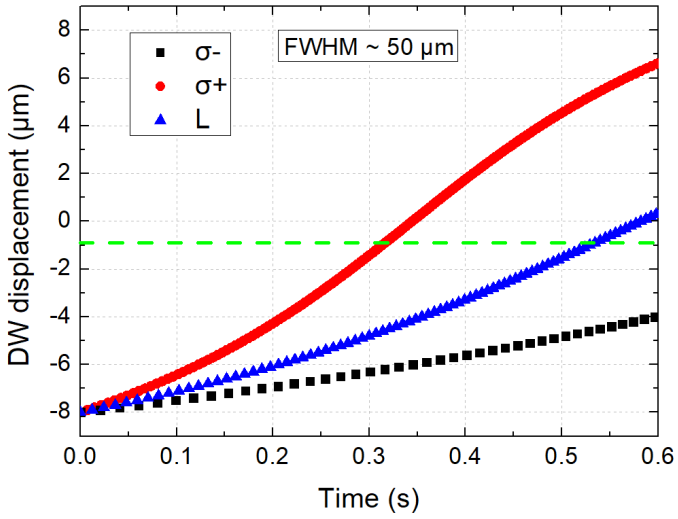

Figure 4-6 Time-dependent simulations of the domain wall displacement based on the Fatuzzo-Labrune model. The domain wall motion is induced by synchronized current pulses and linear (L), right-circularly (σ+) or left-circularly (σ-) polarized laser pulses with a H_{STT} of 4.38 Oe, a Gaussian distribution of H_σ and T with a FWHM of ~50 µm. The green dashed line corresponds to the position of the laser beam center.

4.3 Domain wall logic based on the combined effect

Domain wall logic is based on using domain walls to generate logic gates. Magnetic logic has the advantage of non-volatility. Circuits with instant ON/OFF operations can be developed and magnetic logic can be reconfigurable to execute different logic gate operations like AND, OR, NAND, NOR, etc.

Magnetic wires can be used to construct a complete logic architecture. For instance, Allwood *et al.* realized domain wall logic gates (NOT, Fan-out, cross-over) at low power by using a rotating field induced domain wall motion in sub-micro magnetic wires [ALL05] as seen in Figure 4-7.

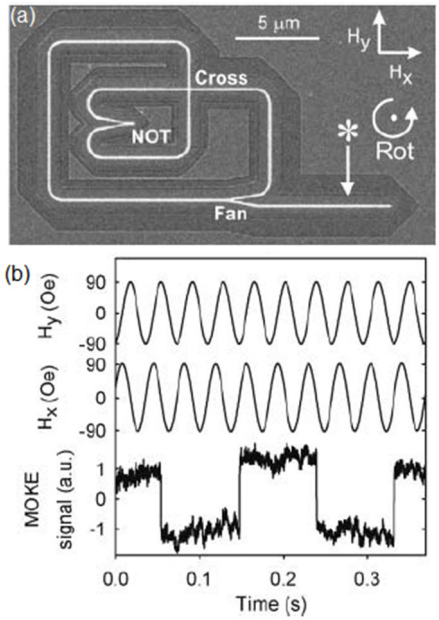

Figure 4-7 (a) Focused ion beam (FIB) image of the magnetic wire consisting of NOT, fan-out and cross-over functions. The white lines indicate the magnetic material. The rotating field (H_x and H_y) and the sense of rotation (Rot) are indicated. (b) Magnetic-optic Kerr effect signals from the asterisk position of the wire with $H_x = H_y = 91$ Oe [ALL05].

Based on the domain wall motion resulted from the contribution of the helicity-dependent optical effect and the SOT, we propose that our structure, which mimics a magnetic domain wall gate, can form the building block for generating Boolean logic functions. An example for an AND gate is given in Figure 4-8. The principle is very similar to the concept of the magnetic shift register based on moving domain walls in a racetrack geometry [PAR08, PAR15, ALL02, ALL05, FRA12]. The elementary logic device consists of a domain wall wire, with two inputs 'A' and 'B' that involve synchronized injected current and illuminated left-circularly (σ-) polarized laser beam, both of which are below the threshold values for domain wall motion, and an output 'C' that involves detecting the local magnetization through the anomalous Hall effect (AHE). The device functions are as follows: First, a single domain wall is nucleated in the wire, away from the AHE detection area, with the output 'C' set to the resistance state '0' (M↑). If none or either of the stimuli 'A' and 'B' are applied, no domain wall motion is induced, which leaves the output 'C' in the '0' state. However, if both stimuli are on (inputs 'A' and 'B' set to '1'), the generated domain wall can propagate along the wire, driven by the combination of SOT 'A' and the helicity-dependent optical

effect ‘B’, leading to the resistance state ‘1’ (M↓) of the output ‘C’. Therefore, a promising approach towards low power spintronic-photonic logic device can be constructed using domain wall motion in magnetic wires.

In addition, after nucleation of a single domain wall and set of output ‘C’ in the resistance state ‘0’ (M↑), implementing left-circularly (σ-) or right-circularly (σ+) polarized laser beam for input ‘A’ along with current for input ‘B’ leads to the ‘1’ or ‘0’ state for output ‘C’, which can be used for direct detection of laser helicity.

As the domain walls store data non-volatilely into magnetic states, the proposed domain wall logic can be used for the logic-in-memory applications, where nonvolatile memory elements are distributed over a logic-circuit plane [STO70, MAT08].

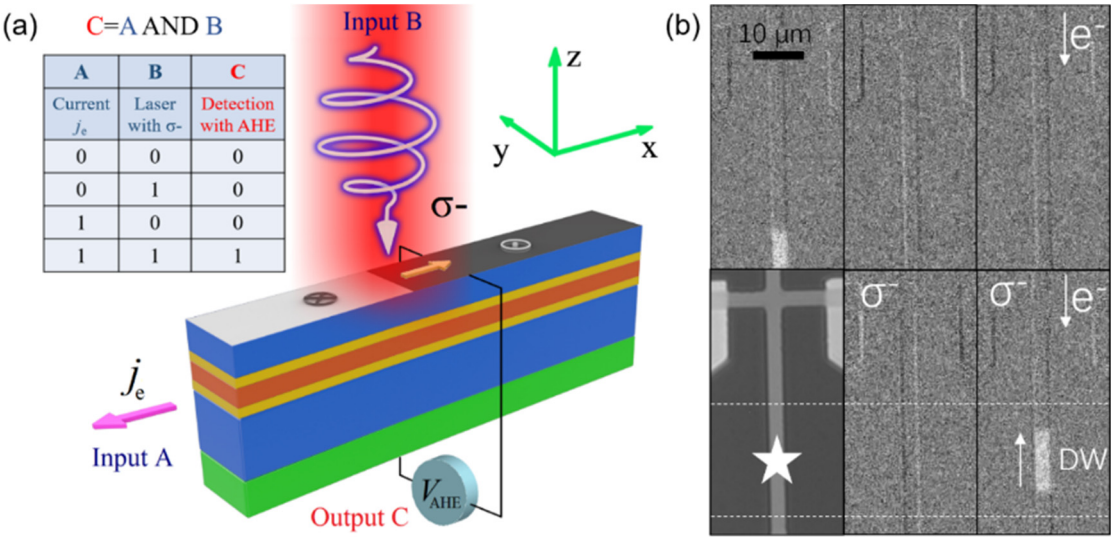

Figure 4-8 (a) Design of an AND logic function by using laser pulses and current pulses to control the domain wall motion. Inputs ‘A’ and ‘B’ are synchronized current pulses and laser pulses below the threshold values for domain wall motion, and output ‘C’ serves as read out for the magnetization direction in the wire through AHE. This scheme corresponds to a logical AND operation and the AND table is shown on top. (b) Kerr images of 4 μm Co/Ni/Co ferromagnetic wires. The current pulses and laser pulses are the same with Figure 4-2 (a). The top three figures correspond to the domain wall nucleation, domain wall motion with input (A,B) = (0,0) and (1,0), while the bottom three figures correspond to the indication of the laser spot center in the wire as a star, domain wall motion with (A,B) = (0,1) and (1,1). The initial magnetization saturation direction is M↑ and the white contrast corresponds to a reversal to M↓.

4.4 Summary

In this section, we have experimentally demonstrated helicity-dependent domain wall motion by using both short current pulses and femtosecond laser pulses simultaneously in Co/Ni/Co ultra-thin film wires with perpendicular anisotropy. Circularly polarized laser pulses propagate or pin the domain wall depending on the laser helicity. The domain wall motion results from the interplay of helicity-dependence optical effect, heating from laser pulses and current pulses, and SOT or STT. The combined effect can be described using the Fatuzzo-Labrune model and examining the physical contributions of different parameters.

In addition, we have demonstrated how such an effect can be exploited to generate Boolean logic functions, which enables a new class of low power spintronic-photonic devices beyond the conventional approach of all-optical switching or all-current switching for data storage.

CONCLUSIONS AND PERSPECTIVES

General conclusions

In this thesis, we experimentally demonstrate optical helicity-dependent domain wall motion by combining synchronized femtosecond laser pulses and short current pulses in Co/Ni/Co ultra-thin film wires with strong perpendicular anisotropy. Two sets of magnetic wire structures have been investigated to manipulate domain wall with the combined effects of helicity-dependent optical effect with SOT in Ta(3 nm)/Pt(5 nm)/Co(0.3 nm)/Ni(0.6 nm)/Co(0.3 nm)/Pt(2 nm) and with STT in Ta(3 nm)/Pt(3 nm)/Co(0.3 nm)/Ni(0.6 nm)/Co(0.3 nm)/Pt(3 nm).

For the former case, the contributions from helicity-dependent optical effect, heating from laser pulses and current pulses, and SOT were investigated by tuning the laser polarization, the current amplitude, the current pulse duration, and the synchronization delay between the electron and light stimuli. Due to the contribution of helicity-dependence optical effect, the energy consumption and the threshold current density due to SOT for domain wall motion can be reduced by more than 50% in the investigated wire.

For the latter case, through the asymmetric field-driven domain expansion and the second harmonic measurements, we exclude the SOT contribution as the sample has a small effective DMI field H_{DMI} of +100 Oe and a spin Hall angle of +0.04. The effective field due to STT, which is the dominate contribution, is analyzed by pulsed-field domain wall measurements. The density of current pulses as low as 7.3×10^6 A/cm^2 is sufficient for STT-induced domain wall motion without any magnetic field.

The origin of these effects has been modelled by considering the effective field due to the polarized laser beam, the effective field due to SOT or STT, and the Gaussian temperature distribution of the laser spot using the Fatuzzo-Labrune model.

The laser polarization provides a new degree of freedom to manipulate the domain wall in magnetic devices, where the displacement of the domain wall is found to be dependent on the laser helicity, and domain wall can remain pinned under one laser circular helicity while depinned for the opposite circular helicity.

In addition, based on the joint effect combining SOT and helicity-dependent laser pulses, an optoelectronic logic-in-memory device has been experimentally demonstrated.

Perspectives

In this thesis, we have provided an energy-efficient approach that highlights a new path towards efficient domain wall manipulation, which enables the development of new families of spintronic nanodevices combining photonics and electronics.

In the following, we propose some possible routes that can further improve our work.

1. The current pulse durations used in our experiments of domain wall motion combining current and laser are in the order of microsecond. Nanosecond current pulses can be used with the following advantages: first, the domain wall velocity can be greatly improved as shown in reference [RYU13], which is essential for the racetrack memory concept; secondly, ns pulse duration is closer to that of the femtosecond laser, and more physical phenomena can be explored by combining ns current and fs laser. New sample holder should be designed to be compatible with the femtosecond laser set-up, while the components of the holder should be carefully chosen considering the impedance matching for the nanosecond pulses.

2. We have proposed an AND gate based on the combined effect of current and laser pulses for optoelectronic logic-in-memory applications. Recently, several logic structures based on laser pulses have been proposed [CHA18, CHA19, RIO19]. More domain wall logic structures can be explored base on the combination of helicity-dependent optical effect and SOT or STT for photonic-spintronic in-memory computing.

BIBLIOGRAPHY

[AKE05] Åkerman J. Toward a universal memory[J]. Science , 2005, 308(5721): 508-510.

[AKY15] Akyol M, Yu G, Alzate J G, et al. Current-induced spin-orbit torque switching of perpendicularly magnetized Hf|CoFeB|MgO and Hf|CoFeB|TaOx structures[J]. Applied Physics Letters, 2015, 106(16): 162409.

[ALL02] Allwood D A, Xiong G, Cooke M D, et al. Submicrometer ferromagnetic NOT gate and shift register[J]. Science, 2002, 296(5575): 2003-2006.

[ALL05] Allwood D A, Xiong G, Faulkner C C, et al. Magnetic domain-wall logic[J]. science, 2005, 309(5741): 1688-1692.

[AND18] Andrieu S, Hauet T, Gottwald M, et al. Co/Ni multilayers for spintronics: high spin-polarization and tunable magnetic anisotropy[J]. Physical review materials, 2018, 2(6):064410.

[ANT19] Determination of the orientation of the Dzyaloshinskii–Moriya vector from the local geometry: https://en.wikipedia.org/wiki/Antisymmetric_exchange (accessed on Jan 22, 2019)

[BAI88] Baibich M N, Broto J M, Fert A, et al. Giant magnetoresistance of (001) Fe/(001) Cr magnetic superlattices[J]. Physical review letters, 1988, 61(21): 2472.

[BAT14] Battiato M, Barbalinardo G, Oppeneer P M. Quantum theory of the inverse Faraday effect[J]. Physical Review B, 2014, 89(1): 014413.

[BEA96] Beaurepaire E, Merle J C, Daunois A, et al. Ultrafast spin dynamics in ferromagnetic nickel[J]. Physical review letters, 1996, 76(22): 4250.

[BER16] Bergeard N, Hehn M, Mangin S, et al. Hot-electron-induced ultrafast demagnetization in Co/Pt multilayers[J]. Physical review letters, 2016, 117(14):

147203.

[BER84] Berger L. Exchange interaction between ferromagnetic domain wall and electric current in very thin metallic films[J]. Journal of Applied Physics, 1984, 55(6): 1954-1956.

[BER96] Berger L. Emission of spin waves by a magnetic multilayer traversed by a current[J]. Physical Review B, 1996, 54(13): 9353.

[BIN89] Binasch G, Grünberg P, Saurenbach F, et al. Enhanced magnetoresistance in layered magnetic structures with antiferromagnetic interlayer exchange[J]. Physical review B, 1989, 39(7): 4828.

[BOB75] Bobeck A H, Bonyhard P I, Geusic J E. Magnetic bubbles—An emerging new memory technology[J]. Proceedings of the IEEE, 1975, 63(8): 1176-1195.

[BOD07] Bode M, Heide M, Von Bergmann K et al. Chiral magnetic order at surfaces driven by inversion asymmetry[J]. Nature, 2007, 447(7141): 190–193.

[BOU08] Boulle O, Kimling J, Warnicke P, et al. Nonadiabatic spin transfer torque in high anisotropy magnetic nanowires with narrow domain walls[J]. Physical review letters, 2008, 101(21): 216601.

[BOU11] Boulle O, Malinowski G, Kläui M. Current-induced domain wall motion in nanoscale ferromagnetic elements[J]. Materials Science and Engineering: R: Reports, 2011, 72(9): 159-187.

[BUR09] Burrowes C, Mihai A P, Ravelosona D, et al. Non-adiabatic spin-torques in narrow magnetic domain walls[J]. Nature Physics, 2010, 6(1): 17.

[CHA18] Chakravarty A, Mentink J H, Davies C S, et al. Supervised learning of an opto-magnetic neural network with ultrashort laser pulses[J]. arXiv preprint arXiv:1811.01375, 2018.

[CHA19] Chakraborty I, Saha G, Roy K. Photonic In-Memory Computing Primitive for Spiking Neural Networks Using Phase-Change Materials[J]. Physical Review

Applied, 2019, 11(1): 014063.

[CHE15] Chen G, Schmid A K. Imaging and tailoring the chirality of domain walls in magnetic films[J]. Advanced Materials, 2015, 27(38): 5738-5743.

[COR13] Cortés-Ortuño D, Landeros P. Influence of the Dzyaloshinskii–Moriya interaction on the spin-wave spectra of thin films[J]. Journal of Physics: Condensed Matter, 2013, 25(15): 156001.

[COR16] Cornelissen T D, Córdoba R, Koopmans B. Microscopic model for all optical switching in ferromagnets[J]. Applied Physics Letters, 2016, 108(14): 142405.

[CUB14] Cubukcu M, Boulle O, Drouard M, et al. Spin-orbit torque magnetization switching of a three-terminal perpendicular magnetic tunnel junction[J]. Applied Physics Lett ers, 2014, 104(4): 042406.

[CUR10] Curiale J, Lemaître A, Faini G, et al. Track heating study for current-induced domain wall motion experiments[J]. Applied Physics Letters, 2010, 97(24): 243505.

[DAA92] Daalderop G H O, Kelly P J, Den Broeder F J A. Prediction and confirmation of perpendicular magnetic anisotropy in Co/Ni multilayers[J]. Physical review letters, 1992, 68(5): 682.

[DIA07] Diao Z, Li Z, Wang S, et al. Spin-transfer torque switching in magnetic tunnel junctions and spin-transfer torque random access memory[J]. Journal of Physics: Condensed Matter, 2007, 19(16): 165209.

[DJA05] Djayaprawira D D, Tsunekawa K, Nagai M, et al. 230% room-temperature magnetoresistance in CoFeB/MgO/CoFeB magnetic tunnel junctions[J]. Applied Physics Letters, 2005, 86(9): 092502.

[DZY58] Dzyaloshinsky I. A thermodynamic theory of “weak” ferromagnetism of antiferromagnetics[J]. Journal of Physics and Chemistry of Solids, 1958, 4(4): 241-255

[ELH16] El Hadri M S, Hehn M, Pirro P, et al. Domain size criterion for the observation of all-optical helicity-dependent switching in magnetic thin films[J]. Physical Review

B, 2016, 94(6): 064419.

[ELH17] El Hadri M S, Hehn M, Malinowski G, et al. Materials and devices for all-optical helicity-dependent switching[J]. Journal of Physics D: Applied Physics, 2017, 50(13): 133002.

[ELH18] El Hadri M S, Hehn M, Malinowski G, et al. Suppression of all-optical switching in He+-irradiated Co/Pt multilayers: influence of the domain-wall energy[J]. Journal of Physics D: Applied Physics, 2018, 51(21): 215004.

[EMO13] Emori S, Bauer U, Ahn S M, et al. Current-driven dynamics of chiral ferromagnetic domain walls[J]. Nature materials, 2013, 12(7): 611.

[ENG05] Engel B N, Akerman J, Butcher B, et al. A 4-Mb toggle MRAM based on a novel bit and switching method[J]. IEEE Transactions on Magnetics, 2005, 41(1): 132-136.

[ESC13] Eschenlohr A, Battiato M, Maldonado P, et al. Ultrafast spin transport as key to femtosecond demagnetization[J]. Nature materials, 2013, 12(4): 332.

[FAT62] Fatuzzo E. Theoretical considerations on the switching transient in ferroelectrics[J]. Physical review, 1962, 127(6): 1999.

[FER08] Fert A. Nobel lecture: Origin, development, and future of spintronics[J]. Reviews of Modern Physics, 2008, 80(4): 1517.

[FER17] Fert A, Reyren N, Cros V. Magnetic skyrmions: advances in physics and potential applications[J]. Nature Reviews Materials, 2017, 2(7): 17031.

[FER90] Fert A. Magnetic and transport properties of metallic multilayers[C]. Materials Science Forum. Trans Tech Publications, 1990, 59: 439-480.

[FON56] Foner S. Vibrating sample magnetometer[J]. Review of Scientific Instruments, 1956, 27(7): 548-548.

[FON59] Foner S. Versatile and sensitive vibrating-sample magnetometer[J]. Review of Scientific Instruments, 1959, 30(7): 548-557.

[FRA12] Franken J H, Swagten H J M, Koopmans B. Shift registers based on magnetic domain wall ratchets with perpendicular anisotropy[J]. Nature nanotechnology, 2012, 7(8): 499.

[FRA15] Franke K J A, Van de Wiele B, Shirahata Y, et al. Reversible electric-field-driven magnetic domain-wall motion[J]. Physical Review X, 2015, 5(1): 011010.

[FUK15] Fukami S, Zhang C, DuttaGupta S, et al. Magnetization switching by spin–orbit torque in an antiferromagnet–ferromagnet bilayer system[J]. Nature materials, 2016, 15(5): 535.

[FUL16] Fullerton E E, Childress J R. Spintronics, magnetoresistive heads, and the emergence of the digital world[J]. Proceedings of the IEEE, 2016, 104(10): 1787-1795.

[GIR09] Girod S, Gottwald M, Andrieu S, et al. Strong perpendicular magnetic anisotropy in Ni/Co (111) single crystal superlattices[J]. Applied Physics Letters, 2009, 94(26): 262504.

[GOR16] Gorchon J, Yang Y, Bokor J. Model for multishot all-thermal all-optical switching in ferromagnets[J]. Physical Review B, 2016, 94(2): 020409.

[GRU08] Grünberg P A. Nobel lecture: From spin waves to giant magnetoresistance and beyond[J]. Reviews of Modern Physics, 2008, 80(4): 1531.

[HAA13] Haazen P P J, Murè E, Franken J H, et al. Domain wall depinning governed by the spin Hall effect[J]. Nature materials, 2013, 12(4): 299.

[HAN17] Han J, Richardella A, Siddiqui S A, et al. Room-temperature spin-orbit torque switching induced by a topological insulator[J]. Physical review letters, 2017, 119(7): 077702.

[HAY08] Hayashi M, Thomas L, Moriya R, et al. Current-controlled magnetic domain-wall nanowire shift register[J]. Science, 2008, 320(5873): 209-211.

[HIR99] Hirsch J E. Spin hall effect[J]. Physical Review Letters, 1999, 83(9): 1834.

[HOF13] Hoffmann A. Spin Hall effects in metals[J]. IEEE transactions on magnetics,

2013, 49(10): 5172-5193.

[HOS05] Hosomi M, Yamagishi H, Yamamoto T, et al. A novel nonvolatile memory with spin torque transfer magnetization switching: Spin-RAM[C]//IEEE International Electron Devices Meeting, 2005. IEDM Technical Digest. IEEE, 2005: 459-462.

[HUA08] Huai Y. Spin-transfer torque MRAM (STT-MRAM): Challenges and prospects[J]. AAPPS bulletin, 2008, 18(6): 33-40.

[HUA15] Huang K F, Wang D S, Lin H H, et al. Engineering spin-orbit torque in Co/Pt multilayers with perpendicular magnetic anisotropy[J]. Applied Physics Letters, 2015, 107(23): 232407.

[JE13] Je S G, Kim D H, Yoo S C, et al. Asymmetric magnetic domain-wall motion by the Dzyaloshinskii-Moriya interaction[J]. Physical Review B, 2013, 88(21): 214401.

[KHO12] Khorsand A R, Savoini M, Kirilyuk A, et al. Role of magnetic circular dichroism in all-optical magnetic recording[J]. Physical review letters, 2012, 108(12): 127205.

[KIM12] Kim J S, Stärk M, Kläui M, et al. Interaction between propagating spin waves and domain walls on a ferromagnetic nanowire[J]. Physical Review B, 2012, 85(17): 174428.

[KIM13] Kim J, Sinha J, Hayashi M, et al. Layer thickness dependence of the current-induced effective field vector in Ta|CoFeB|MgO[J]. Nature materials, 2013, 12(3): 240.

[KIR93] Kirilyuk A, Ferré J, Renard D. Temperature effects on domain wall dynamics in ultrathin ferromagnetic films[J]. IEEE transactions on magnetics, 1993, 29(6): 2518-2520.

[KIR10] Kirilyuk A, Kimel A V, Rasing T. Ultrafast optical manipulation of magnetic order[J]. Reviews of Modern Physics, 2010, 82(3): 2731.

[KOY11] Koyama T, Chiba D, Ueda K, et al. Observation of the intrinsic pinning of a magnetic domain wall in a ferromagnetic nanowire[J]. Nature mater ials, 2011, 10(3):

194.

[LAB89] Labrune M, Andrieu S, Rio F, et al. Time dependence of the magnetization process of RE-TM alloys[J]. Journal of magnetism and magnetic materials, 1989, 80(2-3): 211-218.

[LAH12] Lahtinen T H E, Franke K J A, Van Dijken S. Electric-field control of magnetic domain wall motion and local magnetization reversal[J]. Scientific reports, 2012, 2: 258.

[LAM14] Lambert C H, Mangin S, Varaprasad B S D C S, et al. All-optical control of ferromagnetic thin films and nanostructures[J]. Science , 2014, 345(6202): 1337-1340.

[LEG17] Le Gall S, Vernier N, Montaigne F, et al. Effect of spin transfer torque on domain wall motion regimes in [Co/Ni] superlattice wires[J]. Physical Review B, 2017, 95(18): 184419.

[LEG18] Le Gall S, Montaigne F, Lacour D, et al. Statistical study of domain-wall depinning induced by magnetic field and current in an epitaxial Co/Ni-based spin-valve wire[J]. Physical Review B, 2018, 98(2): 024401.

[LI04] Li Z, Zhang S. Domain-wall dynamics driven by adiabatic spin-transfer torques[J]. Physical Review B, 2004, 70(2): 024417.

[LIU11] Liu L, Moriyama T, Ralph D C, et al. Spin-torque ferromagnetic resonance induced by the spin Hall effect[J]. Physical review letters, 2011, 106(3): 036601.

[LIU12] Liu L, Pai C F, Li Y, et al. Spin-torque switching with the giant spin Hall effect of tantalum[J]. Science, 2012, 336(6081): 555-558.

[LIU17] Liu P, Lin X, Xu Y, et al. Optically tunable magnetoresistance effect: From mechanism to novel device application[J]. Materials, 2017, 11(1): 47.

[MAL08] Malinowski G, Dalla Longa F, Rietjens J H H, et al. Control of speed and efficiency of ultrafast demagnetization by direct transfer of spin angular momentum[J]. Nature Physics, 2008, 4(11): 855.

[MAN14] Mangin S, Gottwald M, Lambert C H, et al. Engineered materials for all-optical helicity-dependent magnetic switching[J]. Nature materials, 2014, 13(3): 286.

[MAT08] Matsunaga S, Hayakawa J, Ikeda S, et al. Fabrication of a nonvolatile full adder based on logic-in-memory architecture using magnetic tunnel junctions[J]. Applied Physics Express, 2008, 1(9): 091301.

[MET07] Metaxas P J, Jamet J P, Mougin A et al. Creep and flow regimes of magnetic domain-wall motion in ultrathin Pt/Co/Pt films with perpendicular anisotropy[J]. Physical Review Letters, 2007, 99(21): 217208.

[MIR10] Miron I M, Gaudin G, Auffret S, et al. Current-driven spin torque induced by the Rashba effect in a ferromagnetic metal layer[J]. Nature materials, 2010, 9(3): 230.

[MIR11] Miron I M, Garello K, Gaudin G, et al. Perpendicular switching of a single ferromagnetic layer induced by in-plane current injection[J]. Nature, 2011, 476(7359): 189.

[MIT09] Miron I M, Zermatten P J, Gaudin G, et al. Domain wall spin torquemeter[J]. Physical review letters, 2009, 102(13): 137202.

[MIY95] Miyazaki T, Tezuka N. Giant magnetic tunneling effect in Fe/Al2O3/Fe junction[J]. Journal of Magnetism and Magnetic Materials, 1995, 139(3): L231-L234.

[MOO08] Moore T A, Miron I M, Gaudin G, et al. High domain wall velocities induced by current in ultrathin Pt/Co/AlOx wires with perpendicular magnetic anisotropy[J]. Applied Physics Letters, 2008, 93(26): 262504.

[MOO95] Moodera J S, Kinder L R, Wong T M, et al. Large magnetoresistance at room temperature in ferromagnetic thin film tunnel junctions[J]. Physical review letters, 1995, 74(16): 3273.

[MOR16] Moreau-Luchaire C, Moutafis C, Reyren N, et al. Additive interfacial chiral interaction in multilayers for stabilization of small individual skyrmions at room temperature[J]. Nature nanotechnology, 2016, 11(5): 444.

[MOR60] Moriya T. Anisotropic superexchange interaction and weak ferromagnetism[J]. Physical Review, 1960, 120(1): 91.

[NGU16] Nguyen M H, Ralph D C, Buhrman R A. Spin torque study of the spin Hall conductivity and spin diffusion length in platinum thin films with varying resistivity[J]. Physical review letters, 2016, 116(12): 126601.

[OAK05] Oakberg T. Magneto-optic Kerr effect[EB/OL]. HINDS Instruments, 2005, 1–6. http://www.hindsinstruments.com/wp-content/uploads/Magneto-Optic-Kerr-Effect.pdf.

[OBO15] Oboril F, Bishnoi R, Ebrahimi M, et al. Evaluation of hybrid memory technologies using SOT-MRAM for on-chip cache hierarchy[J]. IEEE Transactions on Computer-Aided Design of Integrated Circuits and Systems, 2015, 34(3): 367-380.

[PAI12] Pai C F, Liu L, Li Y, et al. Spin transfer torque devices utilizing the giant spin Hall effect of tungsten[J]. Applied Physics Letters, 2012, 101(12): 122404.

[PAR04] Parkin S S P, Kaiser C, Panchula A, et al. Giant tunnelling magnetoresistance at room temperature with MgO (100) tunnel barriers[J]. Nature materials, 2004, 3(12): 862.

[PAR08] Parkin S S P, Hayashi M, Thomas L. Magnetic domain-wall racetrack memory[J]. Science, 2008, 320(5873): 190-194.

[PAR15] Parkin S, Yang S H. Memory on the racetrack[J]. Nature nanotechnology, 2015, 10(3): 195.

[PAR17] Pardo R D, Torres W S, Kolton A B, et al. Universal depinning transition of domain walls in ultrathin ferromagnets[J]. Physical Revie w B, 2017, 95(18): 184434.

[PAR18] Parlak U, Adam R, Bürgler D E, et al. Optically induced magnetization reversal in [Co/Pt] N multilayers: Role of domain wall dynamics[J]. Physical Review B, 2018, 98(21): 214443.

[QUE18] Quessab Y, Medapalli R, El Hadri M S, et al. Helicity-dependent all-optical

domain wall motion in ferromagnetic thin films[J]. Physical Review B, 2018, 97(5): 054419.

[QUE18] Quessab Y. Mechanism and size effects of helicity-dependent all-optical magnetization switching in ferromagnetic thin films[D]. Université de Lorraine, 2018.

[RAD11] Radu I, Vahaplar K, Stamm C, et al. Transient ferromagnetic-like state mediating ultrafast reversal of antiferromagnetically coupled spins[J]. Nature, 2011, 472(7342): 205.

[RAV07] Ravelosona D, Mangin S, Katine J A, et al. Threshold currents to move domain walls in films with perpendicular anisotropy[J]. Applied physics letters, 2007, 90(7): 072508.

[RIO19] Ríos C, Youngblood N, Cheng Z, et al. In-memory computing on a photonic platform[J]. Science Advances, 2019, 5(2): eaau5759.

[RYU13] Ryu K S, Thomas L, Yang S H, et al. Chiral spin torque at magnetic domain walls[J]. Nature nanotechnology, 2013, 8(7): 527.

[RYU14] Ryu K S, Yang S H, Thomas L, et al. Chiral spin torque arising from proximity-induced magnetization[J]. Nature communications, 2014, 5: 3910.

[SAM13] Sampaio J, Cros V, Rohart S et al. Nucleation, stability and current-induced motion of isolated magnetic skyrmions in nanostructures[J]. Nature nanotechnology, Nature Publishing Group, 2013, 8(11): 839–844.

[SCH12] Schellekens A J, Van den Brink A, Franken J H, et al. Electric-field control of domain wall motion in perpendicularly magnetized materials[J]. Nature communications, 2012, 3: 847.

[SCH14] Schlickeiser F, Ritzmann U, Hinzke D, et al. Role of entropy in domain wall motion in thermal gradients[J]. Physical review letters, 2014, 113(9): 097201.

[SIN15] Sinova J, Valenzuela S O, Wunderlich J, et al. Spin hall effects[J]. Reviews of Modern Physics, 2015, 87(4): 1213.

[SLO96] Slonczewski J C. Current-driven excitation of magnetic multilayers[J]. Journal of Magnetism and Magnetic Materials, 1996, 159(1-2): L1-L7.

[STA07] Stanciu C D, Hansteen F, Kimel A V, et al. All-optical magnetic recording with circularly polarized light[J]. Physical review letters, 2007, 99(4): 047601.

[STO70] Stone H S. A logic-in-memory computer[J]. IEEE Transactions on Computers, 1970, 100(1): 73-78.

[STU17] Stupakiewicz A, Szerenos K, Afanasiev D, et al. Ultrafast nonthermal photo-magnetic recording in transparent medium[J]. Nature, 2017, 542(7639): 71.

[SUG09] Sugiura K, Takahashi S, Amano M, et al. Ion beam etching technology for highdensity spin transfer torque magnetic random access memory[J]. Japanese Journal of Applied Physics, 2009, 48(8S1): 08HD02.

[SUW15] Suwa M, Tsukahara S, Watarai H. Faraday rotation imaging microscope with microsecond pulse magnet[J]. Journal of Magnetism and Magnetic Materials, Elsevier, 2015, 393: 562–568.

[TAT04] Tatara G, Kohno H. Theory of current-driven domain wall motion: Spin transfer versus momentum transfer[J]. Physical review letters, 2004, 92(8): 086601.

[TEH03] Tehrani S, Slaughter J M, Deherrera M, et al. Magnetoresistive random access memory using magnetic tunnel junctions[J]. Proceedings of the IEEE, 2003, 91(5): 703-714.

[TET15] Tetienne J P, Hingant T, Martínez L J, et al. The nature of domain walls in ultrathin ferromagnets revealed by scanning nanomagnetometry[J]. Nature communications, 2015, 6: 6733.

[THI05] Thiaville A, Nakatani Y, Miltat J, et al. Micromagnetic understanding of current-driven domain wall motion in patterned nanowires[J]. EPL (Europhysics Letters), 2005, 69(6): 990.

[THI12] Thiaville A, Rohart S, Jué É, et al. Dynamics of Dzyaloshinskii domain walls

in ultrathin magnetic films[J]. EPL (Europhysics Letters), 2012, 100(5): 57002.

[TOR15] Torrejon J, Garcia-Sanchez F, Taniguchi T, et al. Current-driven asymmetric magnetization switching in perpendicularly magnetized CoFeB/MgO heterostructures[J]. Physical Review B, 2015, 91(21): 214434.

[UED11] Ueda K, Koyama T, Chiba D, et al. Current-induced magnetic domain wall motion in Co/Ni nanowire at low temperature[J]. Applied physics express, 2011, 4(6): 063003.

[UED15] Ueda K, Kim K J, Taniguchi T, et al. In-plane field-driven crossover in the spin-torque mechanism acting on magnetic domain walls in Co/Ni[J]. Physical Review B, 2015, 91(6): 060405.

[VAN16] Van den Brink A, Vermijs G, Solignac A, et al. Field-free magnetization reversal by spin-Hall effect and exchange bias[J]. Nature communications, 2016, 7: 10854.

[WAN14] Wang X, Guo G, Nie Y, et al. Microwave-assisted domain-wall motion induced by alternating spin-polarized current[J]. Physical Review B, 2014, 89(14): 144418.

[WEI08] Weinberger P. John Kerr and his effects found in 1877 and 1878[J]. Philosophical Magazine Letters, 2008, 88(12): 897-907.

[WOL10] Wolf S A, Lu J, Stan M R, et al. The promise of nanomagnetics and spintronics for future logic and universal memory[J]. Proceedings of the IEEE, 2010, 98(12): 2155-2168.

[WOO14] Woo S, Mann M, Tan A J, et al. Enhanced spin-orbit torques in Pt/Co/Ta heterostructures[J]. Applied Physics Letters, 2014, 105(21): 212404.

[YAK15] Yakushiji K, Kubota H, Fukushima A, et al. Perpendicular magnetic tunnel junction with enhanced anisotropy obtained by utilizing an Ir/Co interface[J]. Applied Physics Express, 2015, 9(1): 013003.

[YAN15] Yang S H, Ryu K S, Parkin S. Domain-wall velocities of up to 750 m s− 1 driven by exchange-coupling torque in synthetic antiferromagnets[J]. Nature nanotechnology, 2015, 10(3): 221.

[YOS12] Yoshimura Y, Koyama T, Chiba D, et al. Current-induced domain wall motion in perpendicularly magnetized Co/Ni nanowire under in-plane magnetic fields[J]. Applied Physics Express, 2012, 5(6): 063001.

[YOU15] You L, Lee O J, Bhowmik D, et al. Switching of perpendicularly polarized nanomagnets with spin orbit torque without an external magnetic field by engineering a tilted anisotropy[J]. Proceedings of the National Academy of Sciences, 2015, 112(33): 10310-10315.

[YU14] Yu G, Upadhyaya P, Fan Y, et al. Switching of perpendicular magnetization by spin–orbit torques in the absence of external magnetic fields[J]. Nature nanotechnology, 2014, 9(7): 548.

[YUA04] Yuasa S, Nagahama T, Fukushima A, et al. Giant room-temperature magnetoresistance in single-crystal Fe/MgO/Fe magnetic tunnel junctions[J]. Nature materials, 2004, 3(12): 868.

[ZHA04] Zhang J, Levy P M, Zhang S, et al. Identification of transverse spin currents in noncollinear magnetic structures[J]. Physical review letters, 2004, 93(25): 256602.

[ZHA11] Zhao W S, Devolder T, Lakys Y, et al. Design considerations and strategies for high-reliable STT-MRAM[J]. Microelectronics Reliability, 2011, 51(9-11): 1454-1458.

[ZHA15] Zhang W, Han W, Jiang X, et al. Role of transparency of platinum–ferromagnet interfaces in determining the intrinsic magnitude of the spin Hall effect[J]. Nature Physics, 2015, 11(6): 496.

[ZHA16] Zhao W, Wang Z, Peng S, et al. Recent progresses in spin transfer torque-based magnetoresistive random access memory (STT-MRAM) [J]. Chinese Science Bulletin, 2011, 56(56): 3072.

[ZHA18] Zhang X. Spin-polarized current-induced domain wall motion in CoFeB nanowires[D]. Université Paris-Saclay, 2018.

LIST OF ABBREVIATIONS

AF	antiferromagnetic
AGM	alternating gradient magnetometer
AHE	anomalous Hall effect
AO-HDS	all-optical helicity-dependent switching
AO-HIS	all-optical helicity-independent switching
AOS	all-optical switching
BLS	Brillouin light scattering
CCD	charge coupled device
DC	direct current
DL	damping-like
DMI	Dzyaloshinskii-Moriya interaction
DRAM	dynamic random-access memory
DW	domain wall
FIB	focused ion beam
FL	field-like
fs	femtosecond
FWHM	full width at half maximum
GMR	giant magnetoresistance
HM	heavy metal
IBE	ion beam etching
IFE	inverse Faraday effect
LED	light emitting diode
LLG	Landau-Lifshitz-Gilbert
M3TM	magnetic three-temperature model
MBE	molecular beam epitaxy
MCD	magnetic circular dichroism
ML	monolayer
MRAM	magnetic random-access memory
MTJ	magnetic tunneling junction
PMA	perpendicular magnetic anisotropy
PVD	physical vapor deposition
RF	radio frequency
RHEED	reflection high energy electron diffraction
SHE	spin Hall effect
SIMS	secondary ion mass spectroscopy
SOC	spin-orbit coupling
SOT	spin-orbit torque
SQUID	Superconducting QUantum Interference Device

SRAM	static random-access memory
STT	spin-transfer torque
TD	thermal demagnetization
TMR	tunnel magnetoresistance
UV	ultraviolet
VSM	vibrating sample magnetometer

LIST OF PUBLICATIONS

Journals

[1] **Zhang B**, Xu Y, Zhao W, et al. Energy-Efficient Domain-Wall Motion Governed by the Interplay of Helicity-Dependent Optical Effect and Spin-Orbit Torque[J]. Physical Review Applied, 2019, 11(3): 034001. DOI: 10.1103/PhysRevApplied.11.034001. (IF: 4.782, JCR: Q1)

[2] **Zhang B**, Xu Y, Zhao W, et al. Domain-wall motion induced by spin transfer torque delivered by helicity-dependent femtosecond laser[J]. Physical Review B, 2019, 99(14): 144402. DOI: 10.1103/PhysRevB.99.144402 (IF: 3.813, JCR: Q2)

[3] **Zhang B**, Cao A, Qiao J, et al. Influence of heavy metal materials on magnetic properties of Pt/Co/heavy metal tri-layered structures[J]. Applied Physics Letters, 2017, 110(1): 012405. DOI: 10.1063/1.4973477. (IF: 3.495, JCR: Q1)

[4] Zhao W, Zhao X, **Zhang B**, et al. Failure analysis in magnetic tunnel junction nanopillar with interfacial perpendicular magnetic anisotropy[J]. Materials, 2016, 9(1): 41. DOI: 10.3390/ma9010041. (IF: 2.467, JCR: Q2)

[5] Liu P, Lin X, Xu Y, **Zhang B**, et al. Optically tunable magnetoresistance effect: From mechanism to novel device application[J]. Materials, 2017, 11(1): 47. DOI: 10.3390/ma11010047. (IF: 2.467, JCR: Q2)

Conferences

[1] **Zhang B**, Xu Y, Zhao W, et al. Experimental demonstration of domain wall logic-in-memory through helicity-dependent optical effect and spin-orbit torque [C]. 3rd International Workshop on Spintronic Memory and Logic. Beijing, China, October 16-20, 2018. (Poster presentation, 17/10/2018)

[2] **Zhang B**, Cao A, Qiao J, et al. Influence of heavy metal materials on magnetic

properties of Pt/Co/heavy metal tri-layered structures[C]. IEEE International Magnetics Conference (Intermag). Dublin, Ireland, April 24-28, 2017. (Poster presentation, AN-16, 25/04/2017)

Summer schools

[1] Introductory course on Magnetic Random Access Memory (InMRAM), Grenoble, France. July 3-5, 2017

[2] IEEE Magnetic Society Summer School. Tohoku University, Sendai, Japan. July 10-15, 2016.

RÉSUMÉ EN FRANÇAIS

Depuis la première observation de la désaimantation ultra-rapide dans des films de Ni soumis à des impulsions laser, un intérêt majeur de la communauté spintronique a été de manipuler l'aimantation de films minces magnétiques par des impulsions laser ultra-courtes. Ces études ont conduit à la découverte de la commutation toute optique (AOS, all-optical switching) de l'aimantation dans des films d'alliage ferrimagnétique en utilisant des impulsions laser femto-seconde (fs). L'AOS permet un renversement de l'aimantation du matériau magnétique sans champ magnétique externe et la direction de l'aimantation résultante est donnée par la polarisation circulaire droite ou gauche de la lumière.

La manipulation de l'aimantation par impulsions laser a ensuite été démontrée dans une variété de matériaux ferromagnétiques, incluant des alliages, des hétérostructures, ou des films ferromagnétiques simples, ouvrant ainsi la voie à une intégration de l'écriture toute optique dans les dispositifs spintroniques.

En parallèle, la propagation de parois magnétiques induite par un courant polarisé en spin a suscité intérêt majeur pour des applications aux mémoires solides ultra-denses (concept de racetrack memory) ou à la logique magnétique. Cependant, les densités de courant requises pour le mouvement des parois magnétiques sont encore trop élevées pour permettre la réalisation de nanodispositifs à faible puissance.

L'objet de cette thèse est d'explorer la possibilité de combiner un courant polarisé en spin et une excitation laser femtoseconde pour manipuler à basse puissance des parois magnétiques dans des dispositifs spintroniques. Différents matériaux sont explorés, pour optimiser conjointement les effets optiques et de courant polarisé en spin. Finalement, le développement de nouvelles fonctions logiques contrôlées optiquement et électriquement est aussi proposé.

Les couches minces étudiées dans cette thèse concernant des multicouches de type [Co/Ni] sont déposées par pulvérisation cathodique sur des substrats de verre. Nous avons tout d'abord optimisé les épaisseurs relatives de Co et Ni pour obtenir l'anisotropie magnétique perpendiculaire des multicouches de type Ta(3 nm)/Pt(x nm)/Co(0.3 nm)/Ni(0.6 nm)/Co(0.3 nm)/Pt(y nm), comme le montre la figure 1.

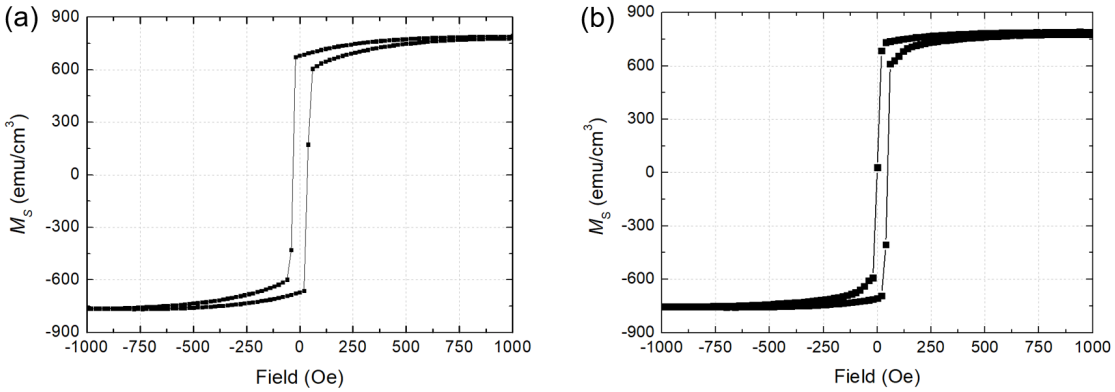

Figure 1 Boucles d'hystérésis obtenues en mesurant l'aimantation en fonction du champ perpendiculaire aux couches minces pour (a) l'échantillons Ta(3 nm)/Pt(5 nm)/Co(0.3 nm)/Ni(0.6 nm)/Co(0.3 nm)/Pt(2 nm) et (b) l'échantillons Ta(3 nm)/Pt(3 nm)/Co(0.3 nm)/Ni(0.6 nm)/Co(0.3 nm)/Pt(3 nm).

Des effets de l'AOS sont ensuite montré sur le fil de 4 µm fabriqué à base des films susmentionnés, comme le montre la figure 2. Pour étudier ensuite la combinaison de l'effet optique dépendant de la polarisation et du courant polarisé sur le mouvement des parois de domaine, des impulsions de courant de 10 µs et des impulsions laser de 35 fs ont été synchronisées à un taux de répétition de 5 kHz.

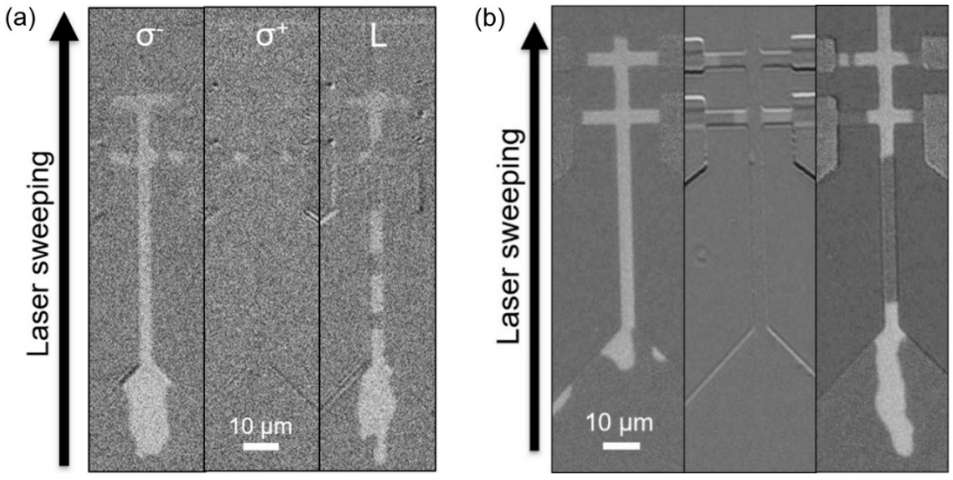

Figure 2 Images de Kerr des pistes des structures de (a) l'échantillons Ta(3 nm)/Pt(5

nm)/Co(0.3 nm)/Ni(0.6 nm)/Co(0.3 nm)/Pt(2 nm) et de (b) l'échantillons Ta(3 nm)/Pt(3 nm)/Co(0.3 nm)/Ni(0.6 nm)/Co(0.3 nm)/Pt(3 nm). Des faisceaux de laser polarisés linéaires (L), circulaires droits (σ+) et circulaires gauches (σ-) ont été balayés sur les pistes.

Dans un premier temps, nous nous sommes focalisés sur des structures de type Ta(3 nm)/Pt(5 nm)/Co(0.3 nm)/Ni(0.6 nm)/Co(0.3 nm)/Pt(2 nm). Nous avons tout d'abord étudié la propagation de parois magnétiques dans des pistes sous l'effet d'un courant polarisé seul. Cette étude indique des densités de courant élevées de l'ordre de 16.5×10^6 A/cm^2 et une propagation des parois magnétiques contre le flux d'électrons, comme le montre la figure 3 (a). Ce résultat est consistant avec la présence de parois magnétiques chirales de type Néel qui se propagent par Couples de Spin Orbite (SOT, Spin Orbit Torque) dû à la présence des couches de Pt. L'effet de SOT est mis en évidence par la présence d'un champ effectif H_{DMI} de +300 Oe lié à l'interaction de Dyalozinski Moriya.

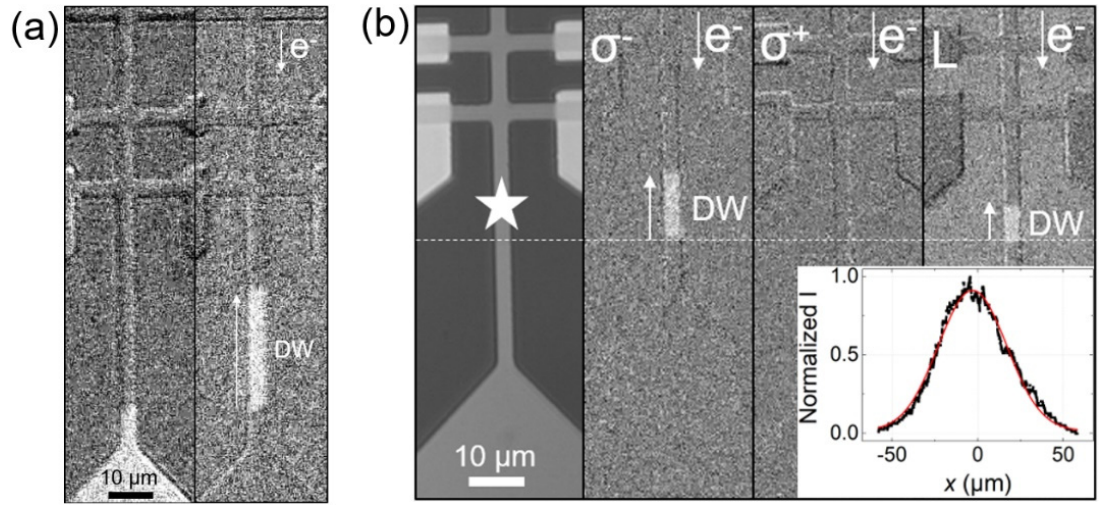

Figure 3 Images de Kerr des pistes des structures de type Ta(3 nm)/Pt(5 nm)/Co(0.3 nm)/Ni(0.6 nm)/Co(0.3 nm)/Pt(2 nm). (a) Des impulsions de courant sont injectées. (b) Des faisceaux de laser polarisé brillent et des impulsions synchronisées de courant sont injectés. Encart: Profil gaussien du point de laser.

L'effet combiné des impulsions synchronisées de laser femtoseconde et de SOT sur le mouvement de parois magnétiques est ensuite démontré avec des densités de courant de l'ordre de 7.3×10^6 A/cm^2 et une fluence du laser de 4 mJ/cm^2, valeurs inférieures aux valeurs de seuil pour chaque effet, comme le montre la figure 3 (b). Un faisceau de laser polarisé linéaire (L) induit une propagation jusqu'au centre du faisceau, qui correspond à la région la plus chaude [encart de figure 3 (b)], en raison du chauffage

au laser gaussien. Les mesures obtenues pour les deux polarisations circulaires démontrent que les parois de domaine peuvent rester piégées sous une hélicité circulaire du laser et dépiégées par une hélicité circulaire opposée. Nous montrons aussi qu'en présence d'impulsions laser avec la polarisation σ-, la consommation d'énergie relative à la propagation de parois magnétiques peut être réduite de plus de 50% par rapport à un courant polarisé seul, ce qui est un résultat majeur de cette thèse.

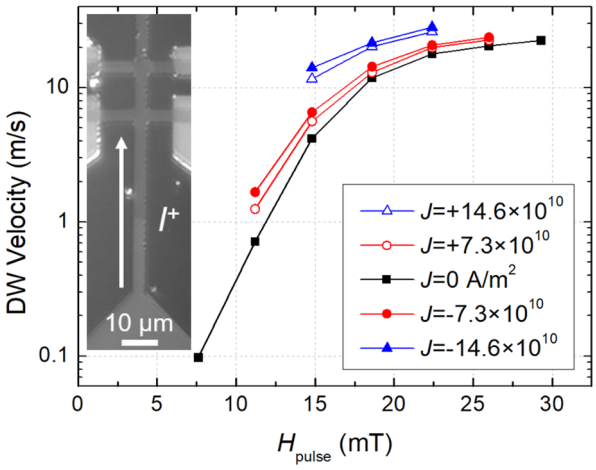

Figure 4 Vitesse des parois de domaine en fonction du champ magnétique extérieur H_{pulse}.

Dans une autre série d'échantillons du type Ta(3 nm)/Pt(5 nm)/Co(0.3 nm)/Ni(0.6 nm)/Co(0.3 nm)/Pt(2 nm), nous avons mis en évidence un effet de SOT négligeable en utilisant une technique de seconde harmonique et une contribution plus importante des couples de transfert de spin (STT, Spin Transfer Torque) qui favorisent une propagation de parois magnétiques dans le sens des électrons de conduction. Dans ce cas les parois magnétiques ne peuvent pas se propager sous l'effet d'un courant polarisé seul mais la propagation doit être assistée par un champ magnétique extérieur, comme le montre la figure 4. Nous avons aussi montré une contribution non négligeable de l'effet Joule. Finalement, la combinaison de densités de courant faible de l'ordre de 7.3×10^6 A/cm^2 et d'impulsions laser de 4 mJ/cm^2 favorise la propagation de parois magnétiques dans le même sens que les électrons de conduction, comme le montre la figure 5.

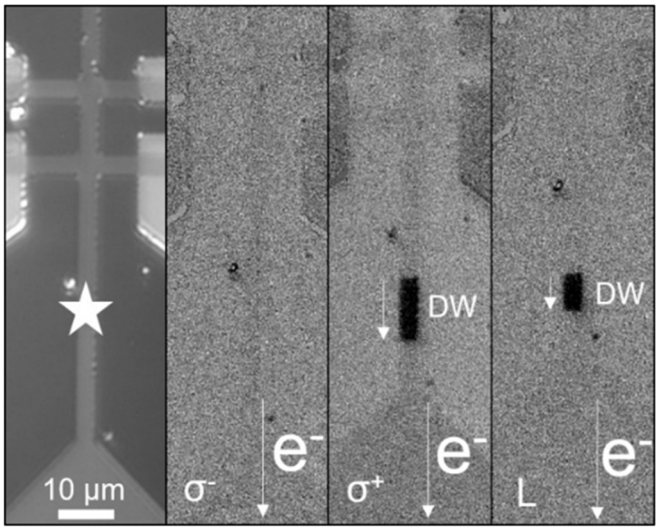

Figure 5 Images de Kerr des pistes des structures de type Ta(3 nm)/Pt(3 nm)/Co(0.3 nm)/Ni(0.6 nm)/Co(0.3 nm)/Pt(3 nm). Des faisceaux de laser polarisés brillent et des impulsions synchronisées de courant sont injectés.

Nous avons ainsi démontré qu'un faisceau laser polarisé permet d'assister la propagation de parois sous courant polarisé dans les deux configurations de STT et SOT. Sur la base de ce résultat important, nous proposons finalement des fonctions logiques booléennes contrôlées optiquement et électriquement comme les portes AND, comme le montre la figure 6.

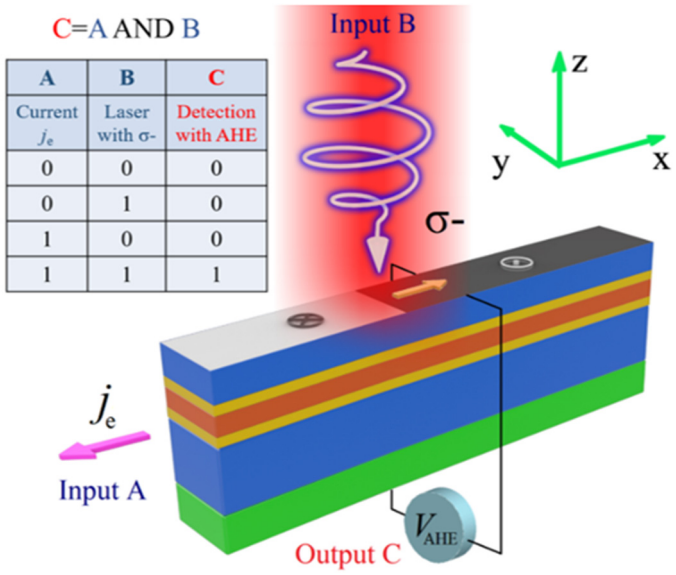

Figure 6 Conception d'une porte logique AND avec le mouvement des parois de domaine. Les entrées «A» et «B» sont des impulsions synchronisées de courant et de laser inférieures aux valeurs de seuil pour le mouvement des parois de domaine, et la sortie «C» sert de lecture de la direction de l'aimantation dans la piste à travers l'effet Hall anormal (AHE, anomalous Hall effect). Ce schéma correspond à une opération logique AND et la table AND

est affichée en haut.

université PARIS-SACLAY
ÉCOLE DOCTORALE
Physique et ingénierie : électrons, photons, sciences du vivant (EOBE)

Titre : Propagation des Parois de Domaines Combinant Courant Polarisé et Commutation Toute Optique

Mots clés : Parois de domaines, courant polarisé, laser femtoseconde, mémoire racetrack, spintronique, fils multicouches magnétiques

Résumé : Depuis la première observation de désaimantation ultra-rapide dans des films de Ni soumis à une excitation laser pulsée, on a assisté à un grand intérêt de comprendre l'interaction entre les impulsions laser ultra-courtes et l'aimantation. Ces études ont conduit à la découverte de la commutation toute optique de l'aimantation dans un alliage de film ferrimagnétique en utilisant des impulsions laser femtosecondes. La commutation toute optique permet un renversement de l'aimantation d'un matériau magnétique sans champ magnétique externe. La direction de l'aimantation résultante est donnée par la polarisation circulaire droite ou gauche de la lumière.

La manipulation de l'aimantation par un faisceau laser a longtemps été limité à un seul type de matériau, mais ce mécanisme s'est avéré être un phénomène plus général qui s'applique à une grande variété de matériaux ferromagnétiques, y compris des alliages, des empilements et des hétérostructures, ainsi que des hétérostructures ferrimagnétiques synthétiques de terres-rares. Récemment, nous avons observé le même phénomène dans des films ferromagnétiques simples, ouvrant ainsi la voie à une intégration de l'écriture toute optique dans les dispositifs spintroniques.

De plus, dans des matériaux de type [Co/Pt] ou [Co/Ni] avec une polarisation de spin élevée et une anisotropie magnétique perpendiculaire contrôlable, un mouvement de parois de domaines induit par un courant polarisé peut être observé dans des pistes magnétiques (couple spin-orbite ou couple de transfert de spin), ce qui présente un grand intérêt pour des applications spintroniques basse consommation et de densité élevée, telles que le concept de mémoire racetrack et la logique magnétique. Cependant, la densité de courant requise pour le mouvement des parois de domaines est encore trop élevée pour permettre la réalisation de dispositifs à faible puissance.

Dans ce contexte innovant, la recherche effectuée dans le cadre de ma thèse s'est concentrée sur la manipulation de parois de domaines dans les pistes fabriquées à partir de films minces à forte anisotropie magnétique perpendiculaire en combinant à la fois les effets du courant polarisé et ceux de la commutation toute optique. Différents films minces ont été explorés afin d'étudier les effets combinés optiques dépendant de l'hélicité et des couples spin-orbite ou de transfert de spin sur le mouvement des parois de domaines. Nous avons montré que les parois de domaines peuvent rester piégées sous une hélicité circulaire du laser et dépiégées par une hélicité circulaire opposée, et la densité de courant polarisé seuil peut être considérablement réduite en utilisant un laser femtoseconde. Nos résultats sont prometteurs pour le développement de nouveaux dispositifs photoniques-spintroniques de faible puissance.

Université Paris-Saclay
Espace Technologique / Immeuble Discovery
Route de l'Orme aux Merisiers RD 128 / 91190 Saint-Aubin, France

université PARIS-SACLAY
ÉCOLE DOCTORALE
Physique et ingénierie : électrons, photons, sciences du vivant (EOBE)

Title : Domain Wall Propagation Combining Spin-Polarized Current and All-Optical Switching

Keywords : Domain wall, spin-polarized current, femtosecond laser, racetrack memory, spintronics, magnetic multilayered wires

Abstract : Since the first observation of ultrafast demagnetization in Ni films arising from a pulsed laser excitation, there has been a strong interest in understanding the interaction between ultrashort laser pulses and magnetization. These studies have led to the discovery of all-optical switching (AOS) of magnetization in a ferrimagnetic film alloy of GdFeCo using femtosecond laser pulses. All-optical switching enables an energy-efficient magnetization reversal of the magnetic material with no external magnetic field, where the direction of the resulting magnetization is given by the right or left circular polarization of the light.

The manipulation of magnetization through laser beam has long been restricted to one material, though it turned out to be a more general phenomenon for a variety of ferromagnetic materials, including alloys, multilayers and heterostructures, as well as rare earth free synthetic ferrimagnetic heterostructures. Recently, we have observed the same phenomenon in single ferromagnetic films, thus paving the way for an integration of all-optical writing in spintronic devices. Moreover, in similar materials, like [Co/Pt] or [Co/Ni] with high spin polarization and tunable perpendicular magnetic anisotropy (PMA), efficient current-induced domain wall (DW) motion can be observed in magnetic wires, where spin-orbit torque (SOT) or spin transfer torque (STT) provides a powerful means of manipulating domain walls, which is of great interest for several spintronic applications, such as high-density racetrack memory and magnetic domain wall logic. However, the current density required for domain wall motion is still too high to realize low power devices.

It is within this very innovative context that my Ph.D. research has focused on domain wall manipulation in magnetic wires made out of thin film with strong perpendicular magnetic anisotropy combining both spin-polarized current and all-optical switching. Different material structures have been explored, in order to investigate the combined effects of helicity-dependent optical effect and spin-orbit torque or spin transfer torque on domain wall motion in magnetic wires based on these structures. We show that domain wall can remain pinned under one laser circular helicity while depinned by the opposite circular helicity, and the threshold current density can be greatly reduced by using femtosecond laser pulses. Our findings provide novel insights towards the development of low power spintronic-photonic devices.

Université Paris-Saclay
Espace Technologique / Immeuble Discovery
Route de l'Orme aux Merisiers RD 128 / 91190 Saint-Aubin, France